Computational modeling of the mechanics of elastic structural lattices: effects of lattice architecture and hierarchy

Thesis by

Alex J. Zelhofer

In Partial Fulfillment of the Requirements
for the Degree of
Doctor of Philosophy

CALIFORNIA INSTITUTE OF TECHNOLOGY
Pasadena, California

2017
(Defended December 5, 2016)

Alex J. Zelhofer
ORCID: 0000-0002-8064-2876

For my parents, Tony and Deb Zelhofer.

ACKNOWLEDGEMENTS

I would like extend my deepest thanks to my advisor, Dr. Dennis M. Kochmann, for his endless patience and support. He has always had an open door policy to discuss the struggles and triumphs of research for which I am extremely grateful. Dennis helped me develop my skills beyond my applied nature into regions of mathematics and theory I never could have imagined at my journey's start.

Secondly, I thank my committee members for their time and expertise. Each person was influential as either a lecturer or collaborator. Dr. Sergio Pellegrino taught a class on Space Structures providing methods fundamental to truss analysis. In my joint work with Dr. Julia Greer she introduced me to the field of nanomaterials helping shape my understanding of the field and how my computational work may contribute. Finally, I thank Dr. Guruswami Ravichandran as his lectures on Solid Mechanics were thought provoking and insightful.

To my friends[1] in my MCE year I owe great gratitude. My first year at Caltech was a mental and physical challenge and with their support the journey was much more manageable. We waded through theory in the pursuit of fundamental laws with many fruitful discussions late into the night. I am thankful to find such welcoming people willing to teach and help each other. To my lab mates I cannot thank you enough. Specifically Ishan Tembhekar, Jeff Amelang, and Neel Nadkarni you have each helped me develop my research skills in theory and numerics. To those who were collaborators and helpfu critics of my work, namely Lucas Meza, Carlos Portela, and Greg Philpot, I am thankful for our discussions of experimental and numerical methods applied to lattice materials. In the background supporting role is the effort of the MCE and Galcit staff. Specifically Cheryl Greer and Denise Ruiz have extended their knowledge and warmth while navigating workplace hurdles. Lastly, I am indebted to my parents for their continued devotion to my education. Whatever my interest was they let me pursue it with their full support.

Finally, I would like to gratefully acknowledge the support from the National Science Foundation (NSF) through CAREER awards CMMI-1254424 and CMMI-1234364 for helping further the pursuit of science.

---

[1] Matt Burkhardt, Tess Saxton-Fox, Andres Goza, Natalie Higgens, Anthony Massari, Reid Kawamoto, Paul Plucinsky, Francesco Restuccia, and Dingyi Sun

ABSTRACT

This thesis establishes advanced theoretical-computational techniques to understand and predict the mechanical properties of structural lattice metamaterials with a focus on the effective elastic properties. First, attention is devoted to the effective stiffness of hierarchical nanolattices, which depends on lattice topology, architecture, and inherent geometric imperfections. A computational substructuring technique is applied to predict the mechanics of hierarchical truss networks containing thousands to millions of truss members, with each solid, hollow-tube, or composite truss member requiring full-detail 3D resolution. By applying this methodology to hierarchical nanolattices structural hierarchy is shown to span several decades of relative density and effective stiffness with near-ideal effective stiffness scaling. Comparisons between experimental data and model predictions show convincing agreement and highlight the lattice sensitivity to fabrication-induced geometric imperfection. Second, elastic stress wave propagation in structural lattices is investigated with a focus on wave beaming (i.e., directional energy flow) under harmonic mechanical excitation. A new technique is introduced to obtain pseudo-continuous maps of group velocity magnitude vs. propagation direction vs. frequency to predict directional wave propagation, demonstrating traditional beaming prediction techniques are insufficient for many scenarios. The method is applied to two-dimensional structural lattices to predict directional energy flow. Predictions are verified by comparison to explicit dynamic simulations showing the limitations of the classical dispersion relation method. Overall, improved computational techniques are presented to better described, understand, predict and optimize the elastic behavior of truss lattices.

PUBLISHED CONTENT AND CONTRIBUTIONS

Meza, Lucas R. et al. (2015). “Resilient 3D hierarchical architected metamaterials.” In: *Proceedings of the National Academy of Sciences of the United States of America* 112.37, pp. 11502–7. ISSN: 1091-6490. DOI: `10.1073/pnas.1509120112`. URL: `http://www.pnas.org/content/112/37/11502.abstract`.
Contributions: A. J. Z. performed the finite element analysis and contributed to the manuscript.

Zelhofer, Alex J. and Dennis M. Kochmann (2017). “On acoustic wave beaming in two-dimensional structural lattices”. In: *International Journal of Solids and Structures* 115, pp. 248–269.
Contributions: A. J. Z. performed the finite element analysis and co-wrote the manuscript.

TABLE OF CONTENTS

LIST OF ILLUSTRATIONS

LIST OF TABLES

NOMENCLATURE

$\bar{\boldsymbol{k}}$	normalized wave vector independent of scale
$\bar{f}$	normalized frequency independent of material and scale
β	in-plane ratio
$\boldsymbol{b}$	body force density
$\boldsymbol{C}$	damping matrix
$\boldsymbol{e}$	lattice vector
$\boldsymbol{e}^*$	reciprocal lattice vector
$\boldsymbol{f}$	force vector
$\boldsymbol{K}$	stiffness matrix
$\boldsymbol{k}$	wave vector
$\boldsymbol{M}$	mass matrix
$\boldsymbol{p}$	mass-weighted directional contributions
$\boldsymbol{t}$	fraction on a body
$\boldsymbol{u}$	displacement vector field
$\boldsymbol{\epsilon}$	infinitesimal strain tensor
$\boldsymbol{\sigma}$	Cauchy stress tensor
$\ddot{\boldsymbol{u}}$	acceleration vector field
Δt	timestep
$\dot{\boldsymbol{u}}$	velocity vector field
$\mathbb{C}$	linear elastic stiffness tensor
γ	stretch ratio
ω	frequency (rad/s)
Φ	mass orthonormalized eigenvector
ρ	mass density
$\tilde{\boldsymbol{f}}$	condensed force vector

$\tilde{\boldsymbol{K}}$	condensed stiffness matrix
c	bar wave speed
E	Young's modulus
f	frequency (Hz)
N	shape function
t	time
v_g	group velocity
v_p	phase velocity
FBZ	first Brillouin zone
IBZ	irreducible Brillouin zone
RUC	representative unit cell

Chapter 1

INTRODUCTION

1.1 Motivation

From the clothes we wear to the food we eat, every product has been touched by engineering. In making these product one must consider the material it will be built from. Every year society demands more from its products and in turn from the material itself. An excellent example is that of a cell phone screen protected by a transparent, engineered material. The specific example of Corning® Gorilla® Glass promising to give "consumers the drop protection they need if they fumble their phones while snapping photos, texting on the go, watching videos, or performing other everyday activities at or below shoulder level" (Corning, 2016). The dropping and subsequent breaking of the protective glass is of concern to nearly all of today's society from young teenagers to the elderly. Simultaneously society expects the display protection material to offer excellent sensitivity for touch interaction, near flawless optical clarity, ever improving toughness, and all at a reasonable price. This impressive feat is not accomplished by a single material exhumed from the ground, but instead by a meticulously engineered composite material. Taking a step back into the broader picture, cell phone screen protection is but a tiny case of vast industries such as automotive, construction, and aerospace where consumers demand improved performance. Admittedly such improved characteristics can come from design of a part or assembly, but here the focus is on the fundamental building blocks of these products, i.e. materials.

Materials can be characterized in many ways with primary properties for technological applications including density, stiffness, strength, fracture toughness, loss coefficient, electrical conductivity, thermal conductivity, and optical properties. In his book (Ashby, 2005) introduced a visual interpretation of material properties, which as since become known as "Ashby Charts", viz. the mapping of one material property vs. another. The four specific properties this work will focus on are stiffness, strength, loss coefficient, and mass density. An example Ashby plot is shown in Fig. 1.1.

Engineering materials can be generally sorted into six categories; metals, ceramic, polymer, glass, elastomers, and hybrids (Ashby, 2005) as illustrated in Fig. 1.2.

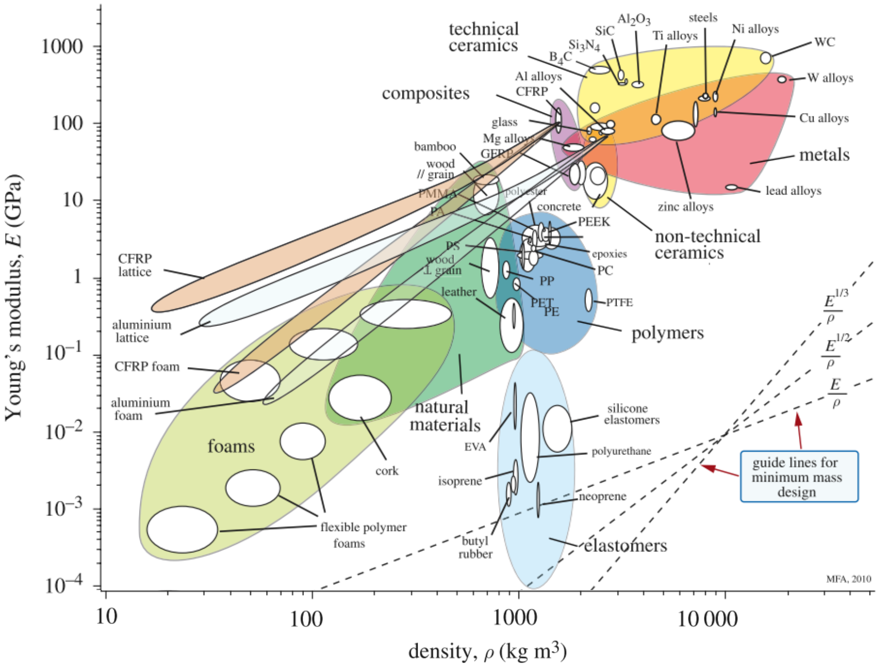

Figure 1.1: Natural and man-made material Young's modulus versus mass density distribution taken from (Fleck, Deshpande, and Ashby, 2010) with permission from copyright holder, The Royal Society.

Within each of the outer family systems (i.e. excluding hybrids) nearly all materials are made of several types of fundamental elements on the molecular level. An example of molecular composite materials are metal alloys such as steel. One achieves significantly varying material properties within the steel material system by combining iron atoms with other molecules such as manganese, nickle, chromium, and titanium. Further processing, such as heat treatment, can enhance the material properties by changing the microstructure. To further improve on material properties, one turns to hybrid materials, illustrated by the inner circle of Fig. 1.2. Hybrids are a composite of the bulk material families where geometric shapes and configurations are created on the tens of nanometers and larger length-scale. To better characterize these materials one refers to the volume fraction of a particular component defined as

$$f_i = \frac{V_i}{\sum_j V_j}\,, \tag{1.1}$$

where V_i and is the total volume of material i in a given sample. A common use of this is in describing carbon-fiber composite materials containing matrix and fiber volume fractions. This concept of volume fraction can then allow us to calculate the expected properties of our hybrid material. Knowing the volume fraction of each

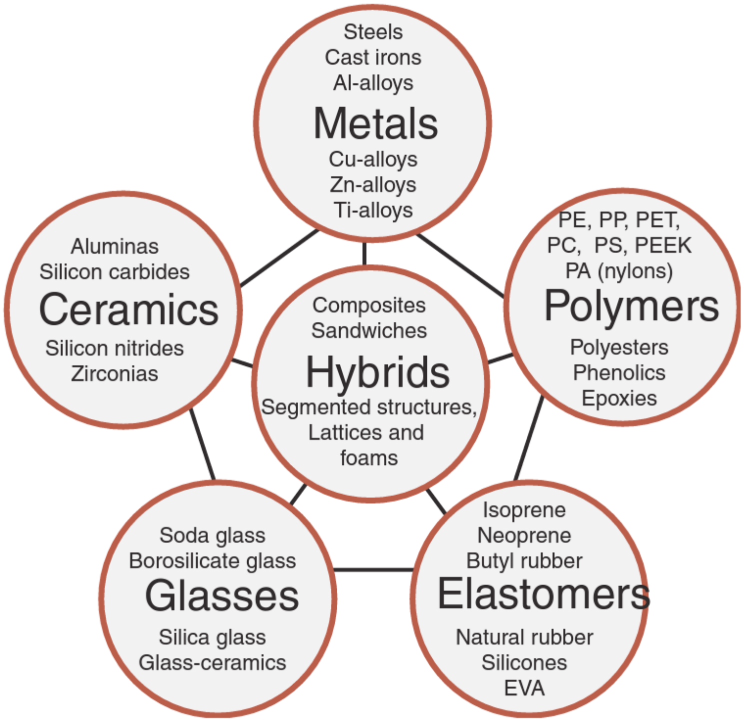

Figure 1.2: Illustrating the breadth of bulk materials combined to create hybrid materials, including lattices. Taken from (Ashby, 2005).

constituent allows us to predict the density of our new material using

$$\rho_h = \sum_i f_i \rho_i \,, \tag{1.2}$$

where ρ_i is the density of the ith constituent material. One can also, with less accuracy than the density calculation due to assumptions, predict the modulus using the famed Voigt and Reuss bounds for a two-phase composite material. The Voigt upper bound on the modulus (which results from assuming that the two components are under the same strain and the stress is the volume average of local stresses) the effective modulus is described as

$$E_v = f_1 E_1 + f_2 E_2 \,. \tag{1.3}$$

As a lower bound one can assume the two constituent materials have the same stress and the strain is the volume average of the local strains, so that the effective modulus is described as

$$E_r = \frac{E_1 E_2}{f_1 E_2 + f_2 E_1} \,. \tag{1.4}$$

For illustration purposes the upper and lower bounds of a fictional composite material system are presented in Fig. 1.3. This implies that the effective stiffness of any solid

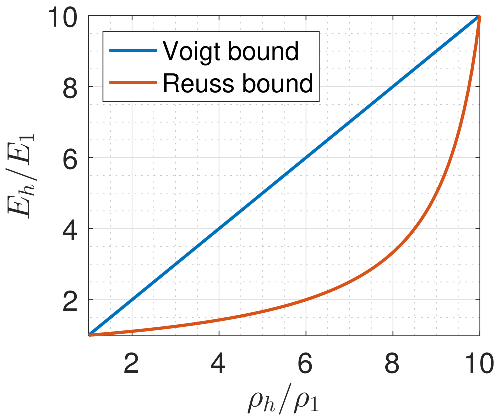

Figure 1.3: Illustration of the Voigt and Reuss bounds of a composite material system with $E_2/E_1 = 10$, $\rho_2/\rho_1 = 10$ with the volume fractions varying from $f_1 = 1$, $f_2 = 0$ continuously.

composite is bounded from above and below by the Voigt and Reuss estiamtes, and that the mass density is given exactly by the volume average of the constituent densities. If one revisits Fig. 1.1 one can see this idea of average properties played out in the upper corner dominated by metal alloys. However, if one was interested in the extremely-low-density materials, the second phase is oftentimes no longer solid and instead is a fluid. These materials are referred to as cellular solids.

Characterized by their extremely efficient distribution of mass, engineered cellular solids achieve properties such as strength and stiffness at incredibly low effective densities. A simple example of beams and panels increasing stiffness while minimizing material is illustrated in Fig. 1.4.

Examples of cellular solids taking advantage of geometric arrangement with minimal mass include foams, honeycombs, and lattices. An excellent overview of these materials can be found in (Gibson and Ashby, 1988; Deshpande, Ashby, et al., 2001). Each of these materials can be made from different constituent materials such as polymers and metals, nevertheless, the general classification is determined by the use of stochastic or non-stochastic geometric configurations. Foams are geometrically stochastic but statistically similar in qualties such as pore size, shape, and distribution. In contrast, honeycombs and lattices are defined by a single repeating representative unit cell with specifically engineered geometry. As shown in Fig. 1.1 lattices are able to achieve higher stiffness for a given density than foams and therefore are more structurally mass-efficient. With more mass efficient materials one is helping fulfill the societal need of enhanced materials in a material

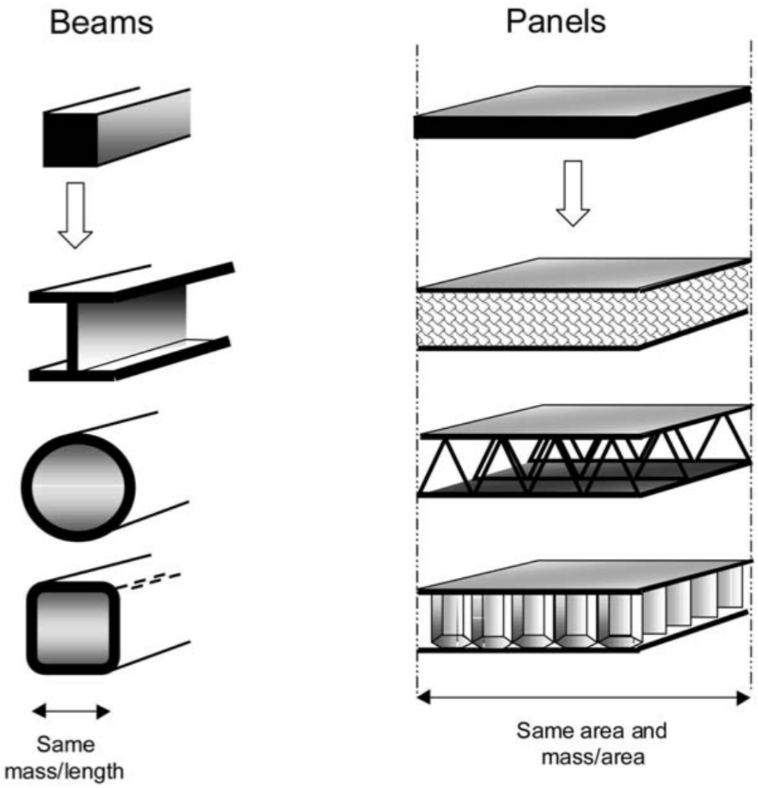

Figure 1.4: Demonstration of mass distribution used to leverage increased stiffness and strength. From top to bottom example beam geometries are solid rectangular, I-beam, round tube, and square tube. Panel examples, from top to bottom, show a solid panel, waffled core, truss core, and honeycomb core. For the same mass flexural stiffness can be as much as 50 times that of the solid beam or panel (Ashby and Bréchet, 2003). Reprinted from (Ashby and Bréchet, 2003) with permission from copyright holder, Elsevier.

space very few other material system can venture and is therefore worthy of further investigation.

1.2 Lattices

Lattice materials, aside from unprecedented stiffness, feature incredible strength, fracture toughness, energy absorption, and even energy directivity at exceptionally low densities. Commonly, these properties are evaluated in terms of the *relative density* defined as

$$\tilde{\rho} = \frac{m_{\mathrm{RUC}}}{V_{\mathrm{RUC}}} , \tag{1.5}$$

where m_{RUC} and V_{RUC} are the mass contained in and volume of the RUC, respectively. Relative density allows one to more clearly isolate the effect of unit cell architecture rather than evaluating the effective density of the lattice influenced by its constituent materials.

Some of the influential theoretical (Deshpande, Fleck, and Ashby, 2001) and experimental (Wadley, 2006) work on lattice materials was with open-cell trusses and closed-cell honeycombs as panel cores providing high bending stiffness at low densities. In a review of micro-architectured materials, Fleck, Deshpande, and Ashby (2010) explored concepts of nodal connectivity and structural hierarchy and their effects on effective material properties such as stiffness and strength. In the pursuit of multi-functional cellular structures, Valdevit et al. (2011) outlined past and present manufacturing approaches and identified experimental and computational tools required to further the field. In more recent work, Schaedler and Carter (2016) detailed the latest fabrication methods for architected materials including metal, polymer, and ceramic with possible coating techniques. In particular, this thesis extends work on ultra-lightweight solid (Deshpande, Fleck, and Ashby, 2001) and hollow (Valdevit, 2014; Jang et al., 2013; Schaedler, Jacobsen, et al., 2011; Meza, Das, et al., 2014; Meza and Greer, 2014) structural lattices.

As interest in lattice materials developed, so did manufacturing techniques at increasingly smaller length-scales. The following examples are meant as state-of-the-art manufacturing methods for the smallest length scale and by no means are exhaustive. The reader is referred to (Valdevit et al., 2011) for a more extensive listing. Wadley et al. (2003) manufactured sandwich cores consisting of lattices with millimeter-scale feature sizes, shown in Fig. 1.5, by bending perforated sheets of metal. The process was able to create multiple layers of truss structure but at the cost of geometric freedom and a relatively work-intensive process. Moving down in length-scale to microlattices, Schaedler, Jacobsen, et al. (2011) used collimated ultra-violet light, a light mask, and a photo monomer to create polymer and metal microlattices as shown in Fig. 1.6. Unfortunately, the obtainable geometric space was limited due to the manufacturing technique's requirement of straight wave guides creating straight member lattices. Venturing to the nano-scale, The Nanoscribe machine in the lab of Julia R. Greer at Caltech is able to print nearly any geometry nano-scale lattices via two-photon lithography, see Fig. 1.7, with nanometer-scale precision.

Although the manufacturing methods have allowed lattices to be manufactured at smaller scales allowing the lattice to act as an effective material instead of a structure, the fundamental question remains of which architecture is the best, e.g., in terms of the effective (meta) material stiffness. In the following section past and present perspectives on maximizing effective stiffness are presented.

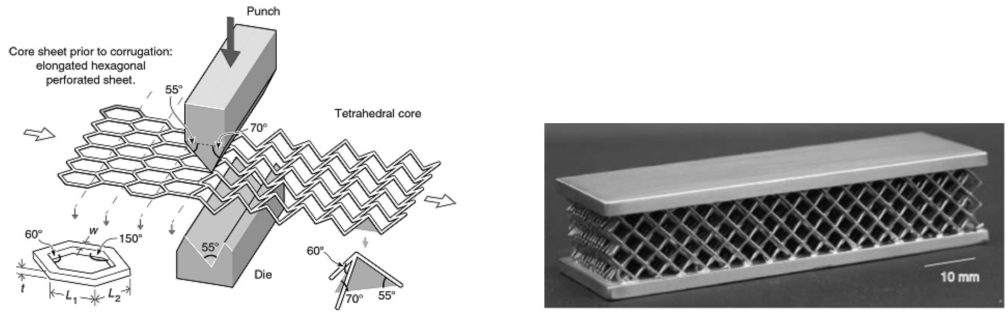

(a) Manufacturing a single layer of lattice-core material by bending perforated sheet metal.

(b) Sandwich panel made of 304 stainless steel with relative density of 12.6%.

Figure 1.5: Millimeter scale lattice-core sandwich material made from individually assembled layers. Reprinted from (Wadley et al., 2003) with permission from copyright holder, Elsevier.

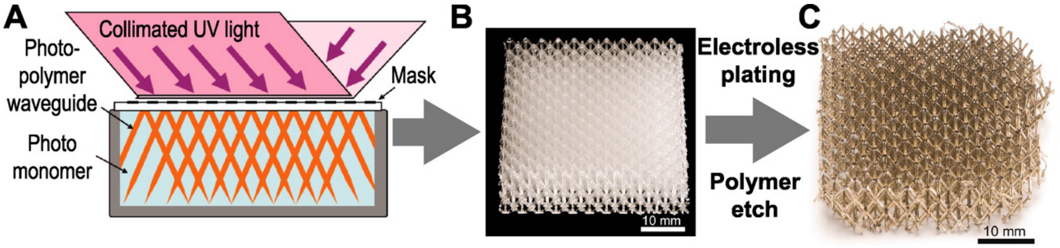

Figure 1.6: Manufacturing of a metal microlattice. (A) Collimated light is sent through a mask into self-propagating waveguide photometer. (B) The developed polymer lattice. (C) Resultant Ni-P hollow-member lattice after plating and polymer etching. Reprinted from (Schaedler, Jacobsen, et al., 2011) with permission from the copyright holder, The American Association for the Advancement of Science.

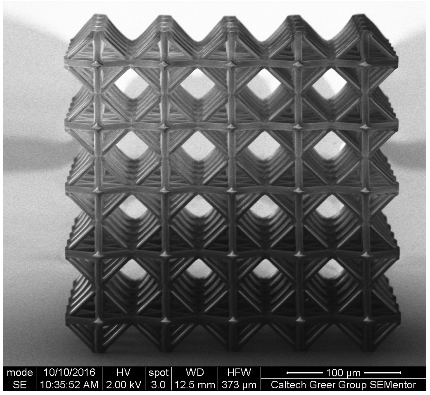

Figure 1.7: Nanolattice with octahedron unit cells made of polymer and created via two-photon lithography. Image courtesy of Carlos Portela (Caltech).

1.2.1 Effective stiffness

One possible prospect of lattice materials is to produce controllable mechanical performance in a mass-efficient manner. However, the natural question, is what lattice architecture is the most efficient. Throughout literature the scaling of the relative modulus with relative density is used as a measure of lattice geometry efficiency, where the relationship is described as

$$E_h = c_1 E_s \tilde{\rho}^{c_2} \,, \tag{1.6}$$

where E_h is the effective modulus of the lattice material, c_1 is a fitted, geometry dependent constant, E_s is the modulus of the constitutive material, and c_2 is a fitting scaling parameter which is also geometry dependent. Ideally c_2 is as close to one as possible indicating a stretching-dominated lattice. Illustrated by Fig. 1.8, stretching-dominated were shown to scale better than bending-dominated lattices such that the relative modulus of the design scaled linearly with the relative density, allowing one to reach higher stiffness at lower relative density. Until recently, it was believed that all lattice materials could be categorized into stretching-dominated and bending-dominated lattices, as outlined in (Deshpande, Ashby, et al., 2001), based

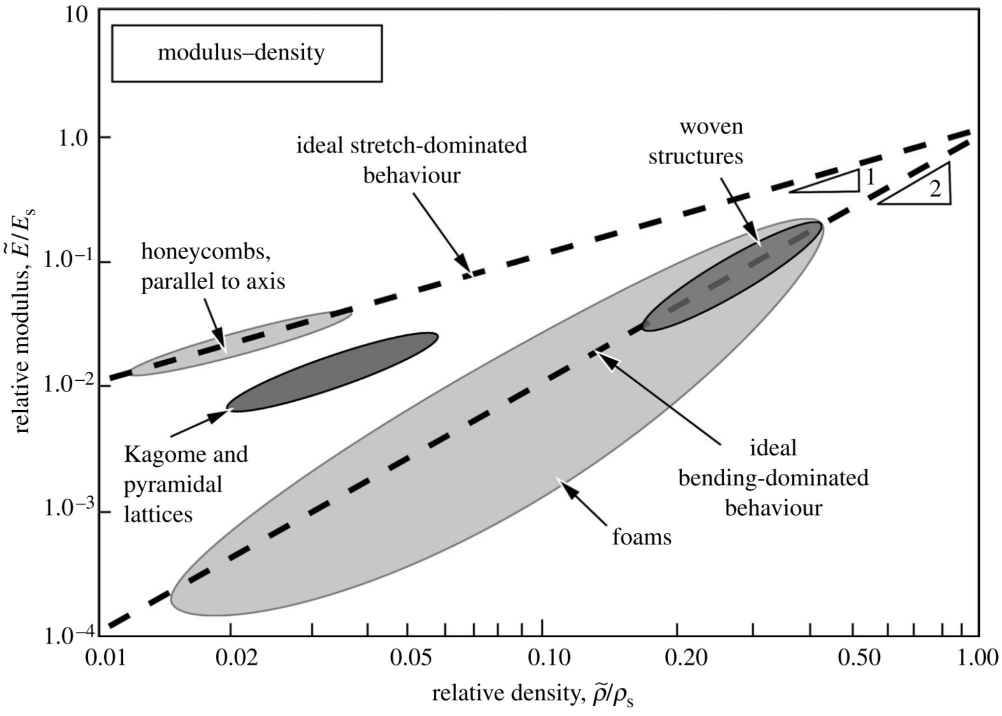

Figure 1.8: Ashby plot of relative modulus to relative density of foams, lattices, and honeycombs taken from (Ashby, 2006) with permission from copyright holder, The Royal Society.

on nodal connectivity. However, in recent work by Meza, Phlipot, et al. (2016) it was shown that the stiffness-density scaling of nanolattices cannot be predicted simply based on nodal connectivity. The classical theory only applied to slender structures, whereas manufacturable nanolattices do not fall into that category. It was shown that stretching-dominated and bending-dominated predictions, based on nodal connectivity alone, apply only to lattices whose beam members have a slenderness of approximately 10 or greater, where slenderness is defined as

$$\lambda = \frac{L}{D}, \tag{1.7}$$

where L is the length of the member measured node to node and D is the effective diameter of the lattice member (Meza, Phlipot, et al., 2016). As an example, Fig. 1.9 presents experiments and simulations of a hollow octet lattice and demonstrates how hollow lattice member geometric factors, such as slenderness and wall thickness-to-length ratios, effect stiffness scaling. In this figure, full-resolution finite element simulations are used to determine the effective stiffness of a non-slender octet lattice. Note how the octet lattice is generally considered a stretching-dominated lattice and therefore has a scaling $c_2 = 1$ as drawn in a yellow band in Fig. 1.9. However, depending on the slenderness of the lattice, the calculated effective stiffness does not necessarily exhibit the typical scaling law given by (1.6) with unique scaling parameters.

For completeness the characterization based on nodes and lattice member connectivity appropriate for lattices with members $\lambda > 10$ is briefly summarized. As suggested by Deshpande, Ashby, et al. (2001), one can identify stretching-dominated lattices by examining Maxwell's rule,

$$b - 3j + 6 = s - m, \tag{1.8}$$

where b is the number of struts, j the number of idealized frictionless nodes, s the number of states of self-stress, and m the number of mechanisms. To achieve stretching-dominated lattices, where effective stiffness scales linearly with relative density, one seeks designs where $b - 3j + 6 \geq 0$ as a necessary condition. In this case the structure can contain a mixture of states of self-stresses and mechanisms. For an exact count of s and m, i.e. if the lattice is stretching-dominated, one can employ e.g. the matrix analysis method developed by Pellegrino and Calladine (1986). As illustrations, example unit cells are shown in Fig. 1.10 indicating whether or not the geometry, as predicted by Maxwell's rule, is stretching-dominated.

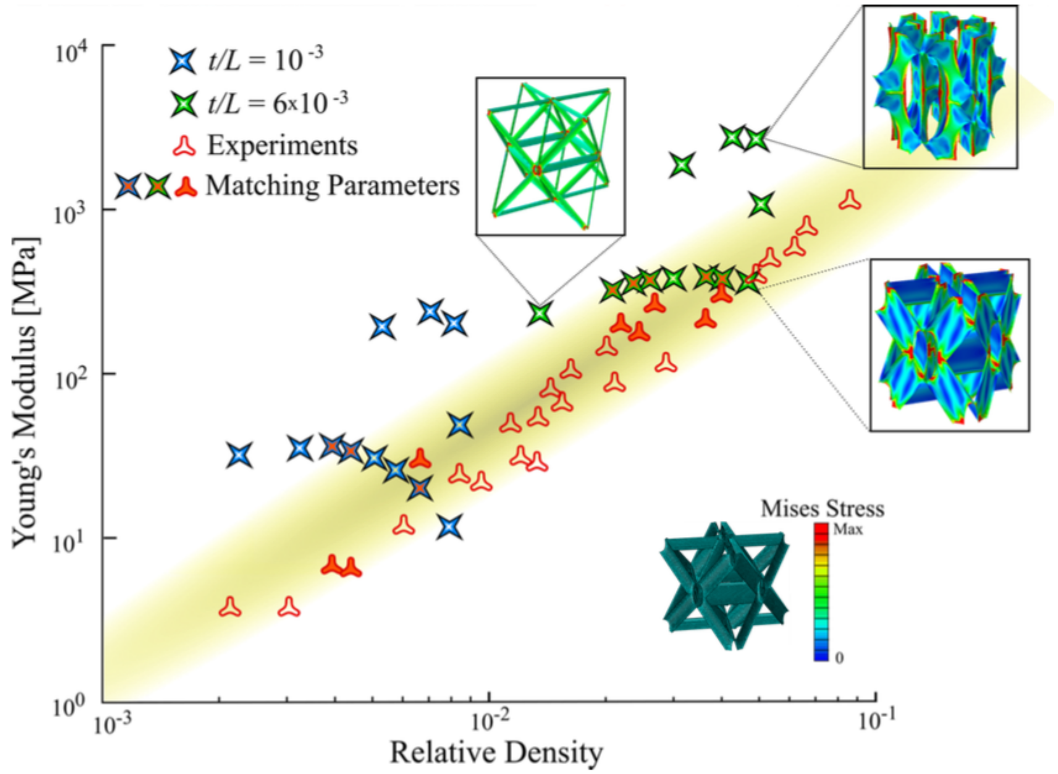

Figure 1.9: The effect of the thickness-to-length and diameter-to-length ratios on the effective Young's modulus of an hallow octet unit cell with periodic boundary conditions. Comparison is made to experiments (hollow red symbols) from (Meza, Zelhofer, et al., 2015). The yellow band shows a linear scaling with relative density. Numerical simulations (green and blue) show effective stiffness (i.e. scaling) is highly sensitive to geometric ratios. Image courtesy of Carlos Portela (Caltech).

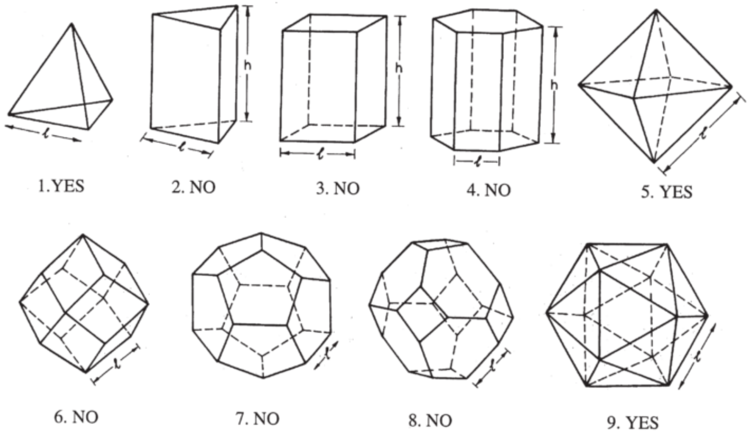

Figure 1.10: Three dimensional polyhedra labeled indicating if the unit cell by itself is predicted to be stretching-dominated. Figure taken from (Deshpande, Ashby, et al., 2001) with permission from copyright holder, Elsevier.

In pursuit of the best-scaling unit cell design many lattice architectures have been examined. One of the most commonly used designs is that of the octet unit cell by Deshpande, Fleck, and Ashby (2001). Hutchinson and Fleck (2006) explored two-dimensional trusses with use of the matrix method developed by Pellegrino and Calladine (1986). In recent years, Professors Julia R. Greer of Caltech and Nicholas X. Fang of MIT have created and tested lattice designs on the nanoscale (Zheng et al., 2014; Meza, Das, et al., 2014; Montemayor et al., 2014). Given the nanoscale precision of these manufacturing methods it was possible to explore geometries with multiple length scales configured as hierarchical lattice structures. This opens entirely new opportunities for the design of massively complex lattice architecture, which - in turn - requires advanced theoretical and computational techniques to predict their properties. Chapter 3 details the use of the finite element method to calculate the effective stiffness of these hierarchical lattices with comparisons to experimental realizations.

1.2.2 Wave propagation

Aside from the effective static properties of a lattice material one can also consider its dynamic or inelastic properties. As mentioned previously, all materials exhibit some level/amount of damping measured e.g. as the loss coefficient. The greater the loss coefficient, the greater the amount of damping provided by the material. From work performed by (Ashby, 2005) one can conclude that materials with high loss coefficients include generally low-modulus elastomers and polymer foams with low melting points. Materials with higher modulus and much higher melting points usually have significantly lower loss coefficients by orders of magnitude. To design a material with relatively high modulus, high melting temperature, and effective loss coefficient one can turn to lattice materials. An unexpected, but unique and interesting consequence of the ordered lattice architecture is the phenomenon of frequency-dependent wave propagation. Where normal materials inherently dampen excitation due to microstructural mechanisms or molecular structure, lattice materials can do so using geometry alone, even in linear elastic lattices without internal material damping.

In general, engineered solids designed for optimal wave propgation are oftentimes referred to as phononic metamaterials. In a review on wave propagation in metamaterials, Hussein et al. (2014) outlined the origins, current work, and future directions of the field generally containing phonic crystals, composites, and lattices metamaterials. Among the various dynamic phenomena encountered in phononic metamaterials, researchers have been interested in *directional wave propagation* commonly determined using dispersion relations.

A simple and canonical example of frequency-dependent wave propagation, depicted in Fig. 1.11, is outlined below. Consider a diatomic chain of masses and springs of equal stiffness in a perfectly elastic system. In the following, a short derivation of the dispersion relation is presented. First, we considered the force balance on the nth pair of mass particles m_1 and m_2 given as

$$m_1\ddot{u}_{n,1} = k_s(u_{n,2} - u_{n,1}) - k_s(u_{n,1} - u_{n-1,2}) \tag{1.9}$$

and

$$m_2\ddot{u}_{n,2} = k_s(u_{n+1,1} - u_{n,2}) - k_s(u_{n,2} - u_{n,1})\,, \tag{1.10}$$

where $u_{n,i}$ is the displacement of the ith (first or second) mass in the nth pair of particles, and k_s is the stiffness of the spring between the particles. If we assume the displacements of the masses have the form of a traveling wave, viz.

$$u_{n,1} = A_1e^{i(kna-\omega t)} \tag{1.11}$$

$$u_{n,2} = A_2e^{i(kna-\omega t)} \tag{1.12}$$

where a is the spacing between each pair of particles, k is the wave vector, ω the frequency of excitation, and t is time, we can rewrite Eqns. (1.9) and (1.10) as

$$A_1(\omega^2m_1 - 2k_s) + A_2k_s(1 + e^{-ika}) = 0 \tag{1.13}$$

$$A_1k_s(1 + e^{ika}) + A_2(\omega^2m_2 - 2k_s) = 0\ . \tag{1.14}$$

For a non-trivial solution (i.e. constants $A_1, A_2 \neq 0$), we must have,

$$\det\begin{pmatrix}\omega^2m_1 - 2k_s & k_s(1 + e^{-ika}) \\ k_s(1 + e^{ika}) & (\omega^2m_2 - 2k_s)\end{pmatrix} = 0\ . \tag{1.15}$$

Solving Eq. (1.15) for ω, we arrive at the dispersion relation mathematically described as

$$\omega^2 = \frac{k_s}{m_1m_2}\left(m_1 + m_2 \pm \sqrt{m_1^2 + m_2^2 + 2m_1m_2\cos ka}\right) \tag{1.16}$$

and illustrated in Fig. 1.11. If the two masses are not equal, a frequency band referred to as a band gap is predicted by the dispersion relation analysis given mathematically are given by the two solutions in (1.16). In terms of the mass-spring system dynamics, a band gap means that, if the system is excited at any frequency within the band gap, the motion will be effectively damped out by local resonance (i.e. the wave motion cannot propagate infinitely). In the cases, of the masses being equal, Eqn. (1.16) simplifies to

$$\omega^2 = \frac{k_s}{2m}\left(2m \pm \sqrt{2m^2(1+\cos ka)}\right) , \tag{1.17}$$

which implies that no band gap exists, as one can clearly see in Fig. 1.11 .

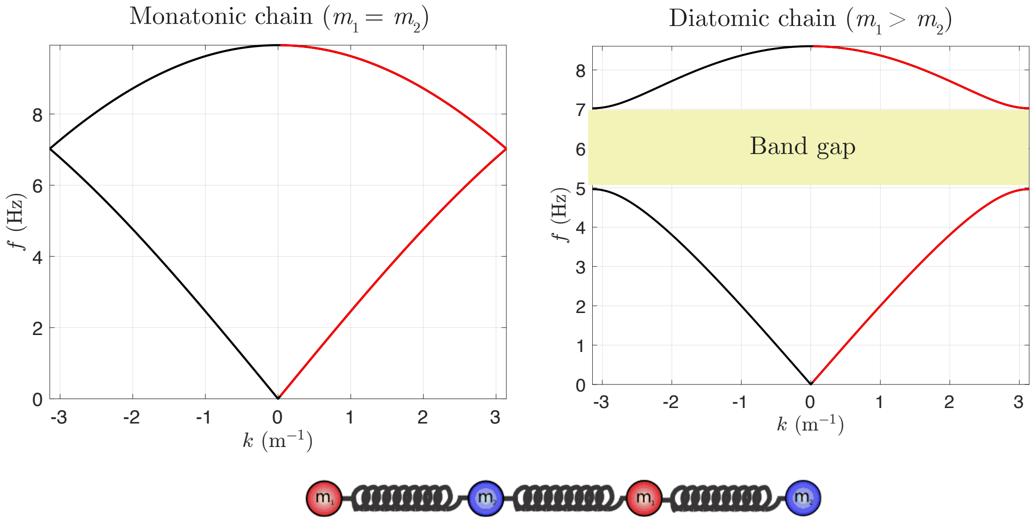

Figure 1.11: Canonical dispersion relation example of a monatomic and diatomic mass-spring chain consisting of springs with stiffness $k_s = 10$ N/m. When the two masses, $m_1 = m_2 = 1$ kg, are equal (left image), a continuous frequency band exists propagating waves. When the two masses are unequal, $m_1 = 2$ kg and $m_2 = 1$ kg, (right image), a band gap exists such that the frequencies within the band gap will not propagate through the system. To illustrate the symmetry of the dispersion relation the negative and positive wavelengths are colored in black and red, respectively.

In considering a system of increasing geometric complexity, one turns to approximate methods such as the finite element method. With significant flexibility and ease one can calculate the dispersion relation e.g. two-dimensional lattices made of Euler-Bernoulli beams such as the hexagonal lattice shown in Fig. 1.12 studied by Phani et al. (2006). Between the normalized frequencies of $\omega = 4$ and $\omega = 6$, there exists a band gap. As discussed in Phani et al. (2006) the width of the band gap is influenced by the slenderness λ of the lattices members. In careful examination of Fig. 1.12 only considers the *edge* of the unique wave-vector space, IBZ, , as being sufficient to extract information about the existence of band gaps. As Chapter 4 illustrates, using the IBZ to determine if an omnidirectional band gap exists fulfills a necessary condition but is not sufficient to prove that band gap does not exist. This idea was already expressed in work by Spadoni et al. (2009) where chiral lattices were investigated. As an illustration of the work done by Spadoni et al. (2009) the edge and corresponding full dispersion surfaces are shown in Fig. 1.13. Clearly a full band gap exists given the full dispersion relation which one cannot deduce from the edge.

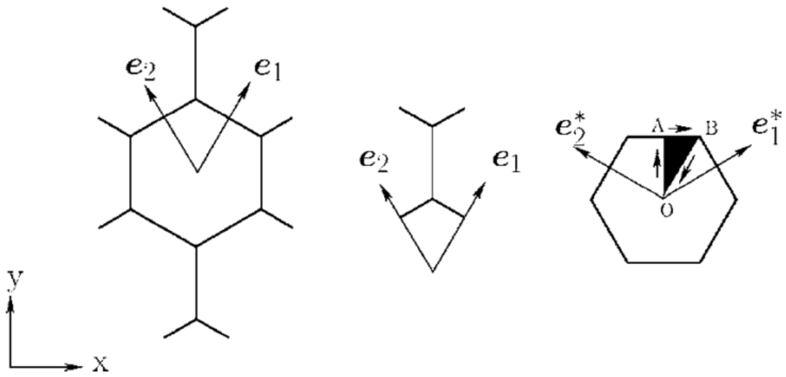

(a) Hexagonal unit cell with lattice vectors $\boldsymbol{e}_1$, $\boldsymbol{e}_2$ and reciprocal lattice vectors $\boldsymbol{e}_1^*$, $\boldsymbol{e}_2^*$.

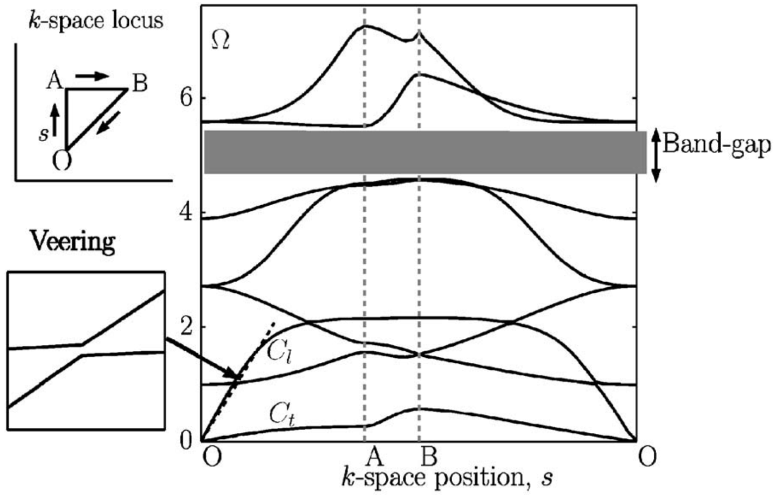

(b) Dispersion relation along parameterized irreducible Brillouin zone edge path O-A-B-O

Figure 1.12: Parameterized dispersion relation along the irreducible Brillouin zone edge in k-space for a regular two-dimensional hexagonal lattice made of beams of slenderness $\lambda = 50$. Figure is taken from (Phani et al., 2006) with permission from the copyright holder, AIP Publishing LLC.

In the pursuit of maximizing the band gaps of two-dimensional lattices made of

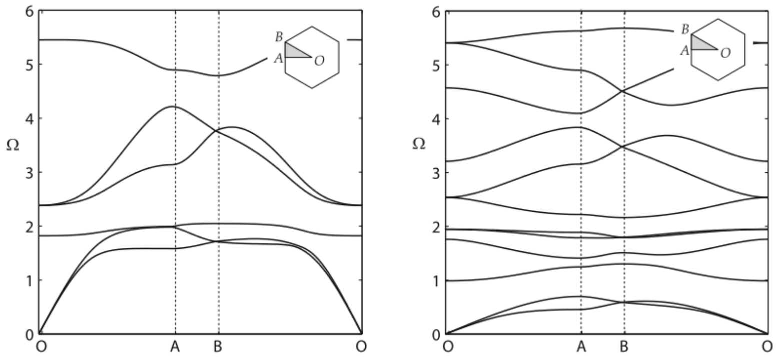

(a) $L/R = 0.90$ (b) $L/R = 0.60$

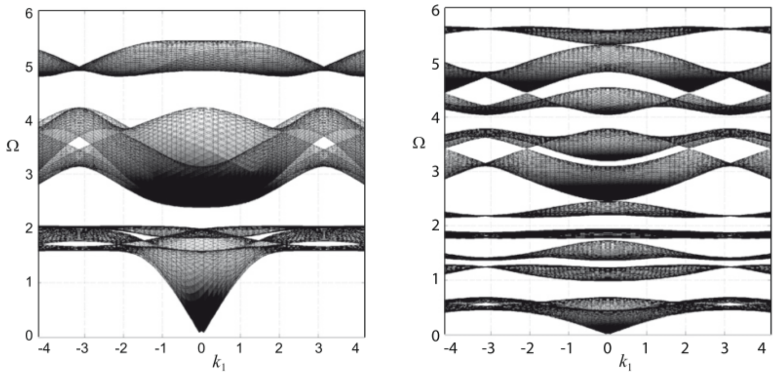

(c) $L/R = 0.90$ (d) $L/R = 0.60$

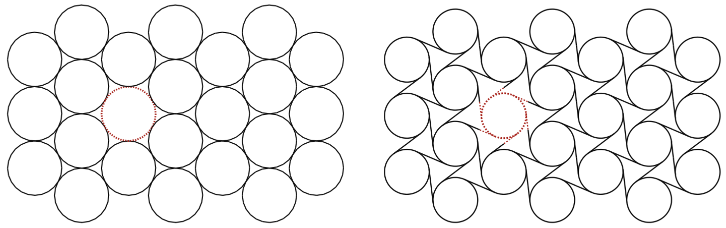

(a) $L/R \to 0$ (b) $L/R = 0.60$

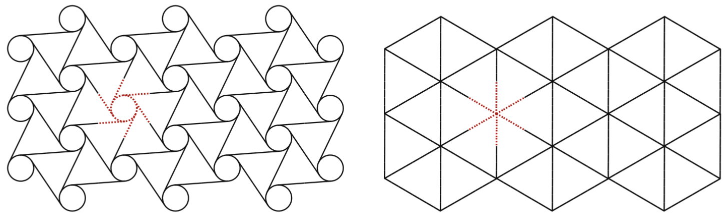

(c) $L/R = 0.90$ (d) $L/R \to 1$

Figure 1.13: Chiral lattices can be characterized by the strut-length-to-circle-radius ratio L/R in the range 0 to 1. Dispersion relations are shown for $L/R = 0.90$ and $L/R = 0.60$ in parameterized form, (a) and (b), along with the full representation, (c) and (d). Images are taken from (Spadoni et al., 2009) with permission from the copyright holder, Elsevier.

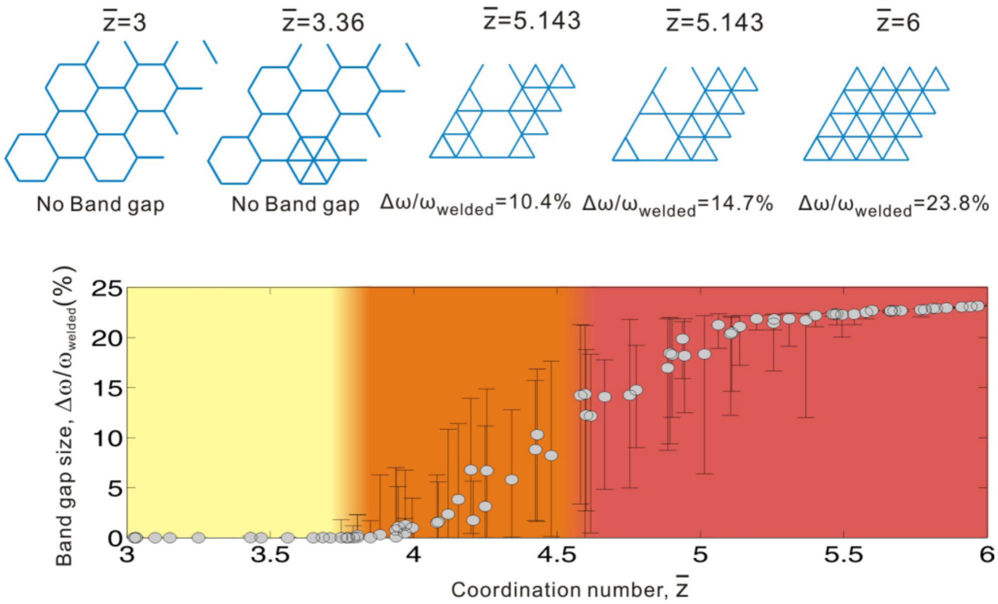

Figure 1.14: P. Wang et al. (2015) investigated the effect of average nodal connectivity, $\bar{z}$, of a two-dimensional lattice on the width of a complete band gap, $\Delta\omega$, relative to the first flexural frequency of a fixed-fixed beam (i.e. ω_{welded}). Taken from (P. Wang et al., 2015) with permission from the publisher, American Physical Society

beams, P. Wang et al. (2015) investigated the influence of average nodal connectivity $\bar{z}$ of a lattice as shown in Fig. 1.14. The average nodal connectivity was varied from $\bar{z} = 3$ to $\bar{z} = 6$ corresponding to hexagonal and triangular lattices, respectively. Wang et al. found a positive correlation between band gap width and average number of members connecting at a node, otherwise known as the coordination number.

Aside from frequency-dependent wave propagation, lattice materials also exhibit *directional wave propagation*. An illustration of this property is given by the example presented in (Casadei and Rimoli, 2013) who varied the volume fraction of solid material of a two-dimensional lattice and excited the center of the lattice to study the spreading of the propagating wave. As one can see illustrated in Fig. 1.16, the lower the volume-fraction of solid material in the lattice, the stronger the potential wave directionality becomes.

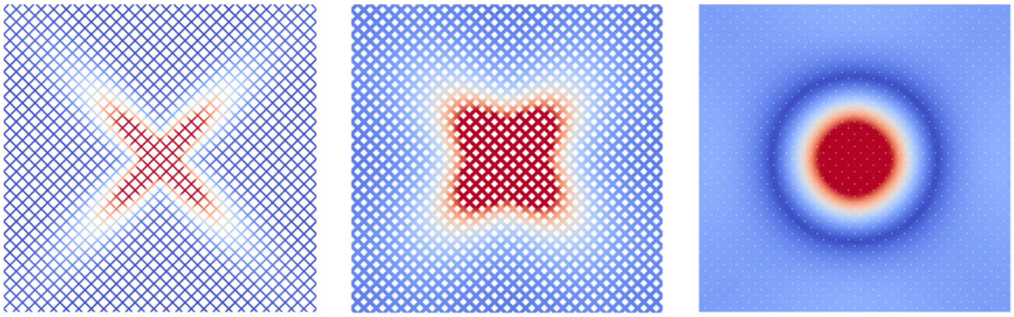

Figure 1.15: From left to right, an array of two dimensional diamond lattices of solid volume fraction 0.33, 0.66, and 0.99. Each lattice is excited at the center with a point forces in the low-frequency spectrum applied in the positive and negative horizontal and vertical directions. Color shows wave amplitude excitation (on a normalized scale) illustrating the influence of volume fraction on directional energy flow. Taken from (Casadei and Rimoli, 2013) with permission from the copyright holder, Elsevier.

In summary, lattices materials are capable of frequency-dependent, directional wave propagation as shown in the wave propagation of a rectangular lattice made from Euler-Bernoulli beams presented in Fig. 1.16. At a lower excitation frequency of 51.6 Hz waves travel in all directions, whereas, when excited at a higher frequency of 76.4 Hz, waves only travel in a 90 degree regions centered at 0 and 180 degrees. So far, studies of directional wave propagation in lattices have been primarily observational, meaning the existence of directional band gaps has been observed and can be predicted by recourse to the dispersion relations (which is only a necessary condition to confirm that no band gaps exist). However, there is not efficient theoretical-computational strategy to sufficiently prove the (non-)existence of directional wave motion in arbitrary lattices. Chapter 4 revisits fundamental two-dimensional lattice shapes and, by improving on existing methodology, provides a strategy to rigorously predict directionality and use this new approach to demonstrate the influence of lattice geometry on directional wave propagation.

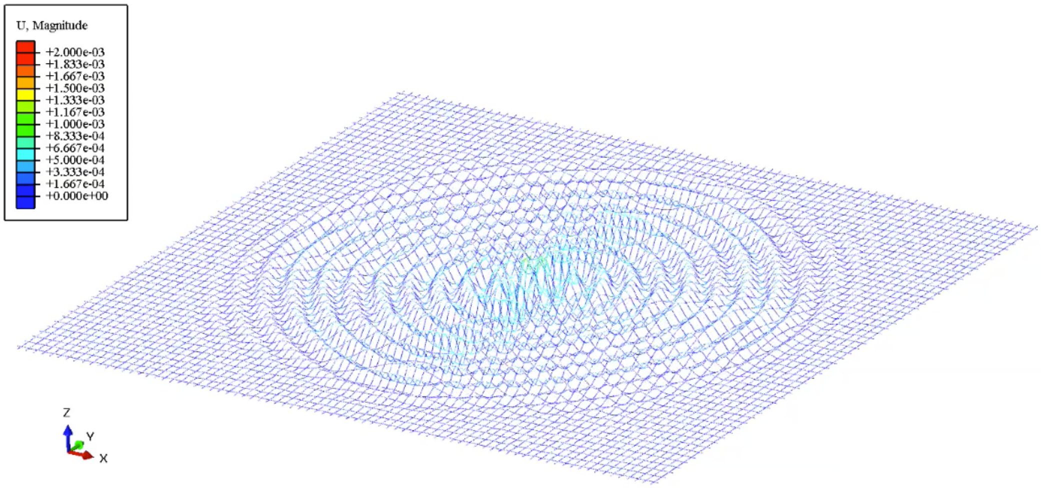

(a) *Omnidirectional* wave propagation due to low-frequency excitation at 51.6 Hz

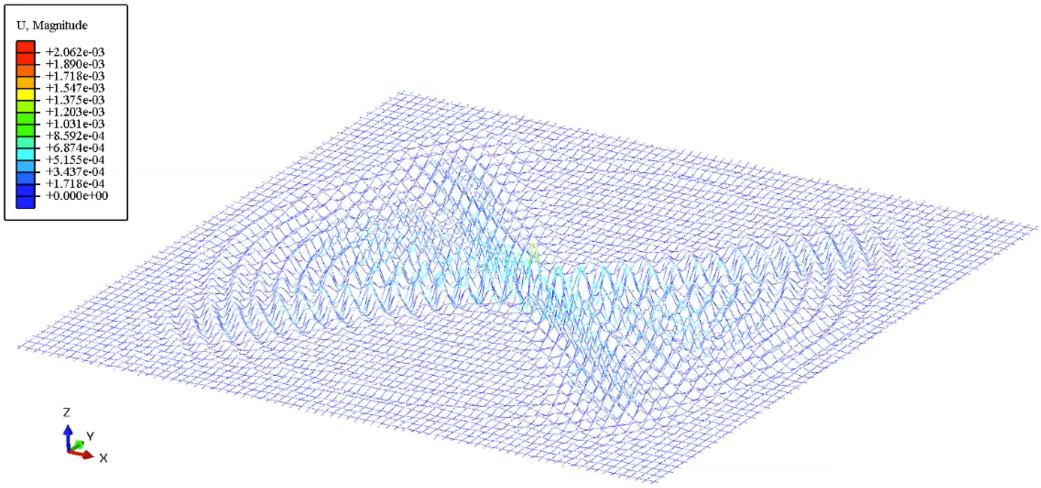

(b) *Directional* wave propgation due to high-frequency excitation at 76.4 Hz

Figure 1.16: Explicit-dynamics finite element simulation of out-of-plane wave propagation in a two-dimensional, rectangular lattice of circular cross-section beams with slenderness $\lambda = 10$, length $L = 1$, and stretch ratio $\gamma = 1.5$ (as defined in Ch. 4) is subjected to single-frequency, mechanical excitation. Color coding shows the magnitude of out-of-plane displacement.

1.3 Thesis outline and contributions

In the following chapters improved computational tools to describe and predict the effective performance of elastic lattices, including stiffness and wave motion. Chapter 2 reviews the fundamentals of the finite element method to lay the foundation for subsequent layers. Chapter 3 focuses on the effective stiffness of three-dimensional hierarchical nano lattices. Two simulation methodologies involving differing levels of geometric accuracy are utilized to minimize computational expenses. Simulations predict that structural hierarchy can achieve the ideal stretching-dominated scaling in nano-lattices while spanning decades of relative density and effective stiffness. Chapter 4 focuses on directional wave energy propagation (i.e. beaming) in two-dimensional lattices. This work improves on existing methods to predict directional wave propagation and provides analysis of fundamental lattice designs. Beaming predictions are then compared to explicit-dynamic simulation results, highlighting directional amplitude and frequency response for validation of the new methodology. Finally, Chapter 5 concludes this thesis and summarized potential future work.

Chapter 2

FINITE ELEMENT DERIVATION

2.1 Introduction

This body of work is restricted to linearized kinematics and as such the derivation of finite elements will be performed accordingly. First, the quasistatic case is derived from the governing equations and the first variation of the total potential energy. Second, the dynamic case is considered and derived using the action principle. Note, this formulation is adopted from (Kochmann, 2014)

2.2 Quasistatics

The governing equations of solid mechanics for linearized kinematics within the quasistatic framework are

$$\sigma_{ij,j} + \rho b_i = 0 \qquad \text{in } \Omega\,, \tag{2.1}$$

$$u_i = u_i^* \qquad \text{on } \partial\Omega_D\,, \tag{2.2}$$

$$\sigma_{ij} n_j = t_i^* \qquad \text{on } \partial\Omega_N\,, \tag{2.3}$$

where σ_{ij} are the components of the Cauchy stress tensor, ρ the mass density, b_i the body force, u_i the displacements, n_i the outward surface normal, Ω the body, $\partial\Omega_D$ surface region of prescribed displacements u_i^*, and $\partial\Omega_N$ surface region of prescribed tractions $\boldsymbol{t}^*$.

The total potential energy of the body is defined as

$$I[\boldsymbol{u}] = \int_\Omega W(\boldsymbol{\varepsilon})\,\mathrm{d}V - \int_\Omega \rho\boldsymbol{b}\cdot\boldsymbol{u}\,\mathrm{d}V - \int_{\partial\Omega_N} t^*\cdot\boldsymbol{u}\,\mathrm{d}S\,, \tag{2.4}$$

where $W(\boldsymbol{\varepsilon})$ is the strain energy density. Using the first variation of the total potential energy,

$$\delta I[\boldsymbol{u}] = \lim_{\epsilon\to 0}\frac{I[\boldsymbol{u}+\epsilon\delta\boldsymbol{u}] - I[\boldsymbol{u}]}{\epsilon}\,, \tag{2.5}$$

we arrive at

$$\delta I[\boldsymbol{u}] = \int_\Omega \frac{\partial W}{\partial\varepsilon_{ij}}\,\mathrm{sym}(\delta u_{i,j})\,\mathrm{d}V - \int_\Omega \rho b_i\delta u_i\,\mathrm{d}V - \int_{\partial\Omega_N} t_i^*\delta u_i\,\mathrm{d}S \tag{2.6}$$

subject to $\forall\,\delta u_i \in \mathcal{U}_0$ where $\mathcal{U}_0$ is a function space satisfying that $\delta\boldsymbol{u} = \boldsymbol{0}$ on $\partial\Omega_D$. The first variation must vanish for the total potential energy to be minimized. First, the definition of the stress tensor,

$$\sigma_{ij} = \frac{\partial W}{\partial \varepsilon_{ij}}, \tag{2.7}$$

we can rewrite Eq. (2.6) as

$$\delta I[\boldsymbol{u}] = \int_{\Omega} \sigma_{ij} \delta u_{i,j} \, \mathrm{d}V - \int_{\Omega} \rho b_i \delta u_i \, \mathrm{d}V - \int_{\partial\Omega_N} t_i^* \delta u_i \, \mathrm{d}S. \tag{2.8}$$

Second, one uses the following expression and substitutes the last term of

$$\left(\sigma_{ij}\delta u_i\right)_{,j} = \sigma_{ij,j}\delta u_i + \sigma_{ij}\delta u_{i,j} \tag{2.9}$$

into Eq. (2.8) along with the divergence theorem applied to our problem as

$$\int_{\Omega} \left(\sigma_{ij}\delta u_i\right)_{,j} \mathrm{d}V = \int_{\partial\Omega} \sigma_{ij} n_j \, \mathrm{d}S \tag{2.10}$$

to find an equivalent form of Eqn.(2.8), which results in the condition of equilibrium as

$$\delta I[\boldsymbol{u}] = \int_{\partial\Omega_N} \left(t_i^* - \sigma_{ij} n_j\right) \delta u_i \, \mathrm{d}S - \int_{\Omega} \left(\sigma_{ij,j} + \rho b_i\right) \delta u_i \, \mathrm{d}V = 0 \qquad \text{for } \delta u \in \mathcal{U}_0. \tag{2.11}$$

If one again examine the governing equations, Eqns. (2.1) – (2.3), we find that for Eq. (2.11) to hold for all admissible variations is equivalent to satisfying the original governing equations. Now let us use the first variation, Eq. (2.6) with the substitution $\delta\boldsymbol{u} = \boldsymbol{v}$ to define the *weak form*

$$G(\boldsymbol{u}, \boldsymbol{v}) = A(\boldsymbol{u}, \boldsymbol{v}) - L(\boldsymbol{v}) = 0 \; \forall \boldsymbol{v} \in \mathcal{U}_0 \tag{2.12}$$

where

$$A(\boldsymbol{u}, \boldsymbol{v}) = \int_{\Omega} \sigma_{ij} \left(\mathrm{sym}(\nabla \boldsymbol{u})\right) v_{i,j} \, \mathrm{d}V \,, \tag{2.13}$$

$$L(\boldsymbol{v}) = \int_{\Omega} \rho b_i v_i \, \mathrm{d}V + \int_{\partial\Omega_N} t_i^* v_i \, \mathrm{d}S. \tag{2.14}$$

This can then be turned into the *discrete weak from*

$$A(\boldsymbol{u}^h, \boldsymbol{v}^h) - L(\boldsymbol{v}^h) = 0 \text{ for all adm. } \boldsymbol{v}^h \,, \tag{2.15}$$

using the Bubnov-Galerkin approximation

$$\boldsymbol{u}^h(\boldsymbol{x}) = \sum_{a=1}^{n} \boldsymbol{u}^a N^a(\boldsymbol{x}) \qquad \text{and} \qquad \boldsymbol{v}^h(\boldsymbol{x}) = \sum_{a=1}^{n} \boldsymbol{v}^a N^a(\boldsymbol{x}) \,, \tag{2.16}$$

where $\boldsymbol{u}^a$ and $\boldsymbol{v}^a$ are displacements at the ath node of a finite element mesh and $N^a(\boldsymbol{x})$ is the shape function of node a. Substituting the discritized displacements from Eqn. (2.16) into Eqn. (2.12), we arrive at

$$\sum_{a=1}^{n} v_i^a \left[\int_\Omega \sigma_{ij}(\mathrm{sym}(\nabla \boldsymbol{u}^h)) N^a_{,j} \, \mathrm{d}V - \int_\Omega \rho b_i N^a \, \mathrm{d}V - \int_{\partial\Omega_N} t_i^* N^a \, \mathrm{d}S \right] = 0. \quad (2.17)$$

This equation mesh vanish for all admissible $\boldsymbol{v}^a$, which implies that the bracketed term must be zero. Rewriting Eq. (2.17) in a matrix format, we have

$$\boldsymbol{F}_{\mathrm{int}}(\boldsymbol{U}^h) - \boldsymbol{F}_{\mathrm{ext}} = \boldsymbol{0} \quad (2.18)$$

where

$$\boldsymbol{F}_{\mathrm{int}}(\boldsymbol{U}^h) = \int_\Omega \sigma_{ij}(\mathrm{sym}(\nabla \boldsymbol{u}^h)) N^a_{,j} \, \mathrm{d}V \,, \quad (2.19)$$

$$\boldsymbol{F}_{\mathrm{ext}} = \int_\Omega \rho b_i N^a \, \mathrm{d}V - \int_{\partial\Omega_N} t_i^* N^a \, \mathrm{d}S \,, \quad (2.20)$$

$$\boldsymbol{U}^h = \begin{pmatrix} \boldsymbol{u}^1 \\ \boldsymbol{u}^2 \\ \cdots \\ \boldsymbol{u}^n \end{pmatrix} . \quad (2.21)$$

In the special case of *linear elasticity* the stress is related to the displacements as

$$\sigma_{ij} = \mathbb{C}_{ijkl} u_{k,l} \,, \quad (2.22)$$

leading to the *linear elastic weak form*

$$G(\boldsymbol{u}, \boldsymbol{v}) = B(\boldsymbol{u}, \boldsymbol{v}) - L(\boldsymbol{v}) = 0 \text{ for all adm. } \boldsymbol{v} \quad (2.23)$$

where

$$B(\boldsymbol{u}, \boldsymbol{v}) = \int_\Omega v_{i,j} \mathbb{C}_{ijkl} u_{k,l} \, \mathrm{d}V \quad (2.24)$$

$$L(\boldsymbol{v}) = \int_\Omega \rho b_i v_i \, \mathrm{d}V + \int_{\partial\Omega_N} t_i^* v_i \, \mathrm{d}S \,, \quad (2.25)$$

Now the internal forces can be described in terms of the shape functions N and material tensor $\mathbb{C}_{ijkl}$ and the nodal displacemenets $\boldsymbol{u}^b$ as

$$F^a_{\text{int},i} = \int_\Omega \mathbb{C}_{ijkl} u^h_{k,l} N^a_{,j} \,\mathrm{d}V \tag{2.26}$$

$$= \sum_{b=1}^n \int_\Omega \mathbb{C}_{ijkl} u^b_k N^b_{,l} N^a_{,j} \,\mathrm{d}V \tag{2.27}$$

$$= \sum_{b=1}^n u^b_k \int_\Omega \mathbb{C}_{ijkl} N^b_{,l} N^a_{,j} \,\mathrm{d}V \tag{2.28}$$

$$= \sum_{b=1}^n u^b_k K^{ab}_{ik} \quad \text{with} \quad K^{ab}_{ik} = \int_\Omega \mathbb{C}_{ijkl} N^b_{,l} N^a_{,j} \,\mathrm{d}V. \tag{2.29}$$

Finally, we can restate the internal force vector as

$$\boldsymbol{F}_{\text{int}} = \boldsymbol{K}\boldsymbol{U}^h\,, \tag{2.30}$$

where $\boldsymbol{K}$ is the global stiffness matrix and $\boldsymbol{F}_{\text{int}}$ denotes the global force vector. Substituting this result into Eq. (2.18), we arrive at the linear set of equations

$$\boldsymbol{K}\boldsymbol{U}^h = \boldsymbol{F}_{\text{ext}}. \tag{2.31}$$

2.3 Dynamics

The governing equations of solid mechanics for linearized within the dynamic framework are

$$\sigma_{ij,j} + \rho b_i = \rho a_i \qquad \text{in } \Omega\,, \tag{2.32}$$

$$u_i(\boldsymbol{x},t) = u^*_i(\boldsymbol{x},t) \qquad \text{on } \partial\Omega_D\,, \tag{2.33}$$

$$\sigma_{ij} n_j(\boldsymbol{x},t) = t^*(\boldsymbol{x},t) \qquad \text{on } \partial\Omega_N\,. \tag{2.34}$$

Note that in comparison to the quasistatic governing equations (2.1) – (2.3) the acceleration term a_i is present in the linear momentum balance and displacements u_i and all other field variables may be a function of time.

Necessary in this derivation is the use of the action principle which states the solution $\boldsymbol{u}(\boldsymbol{x},t)$ holds A stationary with $\boldsymbol{u}(\boldsymbol{x},t_1) = \boldsymbol{u}_1(\boldsymbol{x})$ and $\boldsymbol{u}(\boldsymbol{x},t_2) = \boldsymbol{u}_1(\boldsymbol{x})$ where the action A is defined as

$$A[\boldsymbol{u}] = \int_{t_1}^{t_2} L[\boldsymbol{u}]\,\mathrm{d}t \qquad \text{with} \qquad L[\boldsymbol{u}] = T[\boldsymbol{u}] - I[\boldsymbol{u}]\,, \tag{2.35}$$

where the total potential energy I is defined in Eqn. (2.4) and the total kinetic energy T is defined as

$$T[\boldsymbol{u}] = \int_\Omega \frac{\rho}{2} |\dot{\boldsymbol{u}}|^2 \,\mathrm{d}V\,. \tag{2.36}$$

Therefore, we obtain

$$A[\boldsymbol{u}] = \int_{t_1}^{t_2} \left[\int_\Omega \left(\frac{\rho}{2} |\dot{\boldsymbol{u}}|^2 - W(\varepsilon) \right) \, \mathrm{d}V + \int_\Omega \rho \boldsymbol{b} \cdot \boldsymbol{u} \, \mathrm{d}V + \int_{\partial\Omega_N} t^* \cdot \boldsymbol{u} \, \mathrm{d}S \right] \, \mathrm{d}t \, . \tag{2.37}$$

Again, we wish to set the first variation of $A[\boldsymbol{u}]$ equal to zero. Starting with the definition of the first variation

$$\delta A[\boldsymbol{u}] = \lim_{\epsilon \to 0} A[\boldsymbol{u} + \epsilon \delta \boldsymbol{u}] - A[\boldsymbol{u}] \tag{2.38}$$

we arrive at

$$\begin{aligned} \delta A[\boldsymbol{u}] = \int_{t_1}^{t_2} \Bigg[\int_\Omega \left(\rho \dot{u}_i \delta \dot{u}_i - \sigma_{ij} \delta u_{i,j} \right) \, \mathrm{d}V \, + \\ \int_\Omega \rho b_i \delta u_i \, \mathrm{d}V + \int_{\partial\Omega_N} t_i^* \delta u_i \, \mathrm{d}S \Bigg] \, \mathrm{d}t \, . \end{aligned} \tag{2.39}$$

Similarly to the quasistatic case, we use the last term of the expanded derivative in time

$$\frac{\mathrm{d}}{\mathrm{d}t} \left(\dot{u}_i \delta u_i \right) = \ddot{u}_i \delta u_i + \dot{u}_i \delta \dot{u}_i \, . \tag{2.40}$$

Examining the first term of Eqn. (2.40) and inserting into Eqn. (2.39), one notes

$$\int_{t1}^{t2} \frac{\mathrm{d}}{\mathrm{d}t} \left(\dot{u}_i \delta u_i \right) \, \mathrm{d}t = 0 \tag{2.41}$$

given the variation $\delta \boldsymbol{u}$ vanishes at times t_1 and t_2. Therefore, along with the governing equations (2.32) – (2.34), Eqn. (2.39) yields the action principle

$$\delta A[u] = 0 \text{ for all adm. } \delta u \, . \tag{2.42}$$

The linearized-kinematics weak form of the dynamic problem thus becomes

$$\begin{aligned} G(\boldsymbol{u}, \boldsymbol{v}) = \int_{t_1}^{t_2} \Bigg[\int_\Omega \left(\rho \dot{u}_i \dot{v}_i - \sigma_{ij} v_{i,j} \right) + \\ \int_\Omega \rho b_i v_i \, \mathrm{d}V + \int_{\partial\Omega_N} t_i^* \delta v_i \, \mathrm{d}S \Bigg] \, \mathrm{d}t = 0 \text{ for all adm. } \boldsymbol{v} \, . \end{aligned} \tag{2.43}$$

Again using a discretization in space, we write the displacements as

$$\boldsymbol{u}^h(\boldsymbol{x}, t) = \sum_{a=1}^{n} \boldsymbol{u}^a(t) N^a(\boldsymbol{x}) \qquad \text{and} \qquad \boldsymbol{v}^h(\boldsymbol{x}, t) = \sum_{a=1}^{n} \boldsymbol{v}^a(t) N^a(\boldsymbol{x}) \, , \tag{2.44}$$

and the velocities are defined as

$$\dot{\boldsymbol{u}}^h(\boldsymbol{x}, t) = \sum_{a=1}^{n} \dot{\boldsymbol{u}}^a(t) N^a(\boldsymbol{x}) \qquad \text{and} \qquad \dot{\boldsymbol{v}}^h(\boldsymbol{x}, t) = \sum_{a=1}^{n} \dot{\boldsymbol{v}}^a(t) N^a(\boldsymbol{x}) \, , \tag{2.45}$$

and accelerations as

$$\ddot{\boldsymbol{u}}^h(\boldsymbol{x},t) = \sum_{a=1}^{n} \ddot{\boldsymbol{u}}^a(t) N^a(\boldsymbol{x}) \qquad \text{and} \qquad \ddot{\boldsymbol{v}}^h(\boldsymbol{x},t) = \sum_{a=1}^{n} \ddot{\boldsymbol{v}}^a(t) N^a(\boldsymbol{x}) \,. \tag{2.46}$$

Now we obtain the *discretized weak form* of the dynamic problem via Eqn. (2.43) by inserting the Galerkin approximation and multiplying by -1 we have

$$\begin{aligned} G(\boldsymbol{u}^h, \boldsymbol{v}^h) = \int_{t_1}^{t_2} \sum_{a=1}^{n} \sum_{b=1}^{n} \Bigg[\ddot{u}_i^a v_i^b \int_\Omega \rho N^a N^b \,\mathrm{d}V + v_i^b \int_\Omega \sigma_{ij} N^b_{,j} \mathrm{d}V \\ - v_i^b \int_\Omega \rho b_i N^b \mathrm{d}V - v_i^b \int_{\partial\Omega_N} t_i^* N^b \,\mathrm{d}S \Bigg] \,\mathrm{d}t = 0. \end{aligned} \tag{2.47}$$

For this to hold for all admissible $\boldsymbol{v}^a$, we can again factor out those coefficients and reduce this long and complicated expression into a set of linear equations in matrix form as

$$\boldsymbol{M}\ddot{\boldsymbol{u}}^h + \boldsymbol{F}_{\text{int}}(\boldsymbol{u}^h) - \boldsymbol{F}_{\text{ext}}(t) = \boldsymbol{0} \tag{2.48}$$

where

$$M_{ij}^{ab} = \delta_{ij} \int_\Omega \rho N^a N^b \,\mathrm{d}V \,, \tag{2.49}$$

$$F^b_{\text{int},i} = \int_\Omega \sigma_{ij} N^b_{,j} \mathrm{d}V \,, \tag{2.50}$$

$$F_{\text{ext},i} = \int_\Omega \rho b_i N^b \mathrm{d}V + \int_{\partial\Omega_N} t_i^* N^b \,\mathrm{d}S \,. \tag{2.51}$$

In this case we have derived the *consistent* mass matrix $\boldsymbol{M}$. An alternative type of mass matrix, named the *lumped* mass matrix, is obtained by lumping the mass of each element to its nodes such that $\boldsymbol{M}$ has only diagonal entries. It is also common to include velocity-proportional damping matrix $\boldsymbol{C}$ such that

$$\boldsymbol{M}\ddot{\boldsymbol{u}}^h + \boldsymbol{C}\dot{\boldsymbol{u}}^h + \boldsymbol{F}_{\text{int}}(\boldsymbol{u}^h) - \boldsymbol{F}_{\text{ext}}(t) = \boldsymbol{0} \,, \tag{2.52}$$

where

$$\boldsymbol{C} = \alpha \boldsymbol{M} + \beta \boldsymbol{K} \,, \tag{2.53}$$

where α and β are real damping parameters greater than or equal to zero.

2.4 Summary

Finite elements can be derived in a multitude of ways. In the above work, the variational approach was used to derive both the quasistatic and dynamic weak forms. The Bubnov-Galerkin approximation allows one to create discrete weak forms by introducing shape functions, ultimately leading to the finite element matrix equations.

With respect to the remainder of this document, the quasistatic formulation is the foundation for Chapters 3 and 4, while the dynamic formulation is used exclusively in Chapter 4.

Chapter 3

EFFECTIVE STIFFNESS OF HIERARCHICAL LATTICES

> *Essentially, all models are wrong, but some are useful.*
> *– George E. P. Box*

The content of this chapter is an expansion of the work presented in:

Lucas R. Meza, Alex J. Zelhofer, et al. (2015). “Resilient 3D hierarchical architected metamaterials.” In: *Proceedings of the National Academy of Sciences of the United States of America* 112.37, pp. 11502–7. ISSN: 1091-6490. DOI: `10.1073/pnas.1509120112`. URL: `http://www.pnas.org/content/112/37/11502.abstract`

3.1 Introduction

Nature has created mass-efficient and robust structural materials (Mandelbrot, 1982; Fratzl and Weinkamer, 2007; Brakus, 1995; Lakes, 1993; Ortiz and Boyce, 2008) such as bone (Currey, 2014), wood (Gibson, 2012), and glass sponges (e.g. euplectella) (Aizenberg et al., 2005). Each of these materials have their own unique microstructure containing multiple length scales via hierarchical design. Mankind has emulated the idea of structural hierarchy in buildings such as the Eiffel tower (Lakes, 1993) and the Garabit viaduct (Sundaram and Ananthasuresh, 2009) and continues to do so in the field of metamaterials. Given the recent advances in additive manufacturing, micro- and nano-lattice metamaterials have become an intense topic of focus (Deshpande, Fleck, and Ashby, 2001; Queheillalt and Wadley, 2005; Wadley, 2006; Schaedler, Jacobsen, et al., 2011; Meza and Greer, 2014; Rys et al., 2014). In this chapter, the effect of structural hierarchy on the effective stiffness of a new class of nano-architected metamaterials, viz. hierarchical nanolattices, is explored.

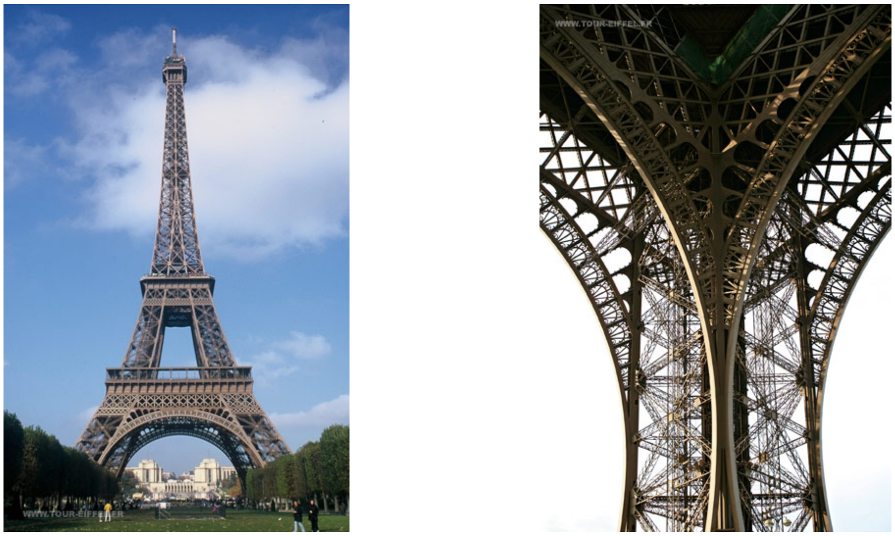

(a) Overall structure of the Eiffel Tower. Image courtesy of P. Nicou.

(b) Interior view of a tower leg showing trusses made of trusses. Image courtesy of B. Michau.

Figure 3.1: The Eiffel Tower is an example of a structure with more than four levels of hierarchy. Images are taken from (*Eiffel Tower Gallery* 2017)

Figure 3.2: The Garabit Viaduct is another example of a structure with several levels of hierarchy. Image courtesy of Graeme Churchard taken from (*Garabit Viaduct* 2009)

3.2 Hierarchical lattices

Hierarchical lattices have been studied as honeycombs (Oftadeh et al., 2014; Ajdari et al., 2012; Fan et al., 2008), cores of sandwich panels (Wadley et al., 2003; Kooistra et al., 2007), truss structures (Li and Fang, 2014), and space frames (Rayneau-Kirkhope, Mao, Farr, and Segal, 2012). An example of the hierarchical lattice used in cores of sandwich panels is shown in Fig. 3.3. Kooistra et al. (2007) found that designs with relative densities less than 5% and equal masses second-order lattice have significantly higher compressive and shear strengths than first-order lattices.

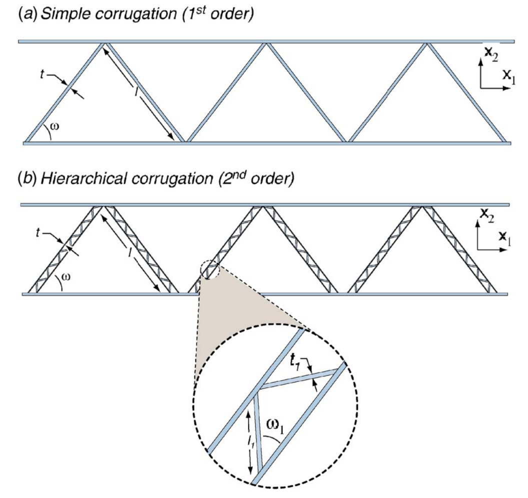

Figure 3.3: The effect of hierarchical truss core studied by Kooistra et al. (2007).

From a theoretical perspective, hierarchical structures have been approximated using solid (Farr, 2007b; Farr and Mao, 2010; Rayneau-Kirkhope, Mao, Farr, and Segal, 2012; Rayneau-Kirkhope, Mao, and Farr, 2013) and hollow beams (Farr, 2007a; Rayneau-Kirkhope, Mao, and Farr, 2012) and Euler buckling criteria to predict optimal designs. Fig. 3.4 shows first-, second-, and third-order lattice design meeting the same load requirements using deceasing amounts of material with increasing order.

Conversely, experimental realizations allow one to realize all possible deformation modes within a limited geometric parameter space such as sandwich panel cores (Kooistra et al., 2007) or three-dimensional lattices (Meza, Zelhofer, et al., 2015). To explore geometries inaccessible by theory and at a faster rate than experimentally realizable, computational modeling via FEM (Olson, 1997; Ajdari et al., 2012) is used.

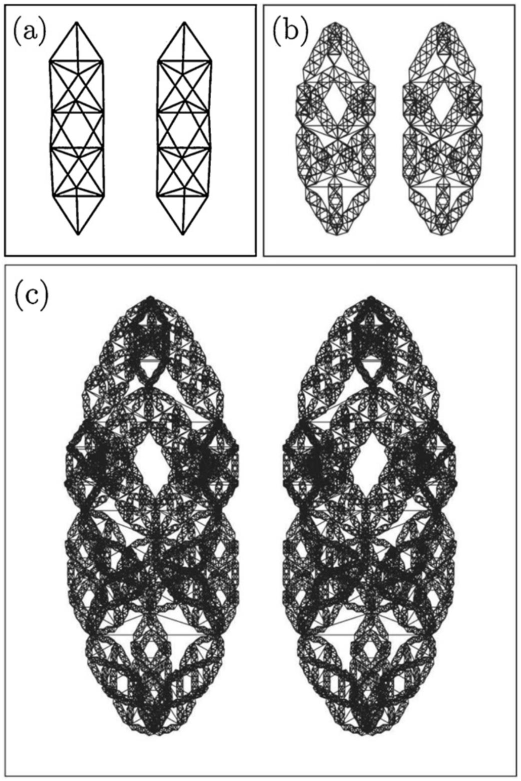

Figure 3.4: Hierarchical lattices studied by Rayneau-Kirkhope, Mao, and Farr (2012) showing (a) first-order, (b) second-order, and (c) third-order lattices able to sustain the same axial load. Relative density decreases with increasing hierarchical order. Reprinted with permission from copyright holder, Elsevier.

3.3 Modeling hierarchical lattices

The number of structural hierarchical levels in a lattice material is referred to as the *order* of the lattice as illustrated in Fig. 3.5 A. For example, a first-order lattice consists of monolithic beams. A second-order lattice's "beams" consist of first-order unit cells which in turn contain monolithic beams. With each additional level of hierarchy, the number of monolithic beams, and associated total degrees of freedom, increases by approximately two orders of magnitude. In addition, the number of computational operations of solving a linear system scales with the cube of the degrees of freedom (Anderson et al., 1999). Therefore, the number of operations necessary for computing the effective stiffness of a third-order unit cell is approximately 10^{12} times greater than the primitive unit cell. To keep the computational cost within an acceptable limit, one achieves a minimal number of degrees of freedom via either simple bar elements with minimal degrees of freedom or using higher-fidelity elements with model reduction techniques, both of which are presented here.

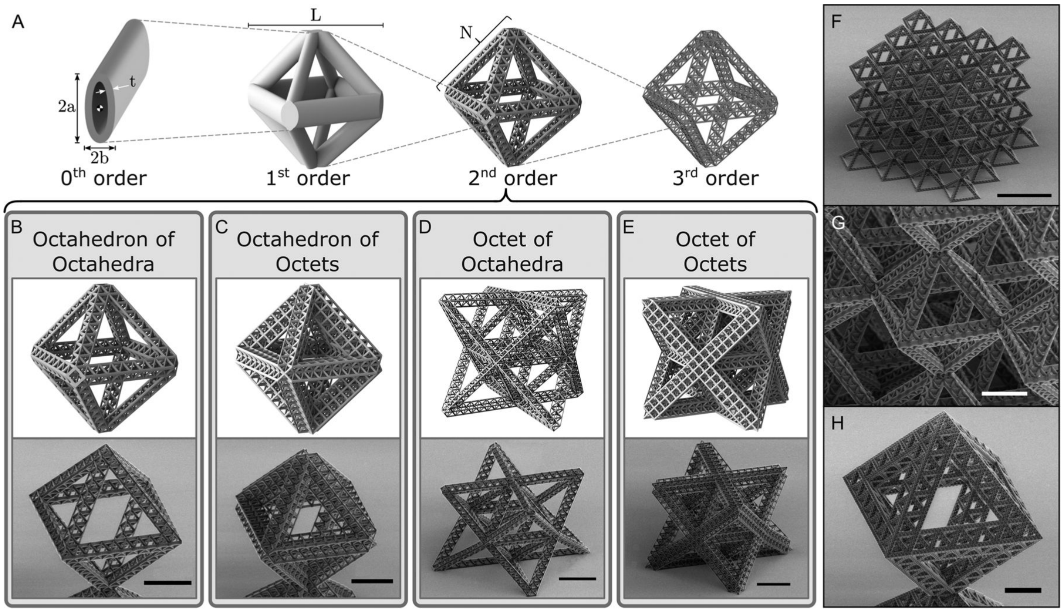

Figure 3.5: Hierarchical lattices produced using two-photon lithography. (A) Lattices are described by their order indicating the number of length scales present in an n^{th} order lattice containing $(n-1)^{th}$ order sub-components. (B–E) Renderings (white background) and SEM images (grey background) show computer generations and experimental realizations, respectfully, of second-order lattices (scale bars of 20μm). (F) Image of a second-order ocatehdron of octehedra lattice. (G) Detailed view of a second-order ocatehdron of otahedra lattice depicting the first-order lattice sub-components (scale bar: 50μm). (H) Image of a third-order octahedron of octahedra of octahedra (scale bar: 25 μm). Image taken from (Meza, Zelhofer, et al., 2015)

3.3.1 Finite element approach

Two small-strain, linear elastic, finite element approaches were used to calculate the effective stiffness of structural lattices. The first approach uses the relatively simple and computationally inexpensive truss approximation. This approach assumes lattice stiffness comes primarily from lattice member axial stiffness and ignores the effects of lattice member junctions. The second approach is the *high-fidelity method* developed to more accurately predict lattice stiffness by accounting for the stiffness of the nodes in addition to the axial and bending stiffness of the lattice members by fully resolving the 3D geometry. This method is especially effective when analyzing hollow lattices where member junctions can play a critical role in lattice stiffness. To illustrate the need for the high-fidelity method, Figs. 3.6 and 3.7 show stress distributions in a solid and hollow node, respectively, under uniaxial compression. In the case of the solid lattice, the lattice members perpendicular to the stressed member are relatively unstressed. Therefore the stiffness of the lattice is independent of junction geometry. However, in the case of a hollow node, a relatively high level of stress is present in perpendicular lattice members, indicating the stiffness of the lattice will be dependent on lattice geometry as discussed in Chapter 1.

In order to compensate for the increased degrees of freedom generated by fully resolving the geometry, a model reduction technique based on *static condensation* is employed. To predict the effective stiffness, both FEM-based methods use a hierarchical lattice half-cell constrained such that the bottom of the half-unit cell is fixed and the top is displaced vertically as shown in Fig. 3.8.

This configuration was chosen as it was the easiest geometry to manufacture without having to print multiple unit cells. Within the finite element simulations, materials are assumed to be linear elastic with constants found in Tbl. 3.1. The polymer modulus was determined by creating polymer pillars in the experimental setup and conducting compression tests. In the absence of appropriate test equipment the modulus value of alumina was taken from (Tripp et al., 2006).

Table 3.1: Material properties used in finite element calculations

Material	Young's modulus (GPa)	Poisson's ratio
Polymer	2.10	0.49
Alumina	165	0.30

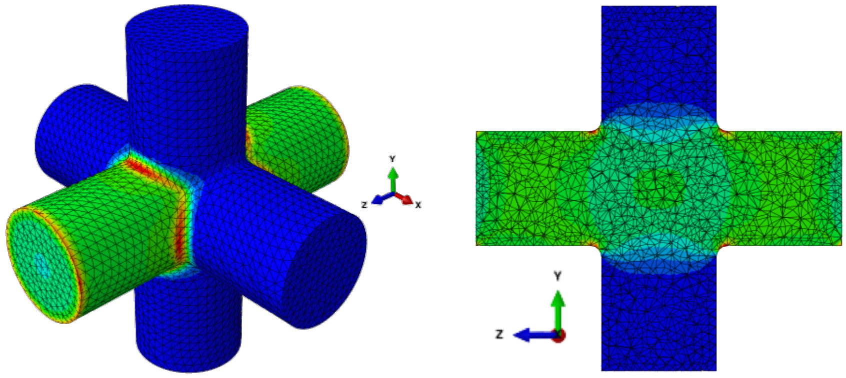

(a) Isoview

(b) Cross-section

Figure 3.6: Representative solid, three-dimensional node made of linear elastic material under uniaxial compression in the z-direction. Stress is near uniform through the stressed member with little interaction from attached members.

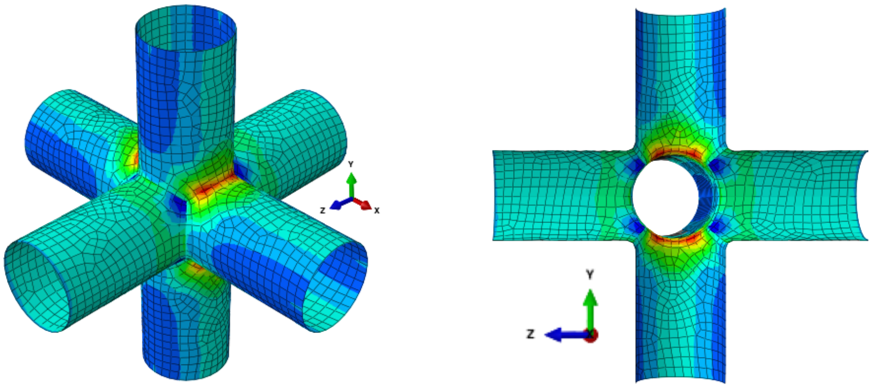

(a) Isoview (b) Cross-section

Figure 3.7: Representative hollow, three-dimensional node made of linear elastic material under uniaxial compression in the z direction. Stress is highly nonuniform through the stress member due to the interactions with the attached members.

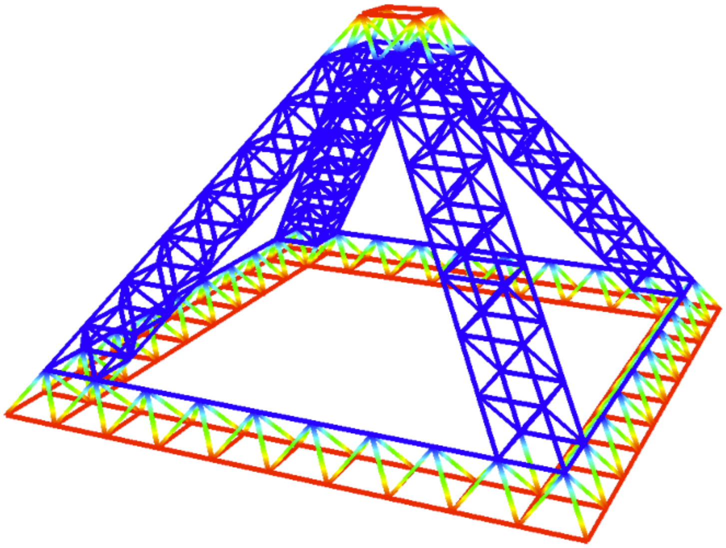

Figure 3.8: Example boundary conditions applied to simulated half cells. The bottom nodes of the structure, highlighted in red, are held fixed (i.e. $u_1 = u_2 = u_3 = 0$) and the top, also highlighted in red, has a prescribed vertical displacement δ (i.e. $u_3 = \delta$) with free movement of u_1 and u_2.

3.3.2 Truss approximation

Many analytical approaches assume lattices consist of bar or beam members (Farr and Mao, 2010; Rayneau-Kirkhope, Mao, and Farr, 2012; Rayneau-Kirkhope, Mao, Farr, and Segal, 2012; Rayneau-Kirkhope, Mao, and Farr, 2013) for analysis simplicity. The quasistatic and failure mechanisms of these idealizations are widely known and accepted. From a computational perspective, one can also choose from

Table 3.2: Three-dimensional elements considered for truss approximation

Element	Bar	Beam
axial stiffness	x	x
bending stiffness		x
torsional stiffness		x
rotational compatability at nodes		x
degrees of freedom per element	6	12

bar or beam elements as the simplest representation of a lattice member in three-dimensional space. Choosing between the two types of elements requires some background on what assumptions each element makes and how they are formulated. A brief overview is presented in Tbl. 3.2. Bar elements consist of two nodes, only providing axial stiffness along the member. Nodes are allowed to rotate freely, therefore assuming lattice member bending stiffness is negligible compared to axial stiffness. Finally, the bar element is the computationally cheapest finite element containing only six degrees of freedom per element in three dimensions. The next level in modeling fidelity is the beam element. This element accounts for axial stiffness, bending stiffness, and torsional stiffness at twice the computational cost of the bar element, having 12 degrees of freedom per element in 3D. While the beam element has a higher fidelity, the purpose of this study is to find the best-scaling finite element methodology to accurately predict hierarchical lattice stiffness.

One should also be aware of a chief assumption made when using bar elements. When modeling lattices using bar elements, one is ignoring the exact geometry of junctions between lattice members by connecting bar elements at the center of junctions as seen in Fig. 3.9. By design, bar elements only support axial loads and cannot exert a moment at the connection points.

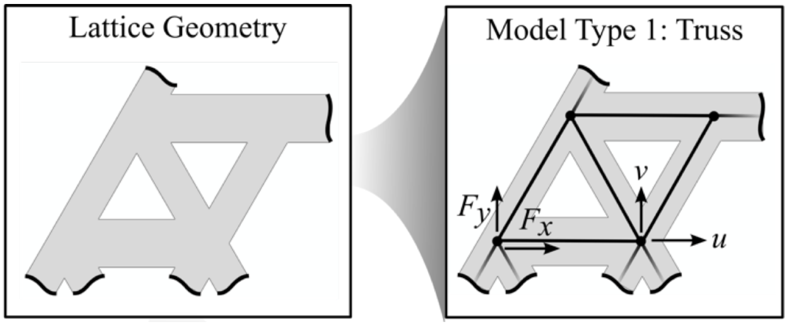

Figure 3.9: Given a particular lattice geometry, the truss method represents each lattice member by a single bar element.

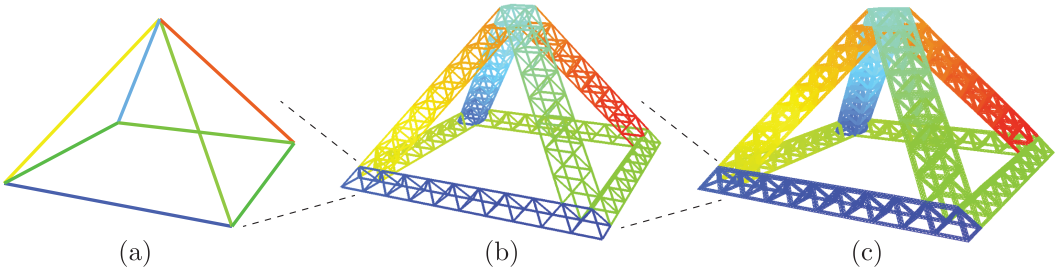
(a) (b) (c)

Figure 3.10: Truss approximations of (a) 8-member first-order, (b) 680-member second-order, (c) 65,000-member third-order half-cell lattices where each lattice member is individually colored.

In modeling single-constituent solid and hollow lattices, a single bar element is used per lattice member. However, when modeling a composite lattice of single-material core and additional material coating, a superposition of two finite element meshes was used. Fig. 3.10 shows an example of first-, second-, and third-order bar element lattices.

3.3.3 High-fidelity method

By contrast to the truss method ignoring member junction geometry and member bending stiffness, the high-fidelity method fully resolves the lattice geometry. This method makes use of 8-node continuum brick and 4-node continuum shell elements to model the different lattices. Due to the mesh density of the first-order lattice members the degrees of freedom per member are on the order of 100, 1000, and 1000 for hollow, composite, and solid-polymer members. To better understand the compounding problem of modeling hierarchical lattices, the number of floating point operations (flops) required to solve an ith-order lattice is shown in Fig. 3.11. Noting the figure is in log scale, one sees that without any type of model-reduction technique the size of the problem to be solved grows by several decades. Hence, to model any lattice in an efficient manner, the so-call static condensation model-reduction technique is utilized, starting from the smallest length scale to the largest scale.

The static condensation method (Guyan, 1965; Wilson, 1974; Qu, 2013), otherwise known as Guyan condensation, allows one to significantly reduce the computational costs of a finite element problem. This is achieved by eliminating degrees of freedom not being acted upon by external forces, essential boundary conditions, or coupled to other assemblies. This technique is useful when analyzing large, complex interacting parts, especially if the parts are repeated in the assembly such

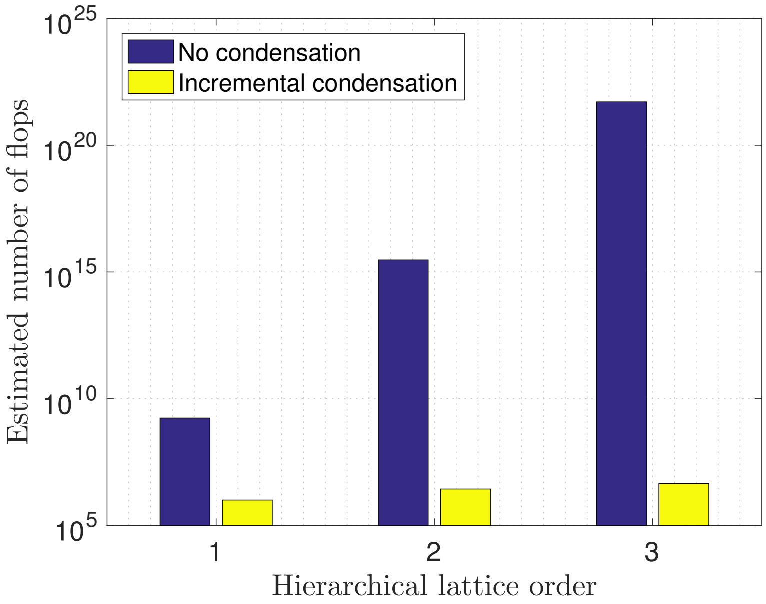

(a) Hollow lattices made of octahedron unit cells on each length scale with 10 unit cells per hierarchical member.

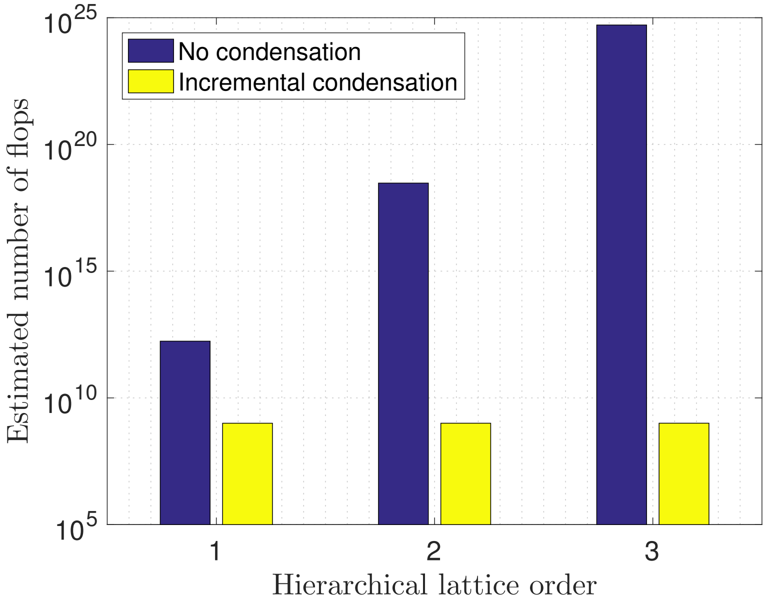

(b) Solid lattices made of octahedron unit cells on each length scale with 10 unit cells per hierarchical member.

Figure 3.11: The number of floating point operations (flops) estimated to solve a high-fidelity, hollow or solid, octahedron, first-, second-, or third-order hierarchical lattice. Comparison is between solving a system with and without incremental condensation at each level of hierarchy.

as in the analysis of vehicles, buildings, or periodic media. The method can be used to efficiently model any lattice with minimal loss in accuracy. When static condensation is applied to parts or assemblies, the result is commonly referred to as a *super-element*. In the specific case of metamaterial lattices, a finite set of nodes and beams can be individually condensed into super-elements and connected together to form the lattice geometry. Furthermore these super-elements, referred to as *super-nodes* and *super-beams* can be assembled, connected, and condensed again to create larger condensed assemblies. The following details how static condensation is realized.

Consider a general linear finite element problem of the form

$$\boldsymbol{K}\boldsymbol{u} = \boldsymbol{f}_{\text{ext}}\,, \tag{3.1}$$

where $\boldsymbol{K}$ is the stiffness matrix, $\boldsymbol{u} \in \mathbb{R}^{(m+s)}$ is the assembled, global displacement vector, and $\boldsymbol{f}_{\text{ext}}$ is the external force vector. One can rearrange the order of linear equations represented in Eq. (3.1) to group together nodes to be condensed out ($\boldsymbol{u}_s \in \mathbb{R}^s$) and nodes to keep ($\boldsymbol{u}_m \in \mathbb{R}^m$) using the permutation matrix $\boldsymbol{A}$ (with $\boldsymbol{A}^{\mathrm{T}}\boldsymbol{A} = \boldsymbol{I}$) so that we have

$$\boldsymbol{A}\boldsymbol{K}\boldsymbol{A}^{\mathrm{T}}\boldsymbol{A}\boldsymbol{u} = \boldsymbol{A}\boldsymbol{f}\,, \tag{3.2}$$

where

$$\boldsymbol{A}\boldsymbol{u} = \begin{bmatrix} \boldsymbol{u}_m \\ \boldsymbol{u}_s \end{bmatrix}, \quad \boldsymbol{A}\boldsymbol{K}\boldsymbol{A}^{\mathrm{T}} = \begin{bmatrix} \boldsymbol{K}_{mm} & \boldsymbol{K}_{ms} \\ \boldsymbol{K}_{sm} & \boldsymbol{K}_{ss} \end{bmatrix}, \quad \boldsymbol{A}\boldsymbol{f} = \begin{bmatrix} \boldsymbol{f}_m \\ \boldsymbol{f}_s \end{bmatrix}. \tag{3.3}$$

Expressing Eq. (3.2) using terms from Eq. (3.3), we obtain the rearranged form as

$$\begin{bmatrix} \boldsymbol{K}_{mm} & \boldsymbol{K}_{ms} \\ \boldsymbol{K}_{sm} & \boldsymbol{K}_{ss} \end{bmatrix} \begin{bmatrix} \boldsymbol{u}_m \\ \boldsymbol{u}_s \end{bmatrix} = \begin{bmatrix} \boldsymbol{f}_m \\ \boldsymbol{f}_s \end{bmatrix}. \tag{3.4}$$

From the second line of matrix equations of Eq. (3.4) one can solve for the condensed nodes as

$$\boldsymbol{u}_s = \boldsymbol{K}_{ss}^{-1}\left(\boldsymbol{f}_s - \boldsymbol{K}_{sm}\boldsymbol{u}_m\right) \tag{3.5}$$

and then substitute into the first line of Eq. (3.4) to obtain

$$\boldsymbol{K}_{mm}\boldsymbol{u}_m + \boldsymbol{K}_{ms}\left(\boldsymbol{K}_{ss}^{-1}\left(\boldsymbol{f}_s - \boldsymbol{K}_{sm}\boldsymbol{u}_m\right)\right) = \boldsymbol{f}_m. \tag{3.6}$$

Once rearranged, this becomes the condensed problem

$$\tilde{\boldsymbol{K}}_{mm}\boldsymbol{u}_m = \tilde{\boldsymbol{f}}_m\,, \tag{3.7}$$

where $\boldsymbol{u} \in R^m$ and the condensed stiffness matrices are defined as

$$\tilde{\boldsymbol{K}}_{mm} = \boldsymbol{K}_{mm} - \boldsymbol{K}_{ms}\boldsymbol{K}_{ss}^{-1}\boldsymbol{K}_{sm}, \tag{3.8}$$

$$\tilde{\boldsymbol{f}}_{m} = \boldsymbol{f}_{m} - \boldsymbol{K}_{ms}\boldsymbol{K}_{ss}^{-1}\boldsymbol{f}_{s}. \tag{3.9}$$

When applying condensation to lattices, one looks for unique geometry in lattice members and member junctions as shown in Fig. 3.12 for a second-order lattice. Each one of these unique members and nodes is fully resolved, meshed, and condensed as shown in Fig. 3.13. Additional degrees of freedom are added to condensed super-elements, creating assembly connection points where nodes on the connected faces are kinematically tied to the mating surface. Each of these unique condensed super-elements (Fig.3.14) can then be assembled into a first-order lattice (as seen in Fig. 3.15) and condensed again. In order to minimize the total computational time when modeling an *n*th-order hierarchical lattice, one condenses all lower-order lattice subcomponents and solves for the displacements of the assembled subcomponents.

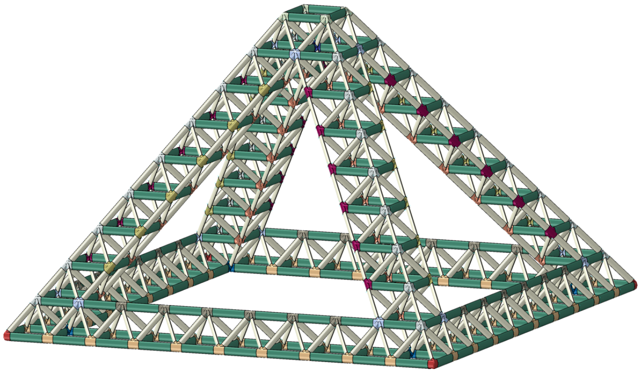

Figure 3.12: Second-order, octahedron of octahedra (N=10) half-cell colored by unique beam and nodal geometry.

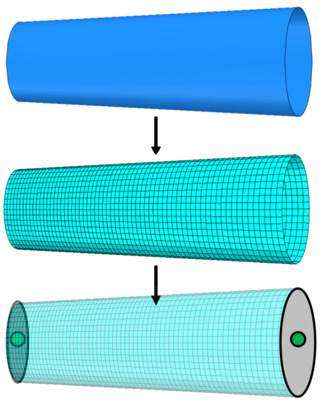

Figure 3.13: Work flow process of creating a hollow super-beam . The geometry (blue) is formed, the full mesh (light green) is generated, and finally connecting nodes (dark green) are added to the ends of the beam allowing for connections between the super-beam and a super-node.

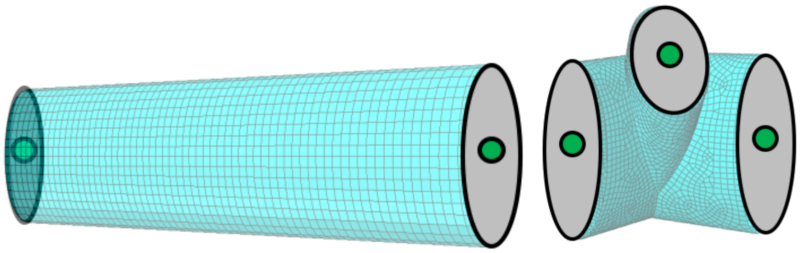

(a) Beam super-element

(b) Nodal super-element

Figure 3.14: Representative constituent super-elements of a first-order lattice. Light green mesh represents condensed nodes while the dark green circles represent master nodes used to connect beam and nodal super-elements. Master nodes are kinematically coupled to all nodes on the face of the respective cross-section as to create an infinitely stiff plate between the master and condensed degrees of freedom.

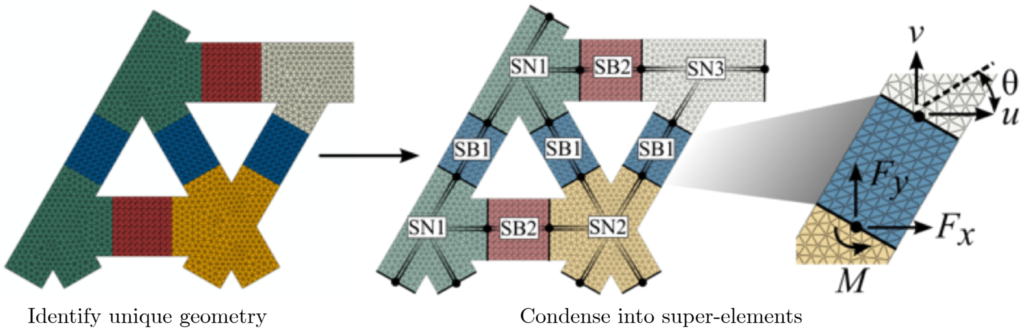

Figure 3.15: High-fidelity model work flow showing super-elements connected at single points capable of translations and rotations in all directions (shown in 2D).

3.3.4 Experimental validation

The experimental realization of hierarchical lattices via two-photon lithography, atomic layer deposition, and their testing by nano-indenter compression tests was performed by Lucas Meza in Prof. Julia R. Greer's group at Caltech. Example compression tests are shown in Fig. 3.18. Each sample was compressed to fifty percent of its original height and the associated compression force was recorded. Effective structural linear elastic moduli were extracted from the linear portion of the force displacement curve. Further details of the experimental fabrication and testing can be found in (Meza, Zelhofer, et al., 2015)

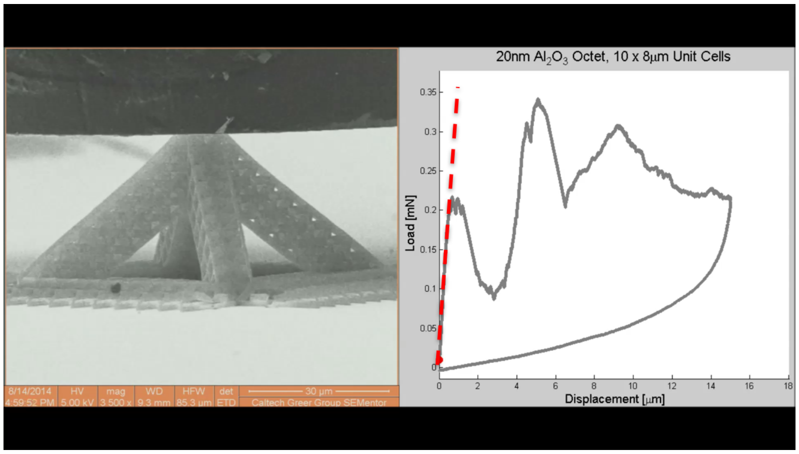

(a) Second-order hierarchical octahedron half-cell made with $N = 10$ first-order octet unit cells.

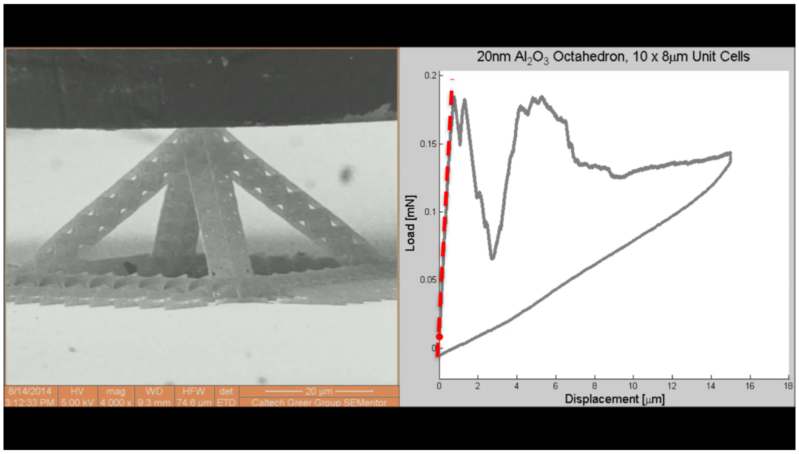

(b) Second-order hierarchical octahedron half-cell made with $N = 10$ first-order octahedron unit cells.

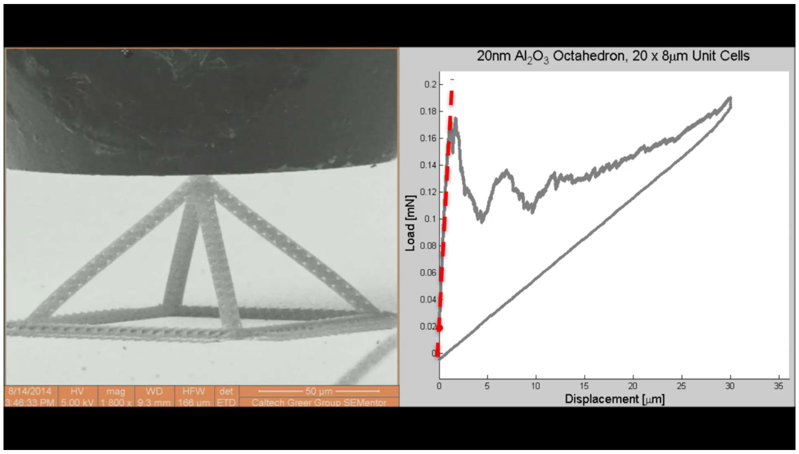

(c) Second-order hierarchical octahedron half-cell made with $N = 20$ first-order octahedron unit cells.

Figure 3.16: Displacement controlled compression tests of second-order, hollow alumina half-cells with 20 nm wall thickness. Left images show the experimental setup and right images the measured force vs. displacement. Dashed red lines indicate the fitted linear stiffness.

3.4 Results

Comparisons are made between the computationally predicted and experimentally measured effective stiffness of second-order half-cell solid polymer, polymer-ceramic composite, and hollow alumina lattices as geometrically described in Appendix Tbl. A.1. Two derived quantities of stiffness are used to compare the finite element predicted and experimentally measured values: effective structural stiffness and effective material stiffness. *Effective structural stiffness* comes from considering the tested unit cell of a structure and is defined as the reaction force to displacing the top of the half-cell divided by the applied displacement, is shown qualitatively in Fig. 3.17 and quantitatively in Fig. 3.18. Whereas *effective material stiffness* views the nanolattices as a metamaterial and divides the reaction force by the effective footprint of the half-cell and the displacement by the original height, so that stiffness results from the thus obtained ratio of effective stress and strain.

In general, relative to the truss method the high-fidelity method predicts a higher effective stiffness for solid cross sections (solid polymer and composite) and a lower effective stiffness for hollow (alumina) nodes. This effect can be attributed to the high-fidelity method accounting for lattice junction geometry, where solid junctions add stiffness and hollow nodes introduce compliance. With respect to experimental results the high-fidelity method overpredicts the composite and hollow lattices by 30.2% and 68.5 %, respectively. This large inaccuracy is attributed to geometric imperfections induced in the manufacturing process such as curved beams, lattice member junction misalignment, or, as seen in several samples, sinusoidal waviness of the first-order beams. In a brief computational study the effect of a 50 nm-amplitude, 1 micron-wavelength sinusoidal shape reduced axial stiffness of first-order members by 5%, 32%, and 70% for solid polymer, composite, and hollow lattices, respectively. A more general study of truss waviness is presented in the next section.

As seen from all three material system simulations and experiments shown in Fig. 3.19, hierarchical lattices can span three orders of magnitude in relative density and four orders of magnitude in effective stiffness. Additionally, second-order lattices are shown to achieve near-ideal linear scaling with relative density for the given geometric configurations.

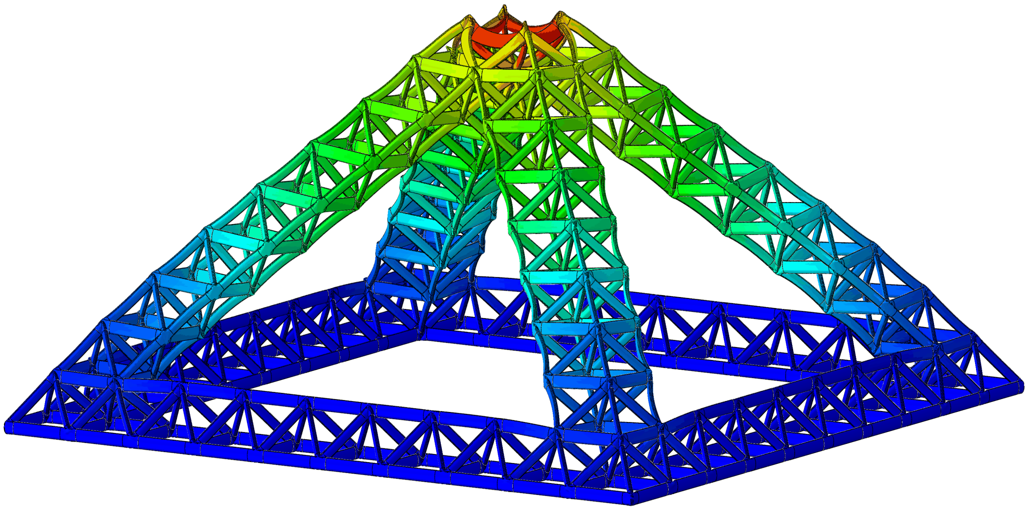

Figure 3.17: Second-order octahedron of octahedra half-cell lattice colored by displacement. The displayed deformed state of this linear perturbation analysis is magnified by a factor of 1000.

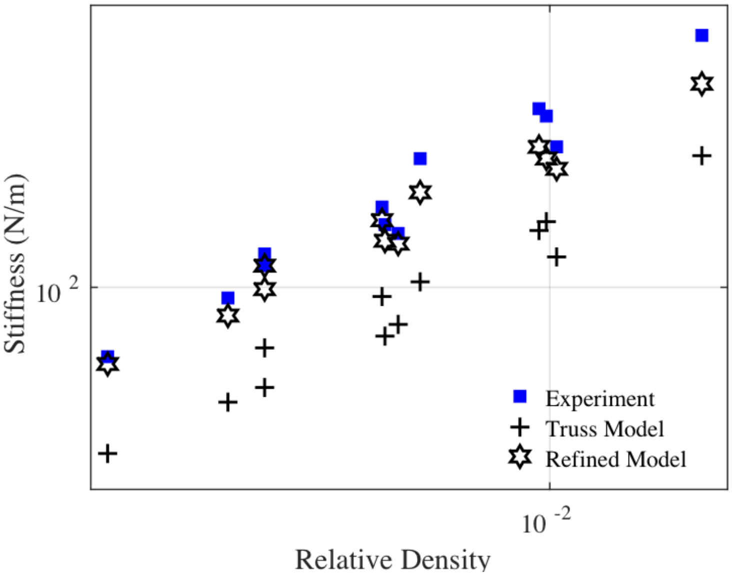

(a) Polymer lattices

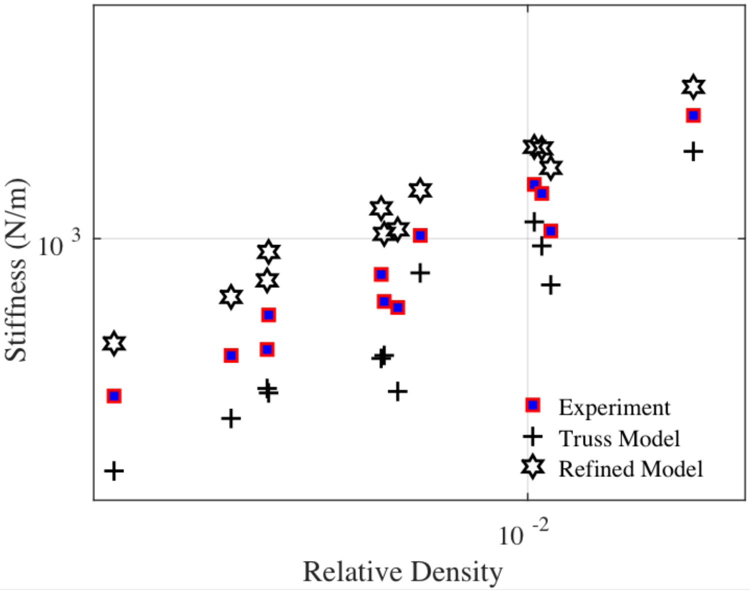

(b) Alumina coated polymer lattices

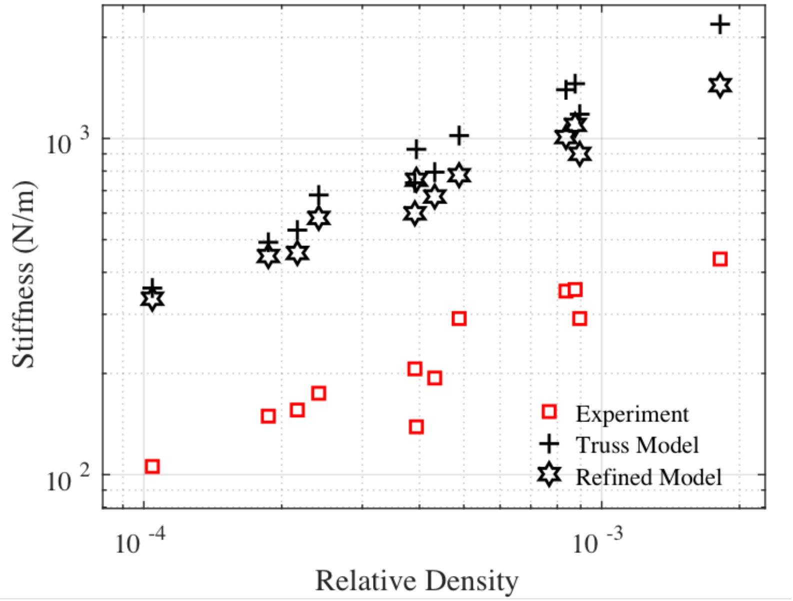

(c) Hollow alumina lattices

Figure 3.18: Comparison of structural stiffness values of second-order hierarchical lattice, half-cell truss and refined models against experiments, where stiffness is defined as the force necessary to deform the structure by a unit displacement.

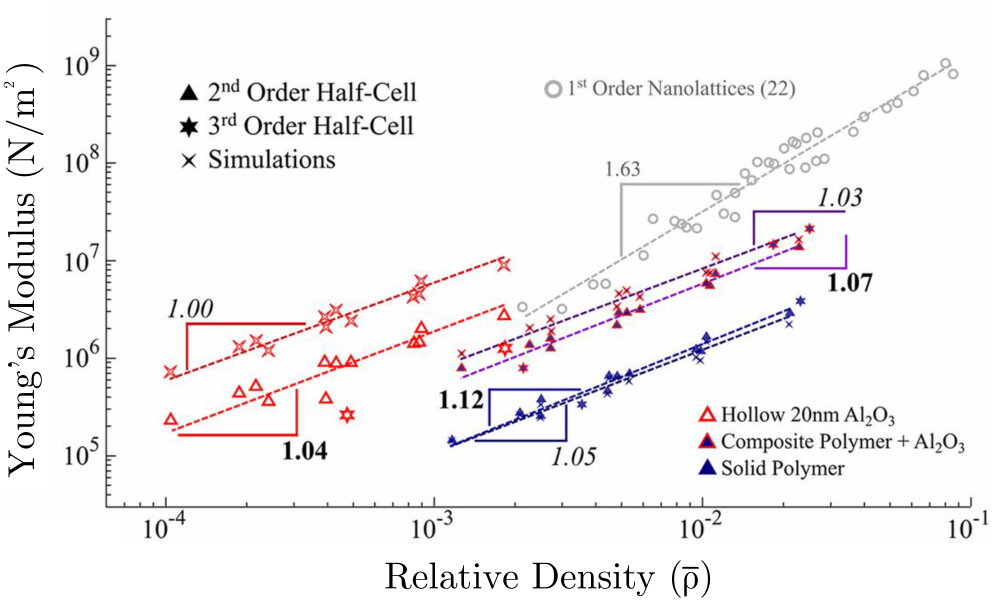

Figure 3.19: Comparison of the effective material stiffness of first-, second-, and third-order lattices. First-order data comes from (Meza, Das, et al., 2014).

3.4.1 Geometric imperfections

As with any manufacturing process, and additive manufacturing is no exception, the parts produced are susceptible to imperfections. Shown below in Figs. 3.20a and 3.20b are two possible types of geometric imperfections from two different manufacturing processes. The first, shown in Fig. 3.20a and referred to as stepping, is due to individual layers being printed with low resolution compared to the size of the lattice member being printed. The second imperfection, shown in Fig. 3.20b, present in two-photon lithography is due to external vibration of the Nanoscribe. Both of these geometric imperfections could be mitigated by considering a larger lattice structure such that layers and vibration amplitudes are sufficiently small compared to the lattice members. However, if this is not an option, one must consider how such imperfections will affect the printed lattice.

Picking one of the two types of geometric imperfection, the following is a finite element study focusing specifically on how the waviness of a lattice member affects the axial stiffness of the member. Fig. 3.22 shows the parameterization of a single-wavelength, solid beam with length L, diameter D, and waviness described by a sinusoidal shape of the beam's neutral axis with amplitude a, subjected to periodic boundary conditions on faces A and B. The effect of two ratios, length to diameter L/D and waviness amplitude to diameter a/D, are studied and shown in Fig. 3.22.

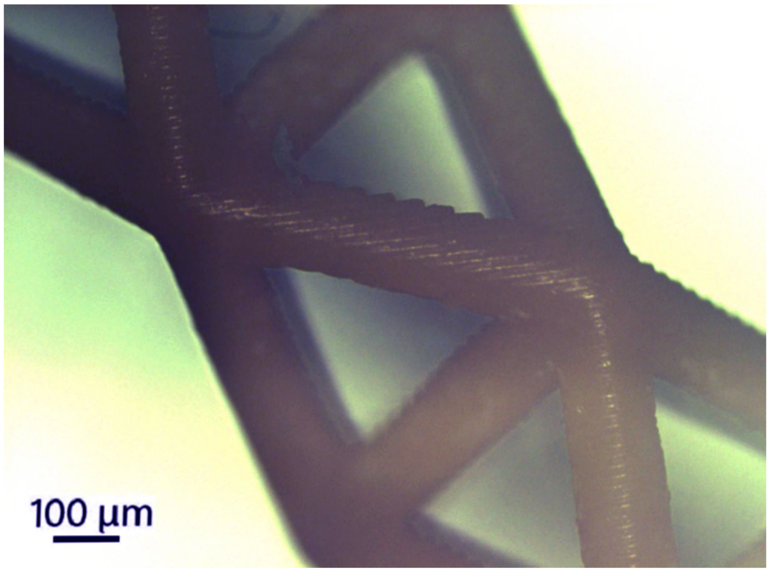

(a) Stepping defect present in micro lattices. Reprinted from (Rayneau-Kirkhope, Mao, Farr, and Segal, 2012) with permission from copyright holder, Elsevier.

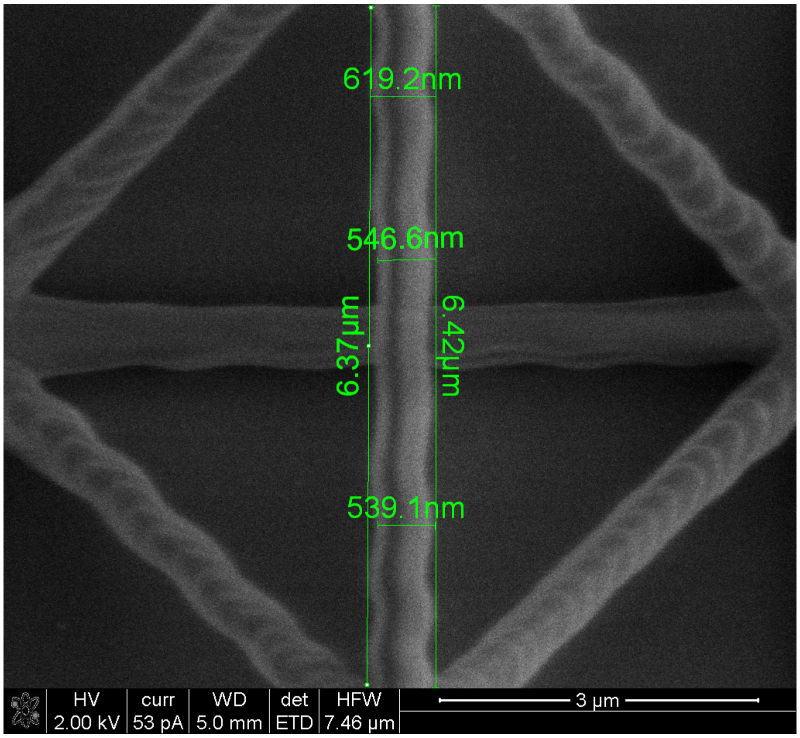

(b) Lattice member waviness and stepping present in nano lattices. Image courtesy of Lucas Meza from Prof. Julia R. Greer's group at Caltech.

Figure 3.20: Two possible geometric imperfections in additively manufactured lattices: stepping and waviness.

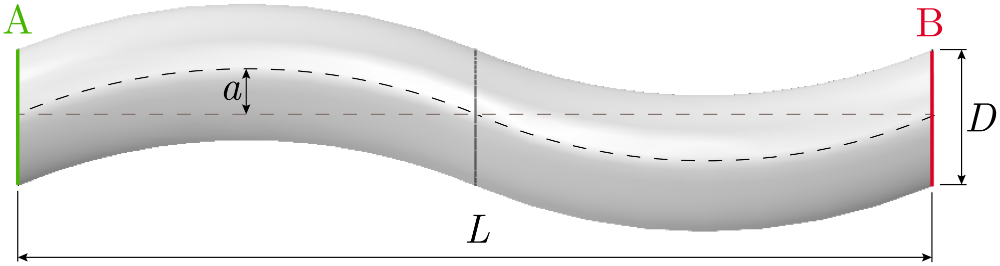

Figure 3.21: Parameterization of a single-wavelength wavy beam characterized by a sinusoidal shape of the beam's neutral axis with amplitude a.

The axial stiffness of the wavy beam is normalized by the stiffness of the equivalent-length-and-diameter straight beam, providing the fraction of stiffness retained. The amplitude-to-diameter ratio is shown to have a significantly larger effect on stiffness reduction than the length to diameter ratio. If we take dimensions from the example shown in Fig. 3.20b, the length of the beam is 6.37 μm, its diameter is 540 nm,

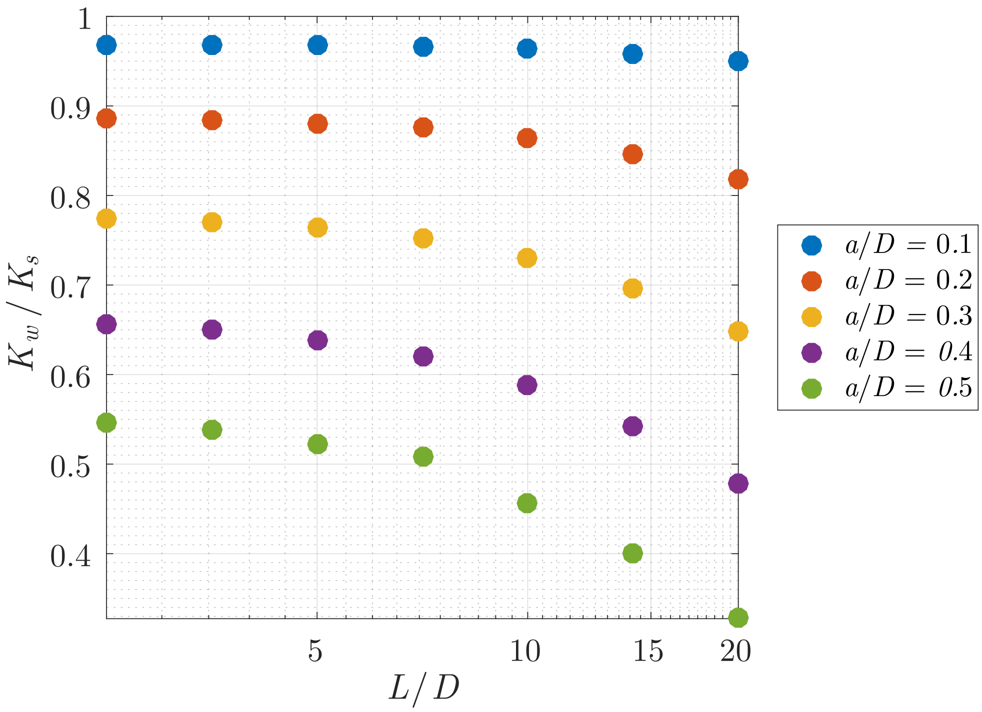

Figure 3.22: Study of the effect of waviness on the axial stiffness of a lattice member. The axial stiffness of a solid, circular cross-section wavy beam K_w normalized by the stiffness of an equivalent diameter straight beam K_s. Different ratios of length to diameter and waviness amplitude to diameter are explored.

and the waviness amplitude is estimated to be 40 nm, therefore $L/D \approx 12$ and $a/D \approx 0.075$. Upon re-examination of Fig. 3.22 it becomes apparent that this decreases the stiffness by at most 5%. However, if the lattice member of the same length, diameter, and waviness amplitude is a polymer coated by a stiffer ceramic or a hollow ceramic shell one could observe stiffness decreases on the order of 30% and 70%, respectively (Meza, Zelhofer, et al., 2015).

3.5 Summary

Hierarchical structures, both natural and man-made, have been shown to improve mass utilization in terms of stiffness and strength. Building structures such as the Eiffel tower and Garabit Viaduct make use of multiple length scales to achieve mass-efficient structures on the meter scale. This same idea is applied on smaller scales to nanoscale lattice materials. Theoretical predictions have shown increasing levels of hierarchy can reduce material use while supporting the same load. In an effort to explore the effect of hierarchy, a computational methodology has been developed and applied to nanoscale hierarchical materials.

Modeling hierarchical lattices requires thousands to millions of truss members while simultaneously accounting for all deformation modes. To this end, two strategies were developed to model lattice materials: the truss method and high-fidelity method. The truss method used the simplest and least computationally expensive of elements supporting only axial loads, the bar element. These elements connect exactly at member junctions and are unable to account for the added stiffness or compliance of the node. In comparison, the more geometrically accurate and predictive high-fidelity method uses higher-order elements coupled with the model-reduction technique static condensation. This reduction technique is necessary to reduce the number of computational floating point operations to a manageable level, sometimes as much as by 10^{10} operations.

Finite element simulations show hierarchical lattices are capable of near-ideal stretching-dominated scaling at relative densities as low as 10^{-4} for the geometric parameters tested. Geometric imperfections in the form of waviness are shown to have a potentially large impact on the effective stiffness of a lattice material depending on the amplitude of the waviness and length-to-diameter ratio of the lattice member.

Chapter 4

BEAMING IN STRUCTURAL LATTICES

> *If you want to find the secrets of the universe, think in terms of energy, frequency and vibration.*
> *—- Nikola Tesla*

The contents of this chapter is an expansion of work presented in:

Alex J. Zelhofer and Dennis M. Kochmann (2017). “On acoustic wave beaming in two-dimensional structural lattices”. In: *International Journal of Solids and Structures* 115, pp. 248–269

4.1 Introduction

The analysis of wave motion in periodic systems can be traced back to Rayleigh’s studies of string vibration (1887) and Brillouin’s analysis on lattice vibrations (Brillouin, 1953). Subsequently, analyses expanded to periodic mechanical structures (Abrahamson, 1973; Mead, 1973), composite materials (Sun et al., 1968; Nemat-Nasser, 1972; Z. Liu et al., 2002; Sigmund and Jensen, 2003; Mace and Manconi, 2008), phononic crystals (Economou and M. M. Sigalas, 1992; M. Sigalas and Economou, 1993; Kushwaha and Halevi, 1994; Vasseur et al., 1994; Kushwaha, 1996) and acoustic metamaterials (Z. Liu, 2000), with applications ranging from aircraft structures (Manconi and Mace, 2009) and turbines (Ewins, 1973; Griffin and Hoosac, 1984; Ottarsson et al., 1997) to cellular materials (Deshpande and Fleck, 2000; Akil Hazizan and Cantwell, 2002; Fleck and Deshpande, 2004) or even at scales of buildings and bridges (Talbot and Hunt, 2003; Boa et al., 2012; Brun et al., 2013). As one can see specific arrangement of periodic building blocks in discrete geometries gives rise to the controllable dispersion of linear waves and the associated frequency- and direction-dependent wave attenuation and wave guiding.

Numerous methods study linear wave motion in periodic structures, starting with Hamiltonian systems such as spring-mass configurations (Brillouin, 1953) and one-dimensional beams (Cremer and Leilich, 1953). Further techniques developed afterwards include the receptance methods (Mead, 1970; Mead, 1975), direct solution of the differential equations of motion (Mead, 1971b), transfer matrix methods

(Lin and McDaniel, 1969; Faulkner and Hong, 1985), energy methods (Mead, 1973; Mead and Mallik, 1976; Mead and Parthan, 1979; Abdel-Rahman and Petyt, 1980), and space-harmonic analysis (Mead, 1971a). One of the first applications of finite element (FE) analysis was by Orris and Petyt, 1974 studying wave motion in one-dimensional beams and rib-skin structures.

From the diverse field of linear wave dispersion, focus is placed on *wave beaming* (i.e., directional energy flow) in unconstrained structural lattices as acoustic metamaterials generated using periodic tessellation of a single *representative unit cell* (RUC) composed of linear elastic beams. Lattice materials have attracted attention in recent years, owing to the enhanced additive manufacturing capabilities and ability to control effective, macroscopic metamaterial properties by microscale architecture. Examples include trusses with high stiffness and strength (Meza, Zelhofer, et al., 2015), improved energy absorption (Shan et al., 2015; Meza, Das, et al., 2014) or even mechanically superior cellular solids (Torquato et al., 1998; Gibson and Ashby, 1988; Christensen, 2000; Evans et al., 2001; Wadley et al., 2003; Wadley, 2006; Hutchinson and Fleck, 2006; Fleck, Deshpande, and Ashby, 2010). Structural lattices also admit elastic stress wave control and continue to be of topical interest for wave guiding, see, e.g. Zimmerman (2003) and Hussein et al. (2014).

When mechanically excited, structural lattices exhibit frequency dispersion due to frequency-dependent phase and group velocities. The interference of waves promotes frequency-dependent wave attenuation, referred to as *stop-bands*. Full stop-bands (i.e., direction-independent wave attenuation) have been prominently achieved through concepts of local resonance, see, e.g. (Martinsson and Movchan, 2002; Yu, Y. Liu, G. Wang, Cai, et al., 2006; Yu, Y. Liu, G. Wang, Zhao, et al., 2006; Y. Liu et al., 2007; L. Liu and Hussein, 2012; Krödel et al., 2013; P. Wang et al., 2015), while partial (i.e., directional) stop-bands and wave beaming have most commonly been created by specific structural architecture (Ruzzene, Scarpa, and Soranna, 2003).

Beaming of out-of-plane wave motion in two-dimensional (2D) structures was probably first studied by Langley, 1994 for a periodic plate assembly, followed by analyses of 2D rectangular grids of beams under harmonic forcing (Langley, 1996; Langley, 1997a) and impulse loading (Langley, 1997b). Since then, wave guiding has been investigated in various 2D and 3D lattices. In 2D, beaming can be associated with in-plane or out-of-plane wave propagation, or both. Prominent in-plane studies have focused on auxetic and non-auxetic hexagonal lattices (Gonella and Ruzzene, 2008b;

Gonella and Ruzzene, 2008c), kagome lattices (Niu and B. Wang, 2016), chiral lattices (Spadoni et al., 2009), and the topological transition from truss-like unit cells to continuum (meta)materials (Casadei and Rimoli, 2013). Out-of-plane investigations studied plates with truss-like cores (Kohrs and Petersson, 2009), honeycomb-filled composites (Ruzzene, Mazzarella, et al., 2002), auxetic and non-auxetic hexagonal lattices (Ruzzene, Scarpa, and Soranna, 2003), chiral honeycombs (Tee et al., 2010), and cross-braced rectangular lattices (Jeong and Ruzzene, 2004; Jeong and Ruzzene, 2005). Owing to the considerably lower associated stiffness, out-of-plane motion occurs generally at lower frequencies, comes with larger amplitudes for a given excitation, and is easier to excite. Besides, most technological applications of 2D structural lattices (such as for impact protection (Qiao et al., 2008) or acoustic insulation (Z. Liu, 2000)) emphasize out-of-plane deformation modes.

Here, focus is placed on out-of-plane wave motion in 2D periodic lattices with the goal of predicting architecture- and frequency-dependent beaming. This is commonly accomplished by either direct numerical simulations (integrating the equations of motion over time) or by indirect methods predicting the complete effective dynamic response. The former is straight-forward but, prohibitively computationally expensive, which is why it is commonly used for verifying beaming predictions rather than predicting the complex lattice response. The latter is challenging because the response of an infinite structure must be approximated, e.g. by the plane wave expansion method, finite difference methods, or the multiple scattering method, see, e.g. (Hussein et al., 2014) for an overview, or by the finite element (FE) method by assuming Bloch-type plane waves and computing the dispersion relations (Orris and Petyt, 1974; Aberg, 1997; Phani et al., 2006). Although popular in the community, dispersion relations reveal only limited information when it comes to directional energy transport, especially when a specific path in the irreducible Brillouin zone is investigated, as was shown by Jeong and Ruzzene (2004). Therefore, prior studies resorted to *phase constant surfaces* (Langley, 1994) and specifically predicted wave motion based on the lowest surface(s), see, e.g. (Ruzzene, Scarpa, and Soranna, 2003; Ruzzene and Scarpa, 2005; Wen et al., 2008; Gonella and Ruzzene, 2008a). In the following a new visualization technique is established to highlight directional wave attenuation across surfaces and frequency ranges providing the accurate prediction of directional stop-bands and wave beaming. The methodology is applied to 2D periodic lattices of three different fundamental unit cells, and comparison are made between beaming predictions based on dispersion relations to direct dynamic calculations. In both cases, the finite element method is used along with linear elastic Euler-Bernoulli beam theory to describe the response of truss lattices.

The remainder of this chapter is structured as follows, Section 4.2 briefly summarizes the underlying theory of linear wave motion, followed by a description of the numerical implementation used and the specific lattice geometries investigated here in Sections 4.3 and 4.4, respectively. Results are presented in Section 4.5, and Section 4.7 summarizes the findings.

4.2 Theory of linear wave motion

A brief review of the theory of wave dispersion in periodic media is provided. The methodology presented here was first developed for harmonic lattices (Brillouin, 1953) and has been applied successfully to general periodic media. For a given RUC we seek the dispersion relation and determine beaming in infinite lattices via the gradient of each dispersion relation surface also known as *phase constant surface*.

4.2.1 Wave propagation in periodic media

Due to the separable, linear form of linear momentum balance, wave propagation in a linear elastic lattice $\Omega \subset \mathbb{R}^d$ is based on a time-harmonic displacement field of the form

$$\boldsymbol{u}_m(\boldsymbol{r}, t) = \boldsymbol{U}_m(\boldsymbol{r}) \exp(-i\omega t), \tag{4.1}$$

where $\boldsymbol{U}_m : \Omega \to \mathbb{C}^{d+1}$ is a generally complex-valued amplitude field in $d + 1$ dimensions, $\omega \in \mathbb{R}$ is the wave frequency, t denotes time and $\boldsymbol{r}$ position (note that the actual solution is the real part of (4.1), which is implied in the following). By exploiting the spatial periodicity of a lattice, described by a set of d Bravais basis vectors $\{\boldsymbol{e}_1, \ldots, \boldsymbol{e}_d\}$ (which are not necessarily orthogonal), we employ Bloch's theorem (Brillouin, 1953) which uniquely links the motion of any point in the lattice to the motion in a representative unit cell (RUC) by

$$\begin{aligned} \boldsymbol{U}_m(\boldsymbol{r}) &= \boldsymbol{U}_m\big(\boldsymbol{r}_{\text{RUC}}(\boldsymbol{r})\big) \exp\left[i\boldsymbol{k} \cdot \big(\boldsymbol{r} - \boldsymbol{r}_{\text{RUC}}(r)\big)\right] \\ &= \boldsymbol{U}_m\big(\boldsymbol{r}_{\text{RUC}}(\boldsymbol{r})\big) \exp\left[i\boldsymbol{k} \cdot \sum_{\alpha=1}^{d} n_\alpha \boldsymbol{e}_\alpha\right] \end{aligned} \tag{4.2}$$

with wave vector $\boldsymbol{k} = \boldsymbol{k}^{\text{Re}} + i\boldsymbol{k}^{\text{Im}} \in \mathbb{C}^d$, where $\boldsymbol{k}^{\text{Re}} \in \mathbb{R}^d$ and $\boldsymbol{k}^{\text{Im}} \in \mathbb{R}^d$ represent, respectively, the attenuation and phase constants. Each position $\boldsymbol{r}$ is linked to a unique point $\boldsymbol{r}_{\text{RUC}}(\boldsymbol{r})$ in the RUC by the notion of periodicity,

$$\boldsymbol{r} - \boldsymbol{r}_{\text{RUC}} = \sum_{\alpha=1}^{d} n_\alpha \boldsymbol{e}_\alpha \tag{4.3}$$

with integers $\{n_1, \ldots, n_d\}$.

When considering linear elastic lattices, we assume no material-inherent losses so that the attenuation constant vanishes. That is, waves travel without decay, implying $\boldsymbol{k} = i\boldsymbol{k}^{\text{Im}}$. Hence, the displacement field at any point in the lattice is described by the RUC via

$$\boldsymbol{u}_m(\boldsymbol{r}, t) = \boldsymbol{U}_m\big(\boldsymbol{r}_{\text{RUC}}(\boldsymbol{r})\big) \exp\left[i\left(\boldsymbol{k}^{\text{Im}} \cdot \sum_{\alpha=1}^{d} n_\alpha \boldsymbol{e}_\alpha - \omega t\right)\right]. \tag{4.4}$$

as illustrated in Fig. 4.1.

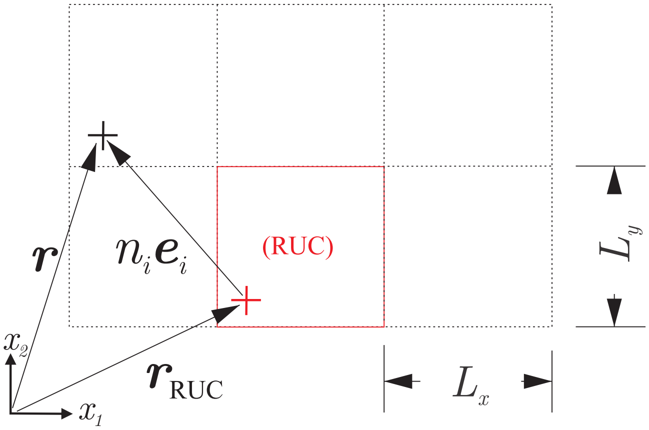

Figure 4.1: Linking wave motion in the entire lattice to the RUC

To predict wave motion, the above displacement field is inserted into the dynamic linear momentum balance equation,

$$\operatorname{div} \boldsymbol{\sigma} = \rho \ddot{\boldsymbol{u}}, \tag{4.5}$$

with infinitesimal stress tensor $\boldsymbol{\sigma}$ and acceleration $\ddot{\boldsymbol{u}}$ (dots denoting time derivatives); note that time-invariant body forces do not affect wave motion. Now, one solves for the dispersion relation between wave vector $\boldsymbol{k}$ and frequency ω. As described in Section 4.3, one solves for $\omega = \omega(\boldsymbol{k})$ numerically by prescribing wave vectors $\boldsymbol{k}$ and solving for the associated frequencies ω. By inspection of Eq. (4.2), one restricts the set of wave vectors to be investigated to within the *first Brillouin zone* (FBZ). That is, one chooses $\boldsymbol{k}$ such that

$$\boldsymbol{k}^{\text{Im}} \cdot (n_1 \boldsymbol{e}_1 + n_2 \boldsymbol{e}_2) \in (-\pi, \pi) \tag{4.6}$$

In reciprocal lattice space (with reciprocal lattice vectors $\{\boldsymbol{e}_1^*, \ldots, \boldsymbol{e}_d^*\}$), this corresponds to the Wigner-Seitz unit cell obtained as the convex domain delimited by Voronoi tessellation in the reciprocal lattice; see Fig. 4.5 for three example RUCs and associated FBZs to be discussed later.

Specifically, in 2D the FBZ is defined in reciprocal space by the set of wave vectors $\boldsymbol{k}^{\mathrm{Im}}$ bounded by

$$\boldsymbol{\zeta}(\alpha,\beta)\boldsymbol{k}^{\mathrm{Im}} \leq \pi \qquad \text{where} \qquad \boldsymbol{\zeta}(n_1,n_2) = \frac{2(n_1\boldsymbol{e}_1^* + n_2\boldsymbol{e}_2^*)}{||(n_1\boldsymbol{e}_1^* + n_2\boldsymbol{e}_2^*)||^2} \tag{4.7}$$

where the wave vectors are calculated as

$$\boldsymbol{e}_1^* = \frac{-\boldsymbol{R}\boldsymbol{e}_2}{\boldsymbol{e}_1 \cdot \boldsymbol{R}\boldsymbol{e}_2}\ , \quad \boldsymbol{e}_2^* = \frac{\boldsymbol{R}\boldsymbol{e}_1}{\boldsymbol{e}_2 \cdot \boldsymbol{R}\boldsymbol{e}_1}, \quad \boldsymbol{R} = \begin{bmatrix} 0 & -1 \\ 1 & 0 \end{bmatrix} \tag{4.8}$$

and (α,β) denotes all permutations $\{\alpha,\beta\} \in \{-1,0,1\}$.

From the dispersion relations, one obtains the *phase velocity* (which indicates how fast the wave travels in a direction $\boldsymbol{k}$):

$$\boldsymbol{v}_{\mathrm{p}}(\boldsymbol{k}) = \left(\frac{\omega(\boldsymbol{k})}{k_1^{\mathrm{Im}}}, \frac{\omega(\boldsymbol{k})}{k_2^{\mathrm{Im}}}\right)^{\mathrm{T}}. \tag{4.9}$$

Physically, this represents the velocity of the peak or trough of a single-frequency signal. By contrast, the *group velocity*

$$\boldsymbol{v}_{\mathrm{g}}(\boldsymbol{k}) = \left(\frac{\partial\omega(\boldsymbol{k})}{\partial k_1^{\mathrm{Im}}}, \frac{\partial\omega(\boldsymbol{k})}{\partial k_2^{\mathrm{Im}}}\right)^{\mathrm{T}} \tag{4.10}$$

indicates the direction and speed of the wave packet (i.e., this is the speed and direction of the propagating mechanical information). The direction of the group velocity equals the direction of energy flow (Langley, 1994), so that one associates wave beaming primarily with the group velocity. Admittedly this definition is not necessarily unique and experimental realizations often use alternative (measurable) metrics such as, e.g. maximum displacement or velocity amplitudes (Langley, 1997a; Jeong and Ruzzene, 2005). It is shown that both metrics produce qualitatively equivalent results by comparing beaming predictions (obtained from directional group velocity analysis to time-resolved wave propagation obtained via transient numerical calculations. For convenience a normalized group velocity is defined as

$$\bar{v}_{\mathrm{g}} = \frac{||\boldsymbol{v}_{\mathrm{g}}||}{c}, \qquad \text{with} \qquad c = \sqrt{\frac{E}{\rho}} \tag{4.11}$$

the bar sound speed of the base material having Young's modulus E and mass density ρ.

By exploiting the symmetry of the FBZ, one further reduces the set of wave vectors to be analyzed to the *irreducible Brillouin zone* (IBZ). To recover the full lattice response, results are mapped from the IBZ to the FBZ by exploiting in particular that

$$\boldsymbol{v}_{\mathrm{g}} = \begin{cases} \boldsymbol{v}_{\mathrm{g}} - 2(\boldsymbol{v}_{\mathrm{g}} \cdot \boldsymbol{m})\boldsymbol{m} & \text{for reflectional symmetry,} \\ -\boldsymbol{v}_{\mathrm{g}} & \text{for two-fold rotational symmetry,} \end{cases} \tag{4.12}$$

where $\boldsymbol{m}$ is a unit normal to any line of symmetry.

Based on the above definitions, a distinction is made for a given excitation frequency between

- *pass-bands* (a group velocity exists in all directions; i.e., waves propagate in all directions)
- *directional stop-bands* (a group velocity exists in only some directions; i.e., waves only propagate in certain directions)
- *complete stop-bands* (no group velocity exists for the chosen frequency in any direction; i.e., waves do not propagate in any direction).

4.3 Numerical implementation

4.3.1 Eigenvalue Problem

Lattice mechanics are described via linear elastic beam theory for infinitesimal displacements and rotations in an FE-discretized setting[1]. Although planar lattices are studies, wave motion involves 3D deformation and obeys the discretized governing equation

$$\boldsymbol{M}\ddot{\boldsymbol{U}} + \boldsymbol{K}\boldsymbol{U} = \boldsymbol{F} \tag{4.13}$$

with global consistent mass matrix $\boldsymbol{M}$ and stiffness matrix $\boldsymbol{K}$, and global displacement and external force vectors $\boldsymbol{U}$ and $\boldsymbol{F}$, respectively. Assuming time-harmonic displacements

$$\boldsymbol{U}(t) = \hat{\boldsymbol{U}} \exp(i\omega t) \tag{4.14}$$

---

[1] For exclusively this chapter, Abaqus simulations use B32 elements with quadratic interpolation. Meshes are shown in 4.5.1

and forces

$$\boldsymbol{F}(t) = \hat{\boldsymbol{F}}\ \exp(i\omega t), \tag{4.15}$$

one arrives at

$$(\boldsymbol{K} - \omega^2\boldsymbol{M})\hat{\boldsymbol{U}} = \hat{\boldsymbol{F}} \tag{4.16}$$

For application in software or libraries with only real valued matrices and methods, the complex-valued problem is separated into real and imaginary parts following Aberg (1997), i.e.,

$$(\boldsymbol{K} - \omega^2\boldsymbol{M})\hat{\boldsymbol{U}}^{\mathrm{Re}} = \hat{\boldsymbol{F}}^{\mathrm{Re}}, \qquad (\boldsymbol{K} - \omega^2\boldsymbol{M})\hat{\boldsymbol{U}}^{\mathrm{Im}} = \hat{\boldsymbol{F}}^{\mathrm{Im}}. \tag{4.17}$$

To separate displacements of internal nodes $\boldsymbol{U}_{\mathrm{i}}$, master boundary nodes $\boldsymbol{U}_{\mathrm{m}}$, and slave boundary nodes $\boldsymbol{U}_{\mathrm{s}}$, we introduce a permutation matrix $\boldsymbol{A}$ (with $\boldsymbol{A}^{\mathrm{T}}\boldsymbol{A} = \boldsymbol{I}$) and boundary condition matrix $\boldsymbol{Q}$ such that

$$\boldsymbol{A}\boldsymbol{U} = \begin{bmatrix} \boldsymbol{U}_{\mathrm{i}} \\ \boldsymbol{U}_{\mathrm{m}} \\ \boldsymbol{U}_{\mathrm{s}} \end{bmatrix} \qquad \text{and} \qquad \begin{bmatrix} \boldsymbol{U}_{\mathrm{i}}^{\mathrm{Re}} \\ \boldsymbol{U}_{\mathrm{m}}^{\mathrm{Re}} \\ \boldsymbol{U}_{\mathrm{s}}^{\mathrm{Re}} \\ \boldsymbol{U}_{\mathrm{i}}^{\mathrm{Im}} \\ \boldsymbol{U}_{\mathrm{m}}^{\mathrm{Im}} \\ \boldsymbol{U}_{\mathrm{s}}^{\mathrm{Im}} \end{bmatrix} = \boldsymbol{Q}(\boldsymbol{k}) \begin{bmatrix} \boldsymbol{U}_{\mathrm{i}}^{\mathrm{Re}} \\ \boldsymbol{U}_{\mathrm{m}}^{\mathrm{Re}} \\ \boldsymbol{U}_{\mathrm{i}}^{\mathrm{Im}} \\ \boldsymbol{U}_{\mathrm{m}}^{\mathrm{Im}} \end{bmatrix}. \tag{4.18}$$

$\boldsymbol{Q}$ depends on wave vector $\boldsymbol{k}$ and relates the displacements of master and slave boundary nodes according to the Bloch wave assumption (4.2) and illustrated in Fig. 4.2.

Analogously, we obtain the vector of internal and external forces by application of $\boldsymbol{Q}^{\mathrm{T}}$, so that we overall arrive at

$$\boldsymbol{Q}^{\mathrm{T}}(\boldsymbol{k})\left(\begin{bmatrix} \boldsymbol{K} & \boldsymbol{0} \\ \boldsymbol{0} & \boldsymbol{K} \end{bmatrix} - \omega^2 \begin{bmatrix} \boldsymbol{M} & \boldsymbol{0} \\ \boldsymbol{0} & \boldsymbol{M} \end{bmatrix}\right) \begin{bmatrix} \boldsymbol{A}^{\mathrm{T}} & \boldsymbol{0} \\ \boldsymbol{0} & \boldsymbol{A}^{\mathrm{T}} \end{bmatrix} \boldsymbol{Q}(\boldsymbol{k}) \begin{bmatrix} \hat{\boldsymbol{U}}_{\mathrm{i}}^{\mathrm{Re}} \\ \hat{\boldsymbol{U}}_{\mathrm{m}}^{\mathrm{Re}} \\ \hat{\boldsymbol{U}}_{\mathrm{i}}^{\mathrm{Im}} \\ \hat{\boldsymbol{U}}_{\mathrm{m}}^{\mathrm{Im}} \end{bmatrix} = \begin{bmatrix} \hat{\boldsymbol{F}}_{\mathrm{i}}^{\mathrm{Re}} \\ \hat{\boldsymbol{F}}_{\mathrm{m}}^{\mathrm{Re}} \\ \hat{\boldsymbol{F}}_{\mathrm{i}}^{\mathrm{Im}} \\ \hat{\boldsymbol{F}}_{\mathrm{m}}^{\mathrm{Im}} \end{bmatrix}. \tag{4.19}$$

For wave propagation starting from the undeformed ground state the right-hand side vanishes therefore providing the form

$$\boldsymbol{Q}^{\mathrm{T}}(\boldsymbol{k})\left(\begin{bmatrix} \boldsymbol{K} & \boldsymbol{0} \\ \boldsymbol{0} & \boldsymbol{K} \end{bmatrix} - \omega^2 \begin{bmatrix} \boldsymbol{M} & \boldsymbol{0} \\ \boldsymbol{0} & \boldsymbol{M} \end{bmatrix}\right) \begin{bmatrix} \boldsymbol{A}^{\mathrm{T}} & \boldsymbol{0} \\ \boldsymbol{0} & \boldsymbol{A}^{\mathrm{T}} \end{bmatrix} \boldsymbol{Q}(\boldsymbol{k}) \begin{bmatrix} \hat{\boldsymbol{U}}_{\mathrm{i}}^{\mathrm{Re}} \\ \hat{\boldsymbol{U}}_{\mathrm{m}}^{\mathrm{Re}} \\ \hat{\boldsymbol{U}}_{\mathrm{i}}^{\mathrm{Im}} \\ \hat{\boldsymbol{U}}_{\mathrm{m}}^{\mathrm{Im}} \end{bmatrix} = \boldsymbol{0} \tag{4.20}$$

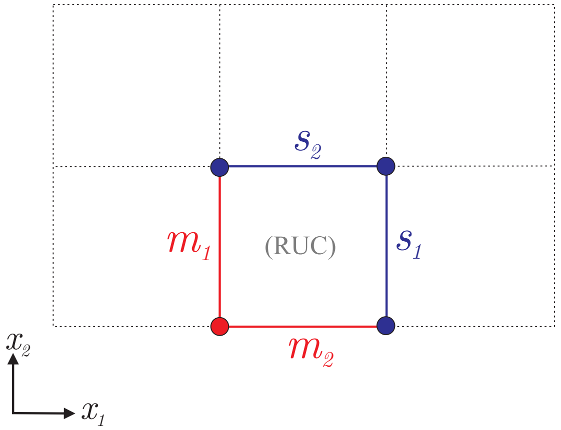

Figure 4.2: Master and slave boundary conditions on RUC

that the real and imaginary systems of equations are coupled through $\boldsymbol{Q}$, which is enforced numerically by introducing kinematic constraints between the two eigenvalue problems to be solved simultaneously for the finite set of frequencies $\omega(\boldsymbol{k}^{\mathrm{Im}})$ (one per degree of freedom in the discrete representation of the IBZ). Depending on the eigenvalue extraction method, all or a subset can be calculated. Here, the lowest few eigenfrequencies will be of relevance, for reference Abaqus' multi-level substructuring (AMS) eigensolver (due to increased performance compared to the Lanczos method) was used to identify the frequencies of interest.

For ease of comparison, all examples will report the normalized frequency and wave vector, respectively,

$$\bar{f} = \frac{\omega L}{2\pi c}, \qquad \bar{\boldsymbol{k}} = L\boldsymbol{k}^{\mathrm{Im}}, \tag{4.21}$$

where L is a characteristic length of the unit cell, c the wave speed.

4.3.2 Mode identification

During vibrational wave motion, lattice members in 2D lattices undergo longitudinal and flexural motion both within and out of the plane spanned by the lattice, leading to the manifestation of in-plane and out-of-plane wave modes.

To differentiate between those macroscopic vibrational modes in the dispersion relations, one categorizes mode shapes as *in-plane* vs. *out-of-plane* as follows. Starting with an eigenvector $\hat{\boldsymbol{U}}$ (defined up to a constant), we apply mass normalization, i.e.,

$$\Phi = \hat{\boldsymbol{U}} / \hat{\boldsymbol{U}} \cdot \boldsymbol{M}\hat{\boldsymbol{U}} \tag{4.22}$$

and further introduce projection matrices $\boldsymbol{P}_1$, $\boldsymbol{P}_2$ and $\boldsymbol{P}_3$ such that

$$\boldsymbol{\phi}_i = \boldsymbol{P}_i \Phi \tag{4.23}$$

contains only the displacement components in the x_i-coordinate direction. The coordinate system is chosen such that the lattice lies in the (x_1, x_2)-plane, while x_3 is perpendicular to the lattice plane. Based on the above, we define mass-weighted directional contributions p_i related to the associated kinetic energy via (no summation convention implied)

$$p_i = \boldsymbol{\phi}_i \cdot \boldsymbol{M} \boldsymbol{\phi}_i. \tag{4.24}$$

To differentiate between in-plane and out-of-plane modes, we calculate a scalar *in-plane ratio*

$$\beta = \frac{\sqrt{p_1^2 + p_2^2}}{\sqrt{p_1^2 + p_2^2 + p_3^2}}, \qquad \Rightarrow \qquad \beta \approx \begin{cases} 1 & \text{for in-plane modes,} \\ 0 & \text{for out-of-plane modes.} \end{cases} \tag{4.25}$$

and $0 \leq \beta \leq 1$.

4.3.3 Explicit Dynamic Analysis

Directional wave beaming has been predicted or verified in the literature by two types of simulations: modal techniques (Langley, 1997a; Ruzzene, Mazzarella, et al., 2002; Ruzzene, Scarpa, and Soranna, 2003) and direct time integration (Casadei and Rimoli, 2013). In order to validate predictions in subsequent sections – while avoiding further approximations or assumptions introduced by modal analysis and necessary boundary conditions – example studies by direct numerical simulations using explicit central-difference time integration (for efficiency, lumped mass matrices are used for transient calculations) are provided. Analysis was performed without material damping nor FE truncation frequency damping, so that only traces of numerical damping from the finite difference scheme may be expected. To excite wave motion, displacements instead of forces are imposed to reduce numerical artifacts, see 4.6. Time-harmonic out-of-plane displacements are imposed at the center-most node of the simulated lattice according to

$$u_3(t) = \hat{u} \sin(2\pi f t) \tag{4.26}$$

with frequency f and (arbitrary) amplitude $\hat{u}$. Explicit time stepping uses sufficiently small time steps for stability and is terminated before the wave arrives at any lattice boundary.

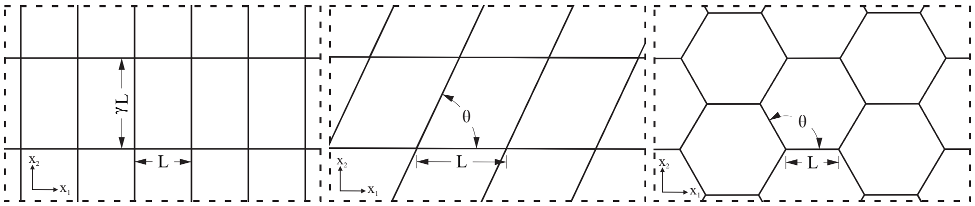

(a) Rectangular lattice (b) Sheared lattice (c) Hexagonal lattice

Figure 4.3: Three example lattices studied in the following with characteristic beam length L and (a) stretch ratio γ, (b) shear angle θ, and (c) honeycomb vs. re-entrant control angle θ.

4.4 Example lattices architectures

The phenomena associated with wave beaming by the help of three example lattice architectures defined by the rectangular, sheared, and hexagonal RUCs depicted in Fig. 4.3 is demonstrated and explained. Each lattice type was chosen to study the impact of fundamental geometric features on wave propagation. First, rectangular lattices highlight the effect of unit cell aspect ratio γ, furthering the understanding of the vibration of beam grillages (Heckl, 1964; Langley, 1996; Langley, 1997a; Langley, 1997b). Second, the effect of asymmetry in a sheared square lattice (parametrized by the shear angle θ while fixing all beam lengths) is studied. Third, focus is placed on the transition from regular hexagonal to re-entrant unit cells (characterized by the internal angle θ). This scenario was extensively studied before (Ruzzene, Mazzarella, et al., 2002; Phani et al., 2006; Gonella and Ruzzene, 2008b; Gonella and Ruzzene, 2008a). While varying the aforementioned geometric parameters, we maintain a constant cross-section of all beams in the lattice.

For consistency, all lattice members have a constant, circular cross-section described by the slenderness ratio $\lambda = L/D$ where D is the diameter of the circular cross-section ($\lambda = 10$ in numerical examples).

The three lattice architectures are described by the RUCs of Fig. 4.4 with lattice vectors $\boldsymbol{e}_i$ detailed in Table 4.1 along with the reciprocal lattice vectors. We reduce the wave vector domain to the IBZ by observing the geometric symmetries (two-fold reflectional symmetry for rectangular and hexagonal lattices, and a rotational symmetry for the sheared lattice), which results in the IBZs of Fig. 4.5.

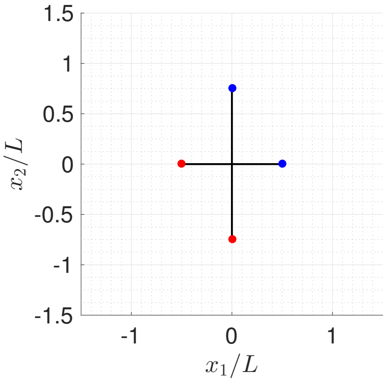

(a) Rectangular unit cell with aspect ratio γ = 1.5.

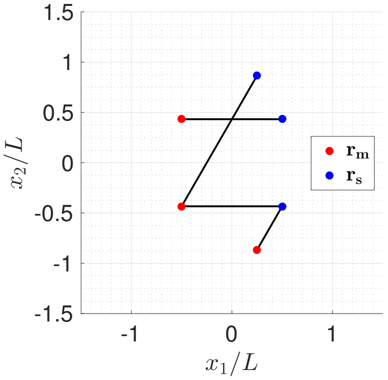

(b) Sheared unit cell with shear angle θ = 60°.

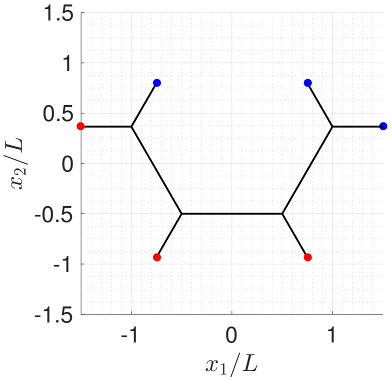

(c) Hexagonal unit cell with interior angle θ = 120°.

Figure 4.4: Example RUCs including master ($\boldsymbol{r}_\mathrm{m}$) and slave ($\boldsymbol{r}_\mathrm{s}$) nodes of the boundary (all lengths normalized by L).

Table 4.1: Lattice architectures studied in the following along with physical and reciprocal lattice base vectors with $(\boldsymbol{x}_1, \boldsymbol{x}_2)$ denoting the Cartesian unit vectors in the lattice plane.

RUC	Physical lattice	Reciprocal lattice	Configurations analyzed
Rectangular	$\boldsymbol{e}_1 = L\boldsymbol{x}_1$ $\boldsymbol{e}_2 = \gamma L\boldsymbol{x}_2$	$\boldsymbol{e}_1^* = \frac{1}{L\gamma}\boldsymbol{x}_2$ $\boldsymbol{e}_2^* = \frac{1}{L}\boldsymbol{x}_1$	$\gamma \in \{1.00, 1.25, 1.50,$ $1.75, 2.00\}$
Sheared	$\boldsymbol{e}_1 = L\boldsymbol{x}_1$ $\boldsymbol{e}_2 = 2L\sin\theta\boldsymbol{x}_2$	$\boldsymbol{e}_1^* = \frac{1}{2L\sin\theta}\boldsymbol{x}_2$ $\boldsymbol{e}_2^* = \frac{1}{L}\boldsymbol{x}_1$	$\theta \in \{30°, 45°, 60°, 90°\}$
Hexagonal	$\boldsymbol{e}_1 = 2L(1-\cos\theta)\boldsymbol{x}_1$ $\boldsymbol{e}_2 = 2L\sin\theta\boldsymbol{x}_2$	$\boldsymbol{e}_1^* = \frac{1}{2L\sin\theta}\boldsymbol{x}_2$ $\boldsymbol{e}_2^* = \frac{1}{2L(1-\cos\theta)}\boldsymbol{x}_1$	$\theta \in \{60°, 70°, 80°, 90°,$ $100°, 110°, 120°\}$

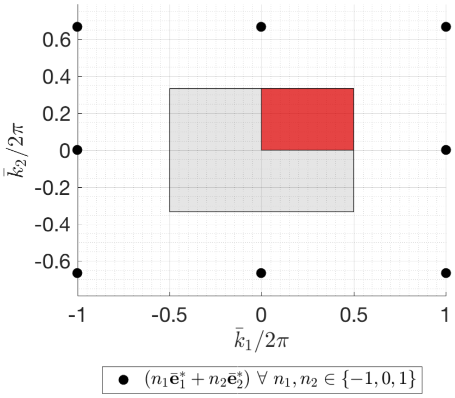

(a) Rectangular unit cell with aspect ratio $\gamma = 1.5$.

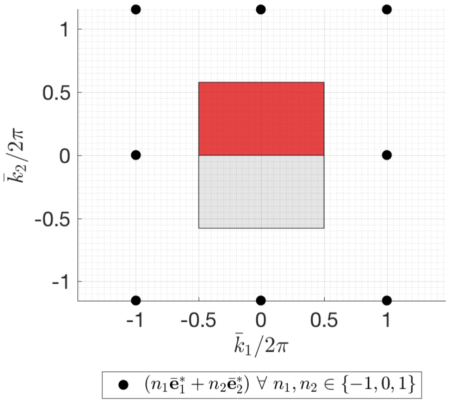

(b) Sheared unit cell with shear angle $\theta = 60°$.

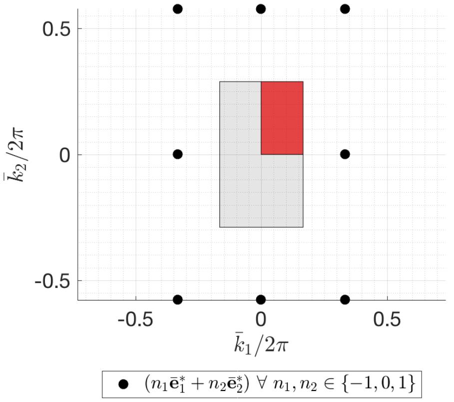

(c) Hexagonal unit cell with interior angle $\theta = 120°$.

Figure 4.5: Wave vector parametrization showing FBZ and IBZ in reciprocal space (the RUC is centered at the origin). Black dots indicate centers of neighboring unit cells, gray and red regions jointly make up the FBZ, red regions indicate the IBZs.

4.4.1 Mode identification and group velocity determination

To determine vibrational energy flow for a given lattice, one first identifies in-plane and out-of-plane vibrational modes by the three directional contributions p_i, as shown in Fig. 4.6a for a rectangular lattice ($\gamma = 1.5$). Color-coding the lowest few dispersion surfaces by the in-plane ratio β of Eq. (4.25) reveals in-plane and out-of-plane modes as shown in Fig. 4.6b. For clarity, the first three in-plane and out-of-plane surfaces are shown in Figs. 4.6c through 4.6h. In the following only the first two out-of-plane dispersion surfaces, shown in Fig. 4.6i, will be focused on. For confirmation of in-plane and out-of-plane modes, Fig. 4.7 illustrates the lowest four mode shapes for $\boldsymbol{k} = (\pi, 0)^{\mathrm{T}}$ along with their respective β-values.

In order to predict directional wave propagation for a given lattice architecture, one analyzes the group velocity (as a metric of vibrational energy flow) associated with all directions and excitation frequencies of interest. The group velocity is defined by the gradient of the dispersion surfaces, and this causes a methodological dilemma. Ideally, one would determine whether or not for a particular direction group velocities exist over a range of frequencies. However, practical limitations force as to compute the dispersion relations directly and extract the group velocities from the latter (thus, one is unable to control the group velocity direction, it is merely an outcome of dispersion surface calculations). Moreover, proving the (non)existence of a finite group velocity in a particular direction requires computing the group velocity at each and every point on the dispersion surfaces of interest. However, the dispersion relation is computed numerically by sampling in $\boldsymbol{k}$-space. Thus, the computation of the gradient not only introduces numerical errors but is also limited by the sampling resolution (high resolutions of points in $\boldsymbol{k}$-space implying high computational costs).

A traditional way to evaluate the direction of the gradient is the use of iso-frequency contour plots of the dispersion surfaces (Langley, 1997a), see, e.g. Figs. 4.8a and 4.8b which represent the lowest two surfaces of a hexagonal lattice with $\theta = 120°$. The group velocity direction is hence perpendicular to the iso-frequency contours, and its magnitude is related to the proximity of two consecutive lines. Even though they are easily obtained, such plots do not precisely reveal group velocity direction and magnitude.

Fitting continuous functions to the iso-frequency contours (Ruzzene, Scarpa, and Soranna, 2003) in Figs. 4.8a and 4.8b allows one to analytically calculate the group velocity direction by differentiation, which results in Figs. 4.9a and 4.9b. Note that these plots are no longer in $\boldsymbol{k}$-space but show the group velocity direction (from $0-90°$ in the IBZ) as a function of frequency. This clearly elucidates the directions of unattenuated wave propagation. However, results in Fig. 4.9 crucially depend on the discrete choice of iso-frequency contours. Furthermore, one can observe an obvious overlap in frequency bands between the first and second surfaces. Hence, except at very low frequencies, it is not suitable to only consider individual surfaces (Langley, 1997a). Instead, this work will consider all out-of-plane surfaces existing in a frequency band of interest.

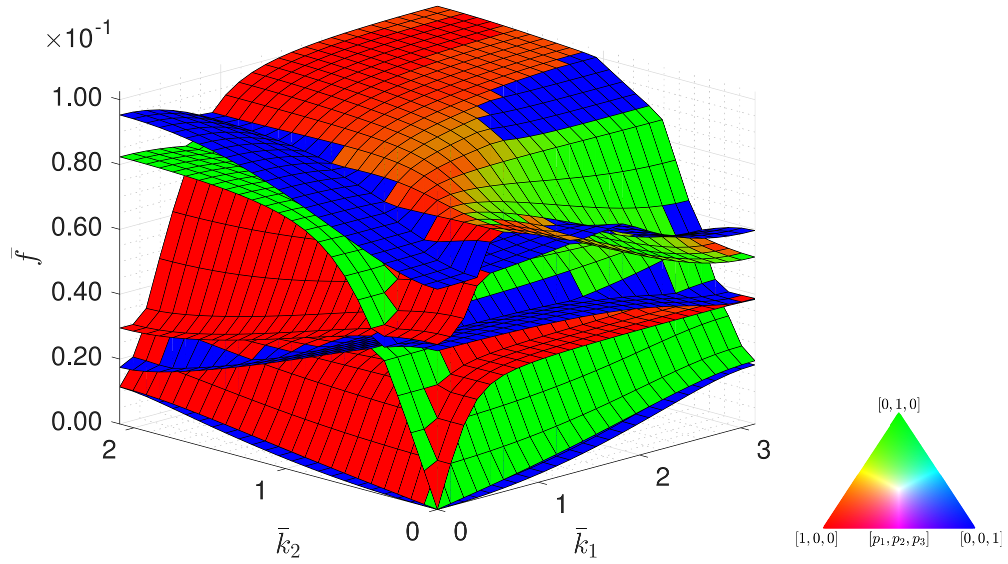

(a) Lowest few dispersion surfaces generated by Bloch wave analysis, colored by the directional contributions p_i.

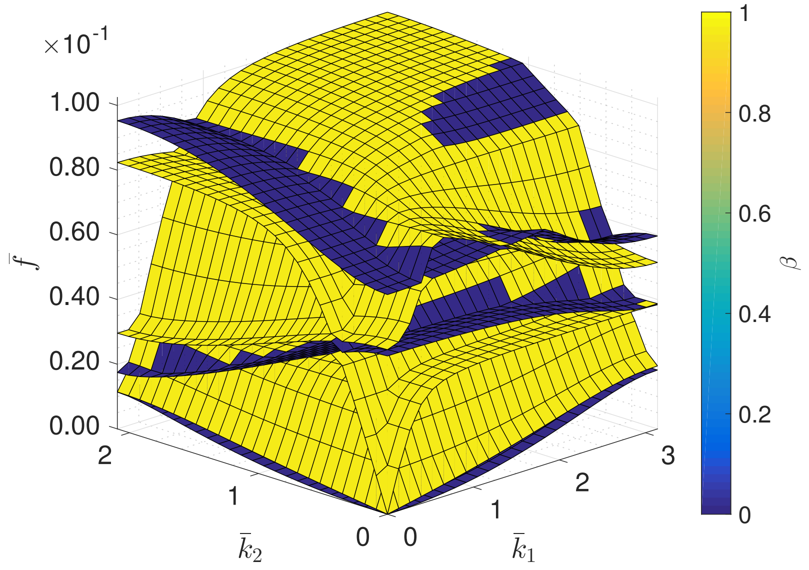

(b) The same dispersion surfaces colored by in-plane ratio β.

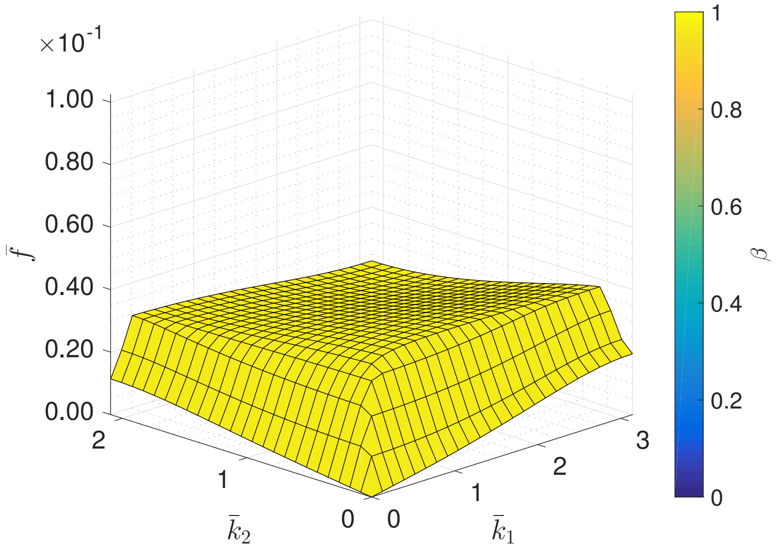

(c) Lowest frequency in-plane surface.

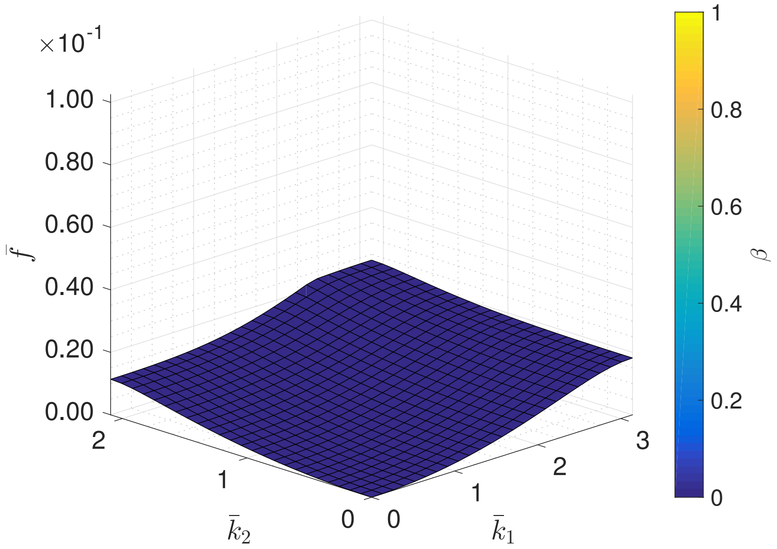

(d) Lowest frequency in-plane surface.

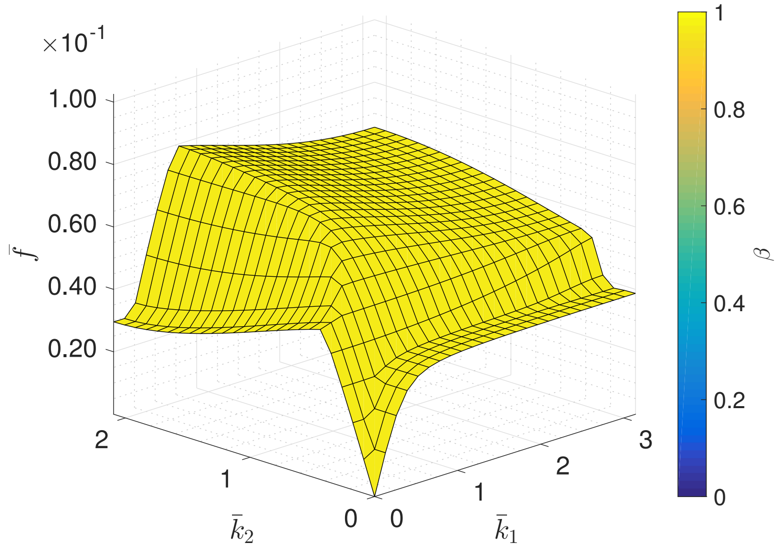

(e) Second lowest frequency out-of-plane surface.

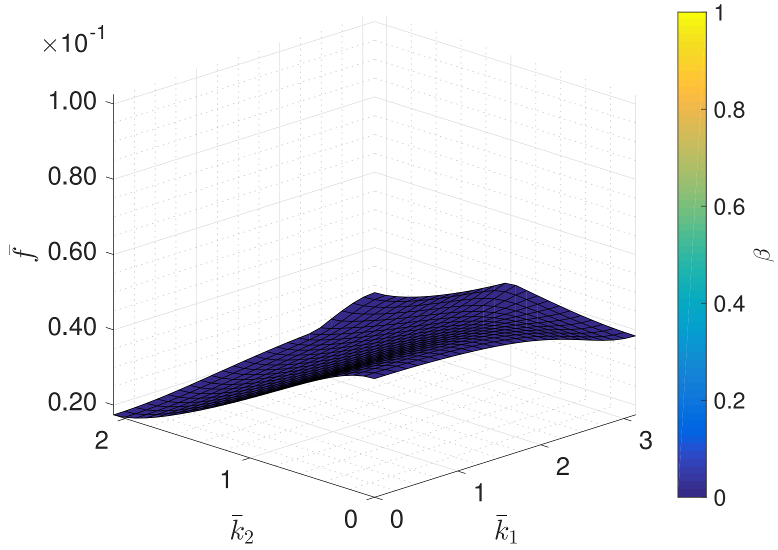

(f) Second lowest frequency in-plane surface.

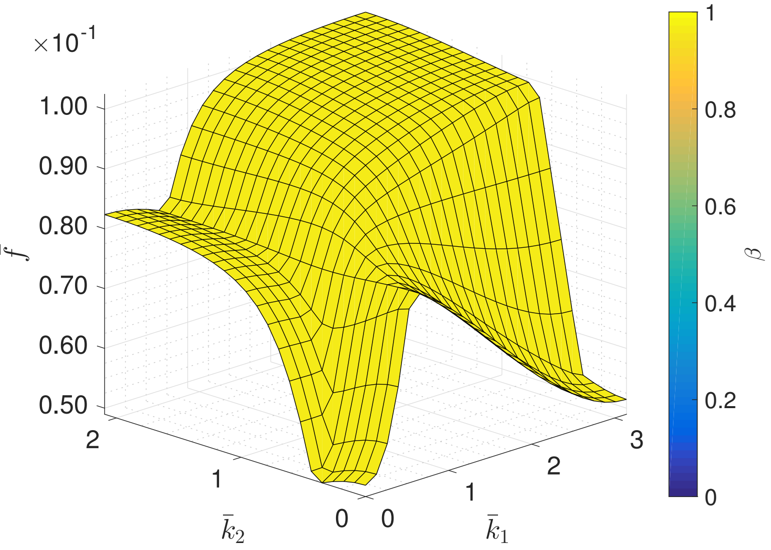

(g) Third lowest frequency in-plane surface.

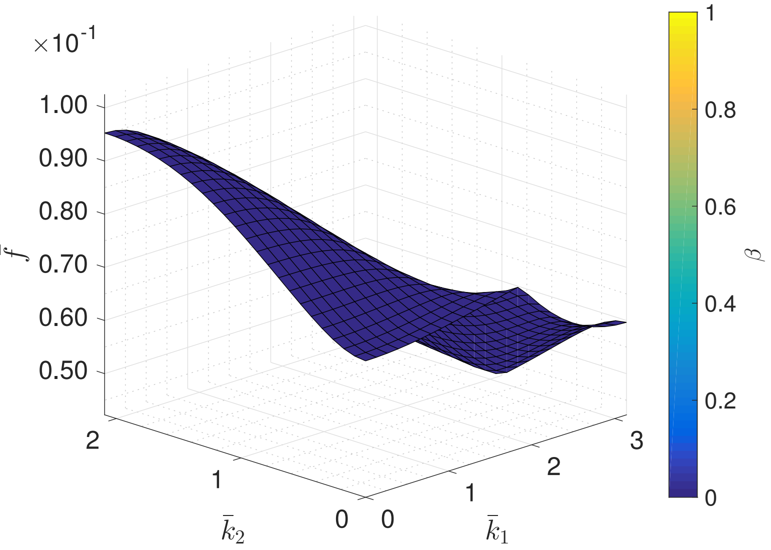

(h) Third lowest frequency in-plane surface.

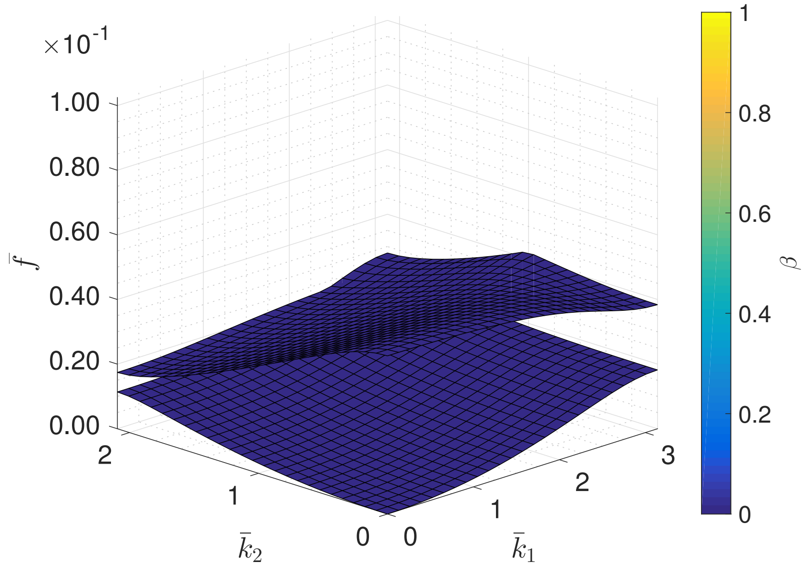

(i) Two lowest-frequency out-of-plane dispersion surfaces.

Figure 4.6: Dispersion surfaces and mode identification for the rectangular lattice (shown for $\gamma = 1.5$, all lengths normalized by L).

Fig. 4.10 introduces our improved methodology to analyze directional group velocity distributions. For these (and all other) examples, the dispersion relation is calculated on an equally-spaced reciprocal grid of 25×25 points within the IBZ in $\boldsymbol{k}$-space. Subsequently, dispersion surfaces are interpolated via cubic splines (rather than interpolating iso-frequency lines) whose differentiation results in the group velocity now available continuously at every point in $\boldsymbol{k}$-space. This results in continuous maps of the group velocity magnitude as shown in Fig. 4.10 for the lowest two out-of-plane surfaces. Directional or complete stop-bands, if any, appear in these plots as white space.

Fig. 4.11a shows the superposition of the lowest two out-of-plane surfaces of Fig. 4.10, thus providing a complete picture of the group velocity in the frequency range $\bar{f} = 0 - 1.20 \cdot 10^{-2}$. By exploiting the aforementioned symmetries, one can reconstruct the full 360° group velocity distribution shown in Fig. 4.11b. Results confirm the six-fold symmetry that may be expected for the hexagonal lattice. Although no significant stop-bands appear, wave beaming appears most pronounced for frequencies near $\bar{f} = 1 - 1.2 \cdot 10^{-2}$. Notice that beaming would have been entirely missed (or even misinterpreted) if only the lowest out-of-plane had been considered. Also, beaming in this frequency range could not have been predicted merely by means of band gaps in the dispersion relations.

(a) Mode shape 1: $\bar{f} = 1.82 \times 10^{-2}$, $\beta = 0.000$

(b) Mode shape 2: $\bar{f} = 1.95 \times 10^{-2}$, $\beta = 0.999$

(c) Mode shape 3: $\bar{f} = 3.84 \times 10^{-2}$, $\beta = 0.000$

(d) Mode shape 4: $\bar{f} = 3.88 \times 10^{-2}$, $\beta = 0.999$

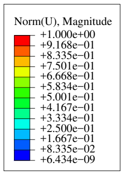

Figure 4.7: Mode shapes for the four lowest frequencies in order of increasing frequency at $\boldsymbol{k} = (\pi, 0)^{\mathrm{T}}$ for the rectangular lattice (shown are the real parts of the eigenvectors for $\gamma = 1.5$).

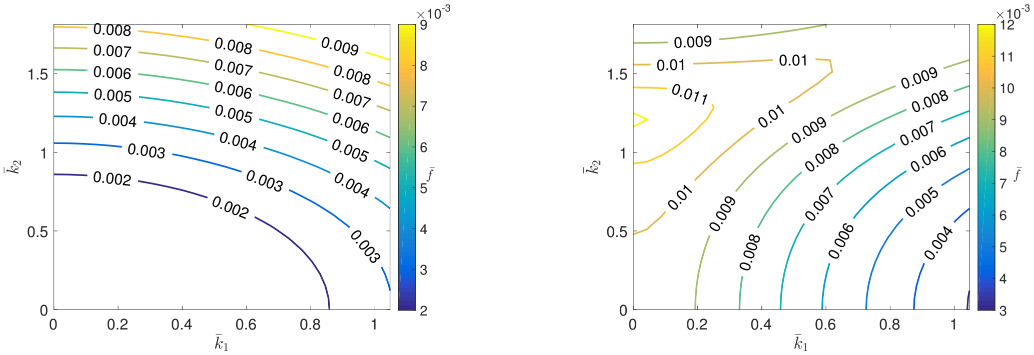

(a) First dispersion surface.

(b) Second dispersion surface.

Figure 4.8: Out-of-plane dispersion surfaces of the IBZ of a hexagonal lattice (with $\theta = 120°$) showing contour lines of constant frequency.

4.5 Results: controlling wave motion by lattice architecture

In the following, the validity of the above procedures to identify beaming and elucidate opportunities for directional propagation of out-of-plane wave motion in 2D lattices is demonstrated. To this end, the following strategy to examples of

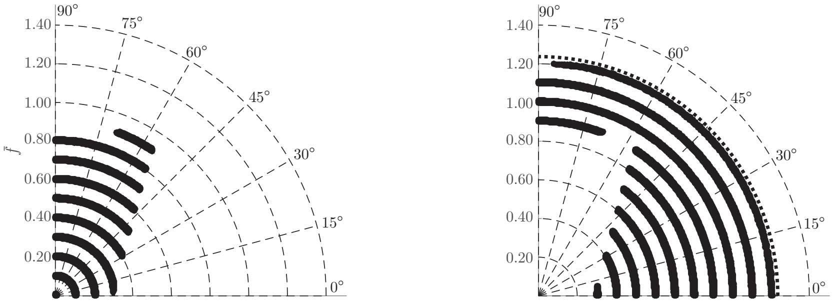

(a) First dispersion surface.

(b) Second dispersion surface.

Figure 4.9: Frequency-dependent group velocity directions in the IBZ calculated via differentiating splines fitted to the iso-frequency contour lines of the lowest two out-of-plane dispersion surfaces of Fig. 4.8.

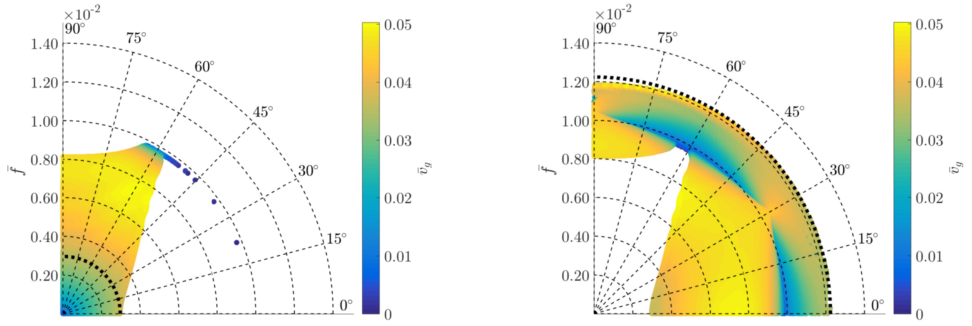

(a) First dispersion surface

(b) Second dispersion surface

Figure 4.10: Group velocity magnitude and direction in the IBZ of a hexagonal lattice ($\theta = 120°$). Dotted black lines indicate the minimum frequency of the next higher surface.

rectangular, sheared, and hexagonal lattices is applied:

- *Mode identification*: this work identifies in-plane vs. out-of-plane vibrational modes in the dispersion relation by using the definitions of Section 4.3.2.
- *Group velocity analysis*: the new group velocity visualization tools of Section 4.4.1 are applied to predict directionality as a function of the RUC geometry. All group velocity plots use the compact IBZ representation; full angular information can be obtained by symmetry. For reference, plots also include the natural frequencies of individual constituent beams with pinned-pinned

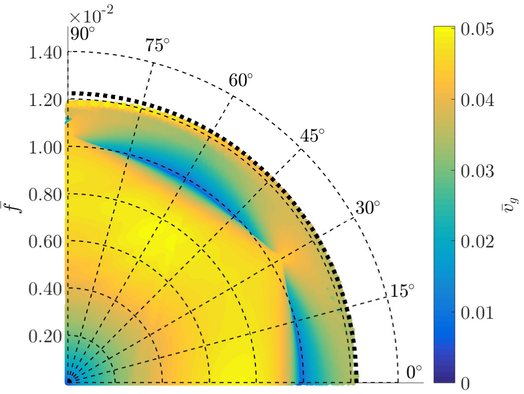

(a) Compact representation

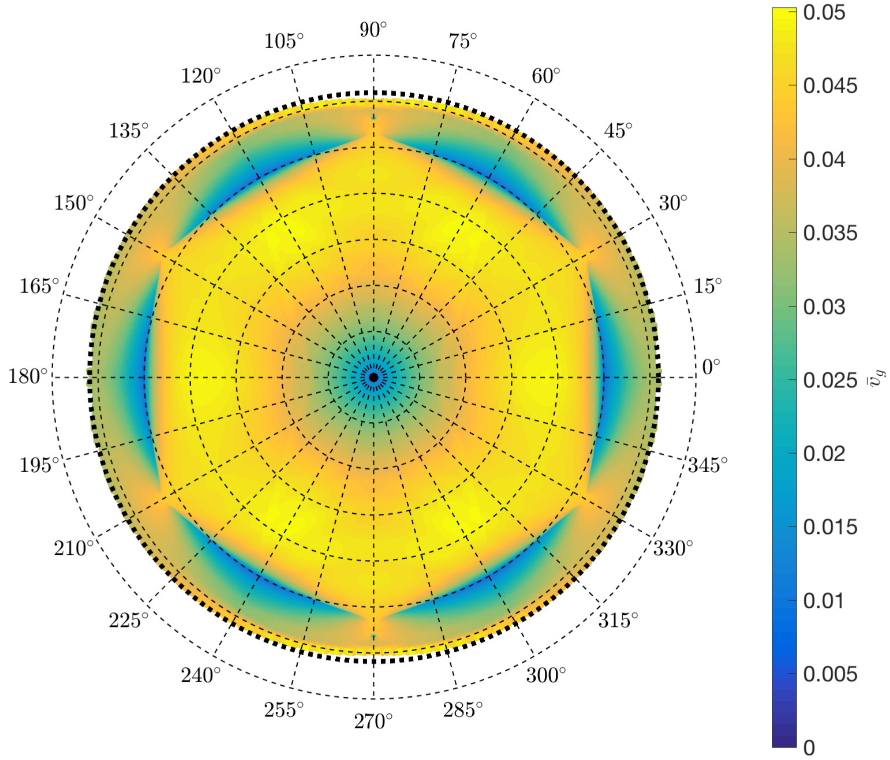

(b) Full representation

Figure 4.11: Group velocity magnitude and direction from the lowest two out-of-plane dispersion surfaces superimposed for a hexagonal lattice (θ = 120°). Dotted black lines indicate the minimum frequency of the third (not considered) surface.

and fixed-fixed boundary conditions, respectively:

$$f_{pp} = \frac{\pi^2}{2\pi l^2}\sqrt{\frac{EI}{\rho A}}, \qquad\qquad f_{ff} = \frac{22.4}{2\pi l^2}\sqrt{\frac{EI}{\rho A}}. \tag{4.27}$$

Note that this work include the lowest frequency of the next higher (not considered) dispersion surface as a dotted line in all plots to ensure that no higher surface can influence the results in the shown frequency ranges.

- *Transient simulations*: theoretical group velocity predictions are validated by comparison to transient simulation results, providing insight into the limitations of information extracted from dispersion relations.

4.5.1 Finite element meshes

Fig. 4.12 illustrates the discrete FE meshes (shown are the FE nodes) used to compute the dispersion relations for rectangular meshes with different aspect ratios. Similarly, Figs. 4.13 and 4.14 show the meshes used for sheared and hexagonal meshes, respectively. The total number of elements per length L for each mesh is approximately 30, 30, and 15 in rectangular, sheared, and hexagonal geometries, respectively.

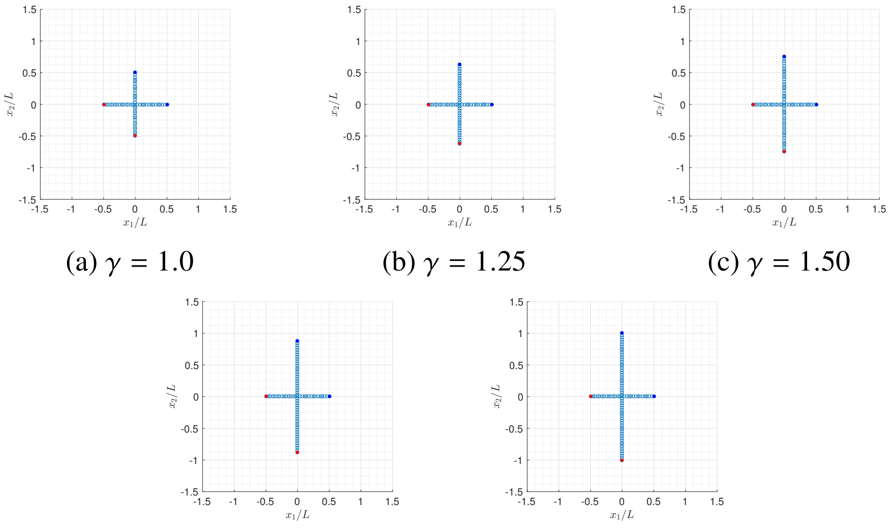

(a) $\gamma = 1.0$ (b) $\gamma = 1.25$ (c) $\gamma = 1.50$

(d) $\gamma = 1.75$ (e) $\gamma = 2.0$

Figure 4.12: FE discretizations of rectangular RUCs having different aspect ratios γ.

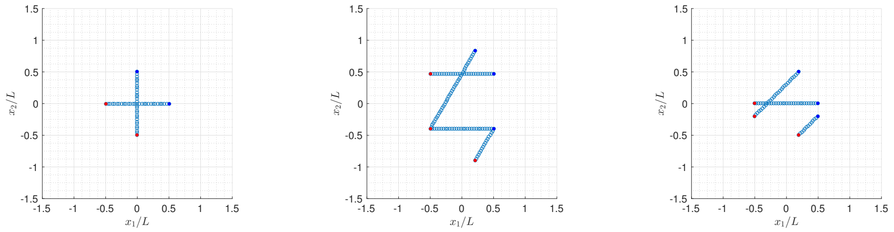

(a) θ = 90°

(b) θ = 60°

(c) θ = 45°

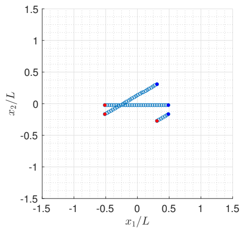

(d) θ = 30°

Figure 4.13: FE discretizations of sheared RUCs having different shear angels θ.

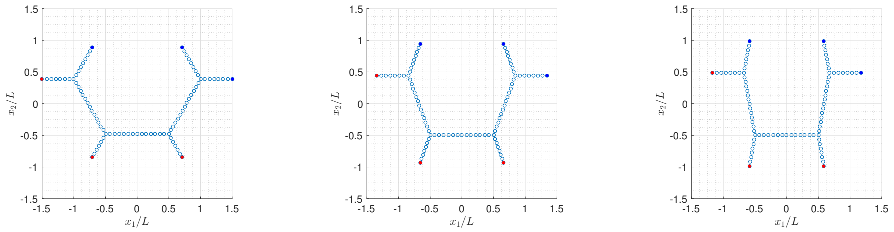

(a) θ = 120°

(b) θ = 110°

(c) θ = 100°

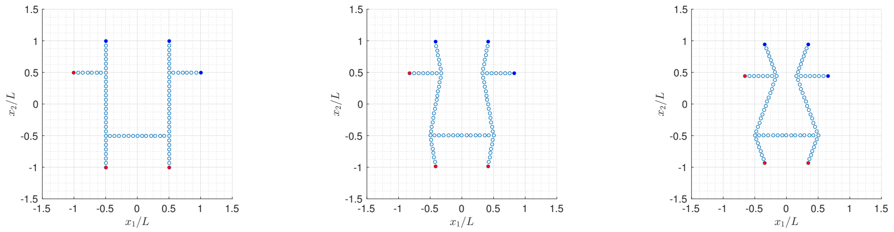

(d) θ = 90°

(e) θ = 80°

(f) θ = 70°

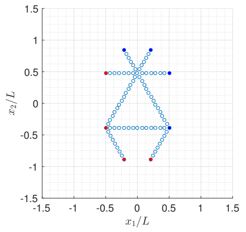

(g) θ = 60°

Figure 4.14: FE discretizations of hexagonal RUCs having different interior angels θ.

4.6 Impact of force vs. displacement excitation

Previously conducted transient analyses of wave motion have primarily used an externally applied force as opposed to a displacement boundary condition for lattice excitation. Fig. (4.15) shows the temporal and frequency responses at the two measurement points in the rectangular lattice ($\gamma = 1.5$) for the two different boundary conditions. As a primary difference between the two types of excitation, we observe that harmonic force excitation produces substantial low-frequency noise and a longer transient time period as compared to harmonic displacement excitation. This is an important observation and explains why displacements have been enforced here.

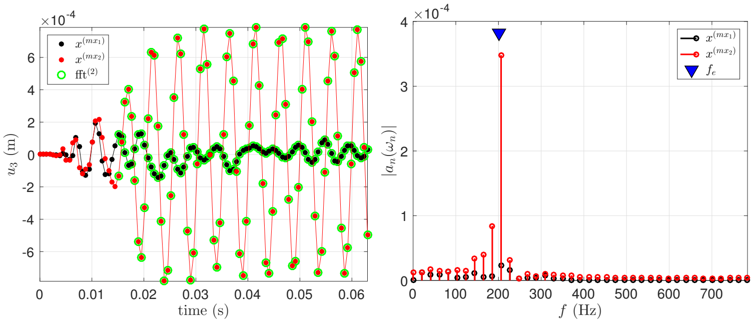

(a) Displacement excitation (b) FFT spectrum of (a)

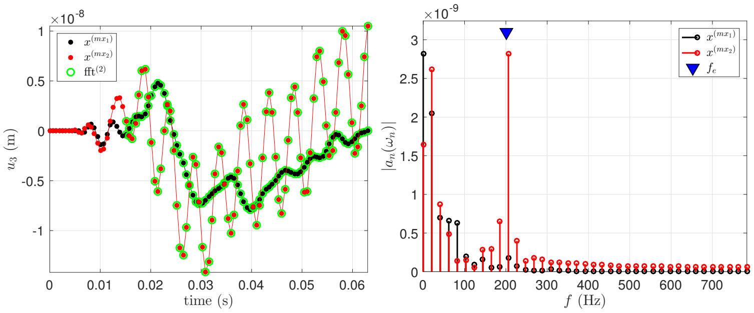

(c) Force excitation (d) FFT spectrum of (c)

Figure 4.15: Comparison of the transient dynamic lattice response to externally applied harmonic forces and displacements.

4.6.1 Rectangular lattice

This work first revisits the fundamental case of the rectangular lattice, which serves as an ideal example demonstrating partial stop-bands. Group velocity distributions are shown in Fig. 4.16, illustrating the effect of different RUC aspect ratios γ visualized in Fig. 4.16f. The first two out-of-plane dispersion surfaces are considered, and they clearly illustrate the effect of geometry on directional band gaps and beaming.

Stop-bands have been associated with local resonance. Thus, as expected from the resonance frequencies of individual beams, the lowest-frequency directional

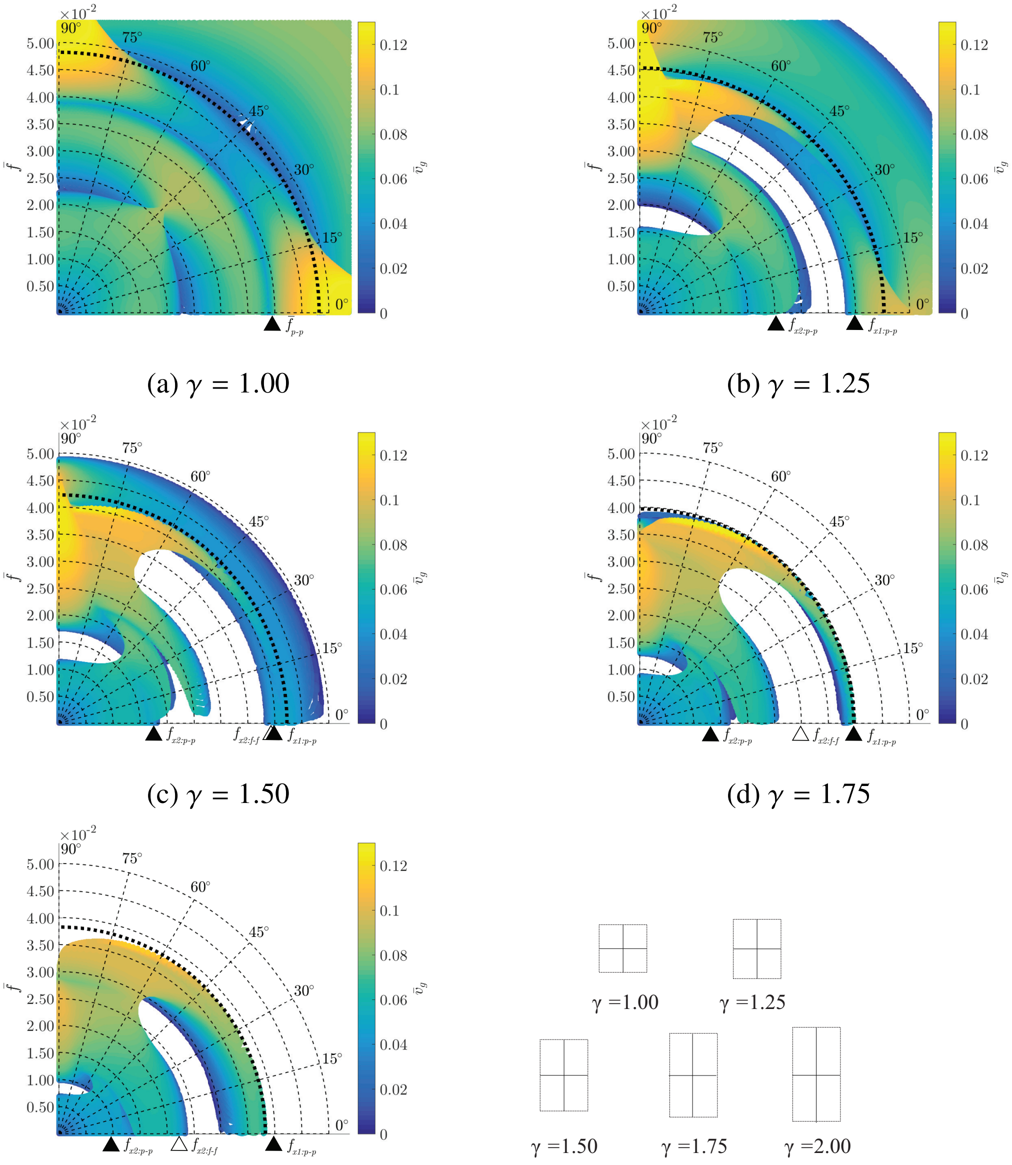

(a) γ = 1.00

(b) γ = 1.25

(c) γ = 1.50

(d) γ = 1.75

(e) γ = 2.00

(f) RUC geometries shown as illustrative primary cell of the lattice.

Figure 4.16: Group velocity direction and magnitude of out-of-plane motion in rectangular lattices of different aspect ratios γ, showing the two lowest out-of-plane frequency surfaces with a black dashed line showing the lowest frequency of the third surface. Solid and open triangles denote resonance frequencies of constituent pinned-pinned and fixed-fixed beams, respectively. When applicable, resonance frequencies of beams aligned with the x_1- and x_2-directions are shown as $f_{xi:pp}$ or $f_{xi:ff}$.

stop-band for $\gamma > 1$ indeed appears centered around the x_2-direction, followed by a higher-frequency band centered around the x_1-direction. As suggested by

P. Wang et al., 2015 due the low coordination number of the rectangular lattice, the observed directional stop-bands could be due to local resonance and, if so, the stop-band should begin at the resonant frequency of a pinned-pinned beam. However, our direct comparison in Fig. 4.16f shows that resonance frequencies do not match consistently with directional stop-band frequencies in each direction, therefore suggesting directional stop-bands in the rectangular lattice are not necessarily linked to local resonance.

Increasing the aspect ratio from $\gamma = 1.25$, both the lower- and higher-frequency directional stop-bands shift to lower frequencies peaking in absolute bandwidth at $\gamma = 1.5$ within the parameter range tested. Furthermore, the angular widths of the lower and higher directional stop-bands decrease from 90° ± 45° and 0° ± 75° to 90° ± 30° and 0° ± 60°, respectively.

λ	$\bar{f}_{\text{fixed-fixed}}$ ($\times 10^{-2}$)	$\bar{f}_{\text{pin-pin}}$ ($\times 10^{-2}$)
1.00	8.90	3.93
1.25	5.70	2.51
1.50	3.95	1.75
1.75	2.91	1.28
2.00	2.22	0.98

Table 4.2: Normalized eigenfrequencies $\bar{f} = \frac{fL}{c}$ of an individual pin-pin or fixed-fixed beam of increasing slenderness $\lambda = l/D$ and circular cross section.

4.6.2 Sheared lattice

As a variation of the rectangular lattice with reduced symmetry, this work proceeds to explore the effect of shearing a square lattice while keeping all member lengths constant. Group velocity distributions for four different shear angles are shown in Fig. 4.17 with RUC geometries depicted in Fig. 4.17e. Focusing on the frequency range $\bar{f} = 0 - 4.00 \cdot 10^{-2}$, one can observe the development of a stop-band at approximately $\bar{f} = 4.00 \cdot 10^{-2}$, close to the natural frequency of an individual pinned-pinned beam. For the shown shear range, the frequency range of the primary stop-band is largest (and the angular width smallest) for $\theta = 45°$. Within the two frequency ranges $\bar{f}_l \in (0, 2\cdot 10^{-2})$ and $\bar{f}_h \in (2\cdot 10^{-2}, 4\cdot 10^{-2})$, highest group velocities are detected in the directions corresponding to angles θ and $\theta/2$, respectively. Specifically, in the lower range, frequencies $\bar{f}_l$ beam along the direction of the angled beams, while in the higher band frequencies $\bar{f}_h$ beam at half that angle. In general, for all tested configurations with $\theta < 90°$, the group velocity is approximately an order of magnitude higher in the θ and $\theta/2$ directions relative to all other directions.

4.6.3 Hexagonal lattice

Hexagonal lattices are popular wave guides due to their interesting geometry-dependent dispersion relations, see, e.g. Ruzzene, Scarpa, and Soranna, 2003 which focused on only the first dispersion surface. In contrast to prior studies, this work includes higher surfaces (up to 12), account for overlap between surfaces as previously deemed necessary, and vary the interior angle from 120° (regular hexagonal lattice) to 60° degrees (regular triangular lattice) while keeping the lengths of all beams constant. Group velocity distributions are shown in Fig. 4.18 for the seven RUC configurations sketched in Fig. 4.18h.

Through Figs. 4.18a and 4.18g, this work confirms a prior analogous observation for in-plane modes (see, e.g. P. Wang et al. (2015)) that regular hexagonal lattices have no stop-bands while regular triangular lattices have a full stop-band that is approximately $\Delta\bar{f} = 2.40 \cdot 10^{-2}$ wide. The transition between these two regular geometries opens several x_1-centered stop-bands having large angular extensions. Once the lattice is of re-entrant configuration (i.e., $\theta < 90$) one can observe the growth of a full stop-band at approximately $\bar{f} = 3.00 \cdot 10^{-2}$. For the two extreme configurations of $\theta = 120°$ (hexagonal lattice) and $\theta = 60°$ (triangular lattice), one confirms the correlation observed by P. Wang et al., 2015, viz. that stop-band features in lattices with low or high coordination numbers (here, hexagonal or triangular lattices, respectively) display features marked by the pinned-pinned and fixed-fixed resonance frequencies, respectively, of individual lattice members. Figs. 4.18a and 4.18g indeed show that those natural frequencies line up with near-zero ($\theta = 120°$) or non-existent group velocities ($\theta = 60°$)).

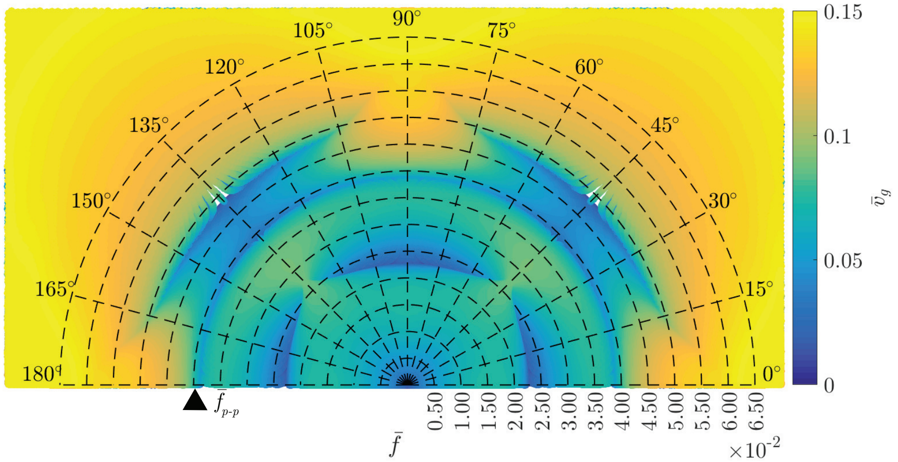

(a) θ = 90° (shown for n = 3)

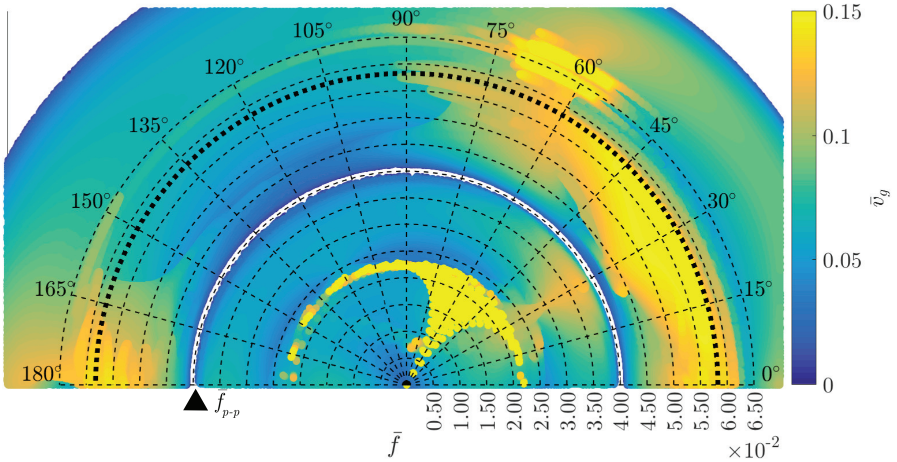

(b) θ = 60° (shown for n = 4)

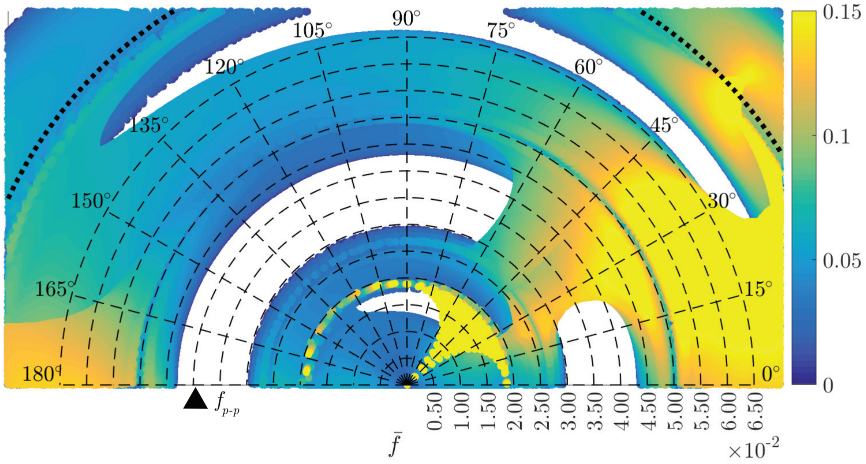

(c) θ = 45° (shown for n = 3)

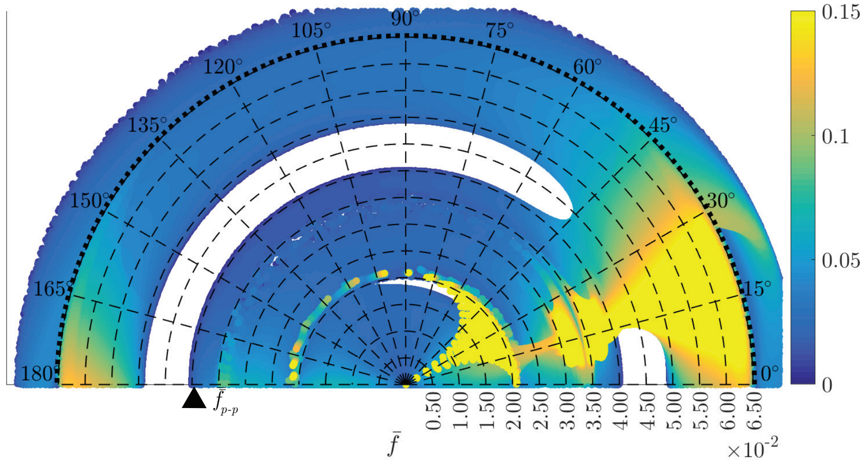

(d) θ = 30° (shown for n = 2)

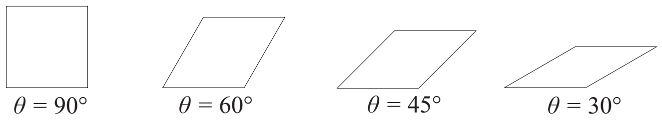

(e) RUC geometries shown as illustrative primary cell of the lattice.

Figure 4.17: Group velocity direction and magnitude of out-of-plane motion in a sheared lattice of different shear levels (internal angles θ), showing the n lowest out-of-plane frequency surfaces with a black dashed line showing the lowest frequency of the $n + 1$ surface. Closed and open triangles denote resonance frequencies of individual pinned-pinned and fixed-fixed constituent beams respectively.

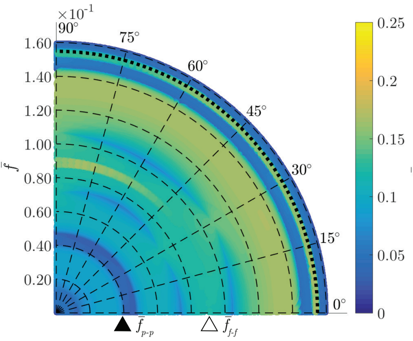

(a) θ = 120° (shown for n = 12)

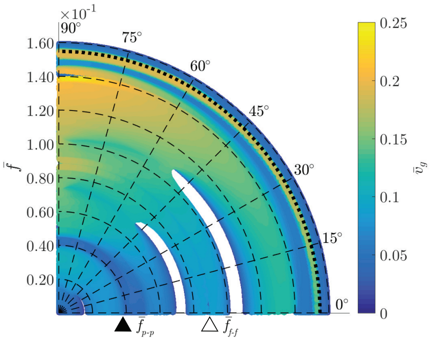

(b) θ = 110° (shown for n = 12)

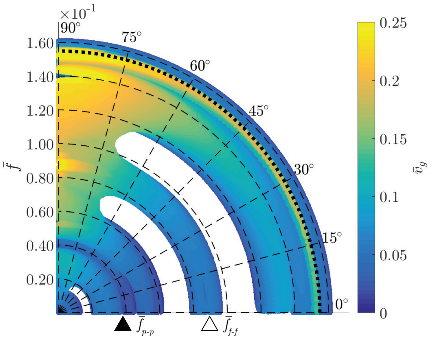

(c) θ = 100° (shown for n = 12)

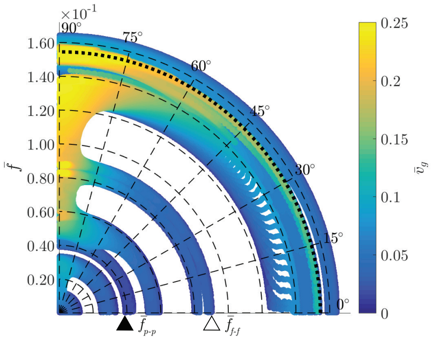

(d) θ = 90° (shown for n = 12)

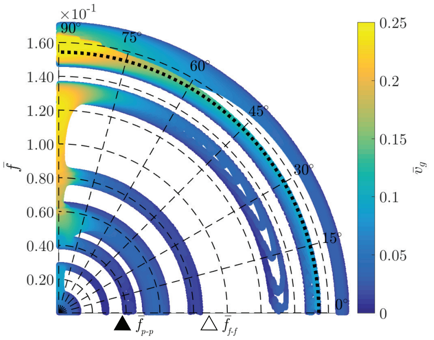

(e) θ = 80° (shown for n = 12)

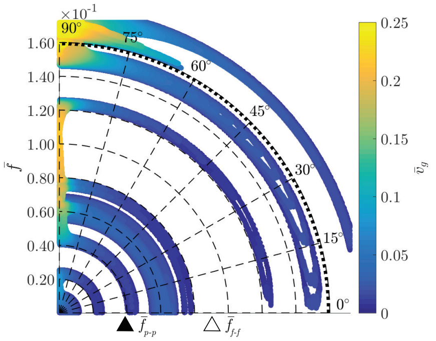

(f) θ = 70° (shown for n = 12)

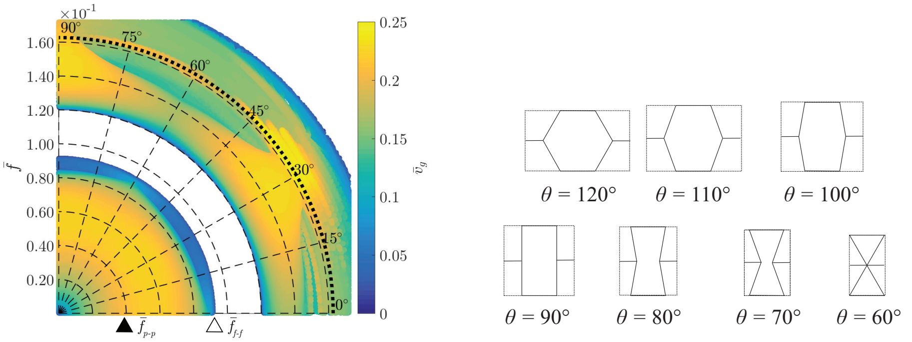

(g) $\theta = 60°$ (shown for $n = 4$)

(h) RUC geometries shown as illustrative primary cell of the lattice.

Figure 4.18: Group velocity direction and magnitude of out-of-plane motion of a periodic hexagonal lattice of different internal angles θ, showing the n lowest out-of-plane frequency surfaces with a black dashed line showing the lowest frequency of the $n + 1$ surface. Black and white triangles denote resonance frequencies of constituent sized pin-pin and fixed-fixed beams respectively.

4.6.4 Validation by transient simulations

To validate the above methodology to predict directional stop-bands and wave beaming, this work compares dispersion relation derived results to transient dynamic simulations of vibrations in rectangular lattices of finite size. This scenario is chosen deliberately to avoid artifacts of periodic boundary conditions or plane-wave assumptions. Each lattice center is excited harmonically at a chosen frequency in the out-of-plane direction by applying a time-harmonic essential boundary condition of the form of Eq. (4.26).

Consider the rectangular lattice with $\gamma = 1.5$ whose group velocity distribution was shown in Fig. (4.16c). Keeping in mind the reflectional symmetries of the lattice, one observe a directional stop-band centered at $\bar{f} = 1.5 \cdot 10^{-2}$ covering the range of $90 \pm 30^\circ$ and a larger directional stop-band at $\bar{f} = 3.5 \cdot 10^{-2}$ covering $0 \pm 65^\circ$. Next, a few specific excitation frequencies are chosen to illustrate the directional variation of the group velocity and explore the dynamic behavior when the lattice is excited within directional stop-bands. For each frequency, compares are made between an explicit dynamic simulation as detailed in Section 4.3.3 with magnitude and direction of group velocities generated from the dispersion surfaces.

For cleaner interpretation of transient simulation results, one performs temporal Fourier analysis at selected lattice points in the x_1- and x_2-directions, labeled $\boldsymbol{x}^{(mx_1)}$ and $\boldsymbol{x}^{(mx_2)}$, respectively; see Fig. 4.20. FFT analysis was performed for times $t > 3/f_e$, allowing displacements to reach an approximately stead-state. Note that some numerical frequency dispersion of the input signal is expected as the lattice is initially at rest.

4.6.5 Explicit Dynamics

In general, there are two types of time-update methods, implicit and explicit, to solve the discrete equations of dynamic motion

$$\boldsymbol{M}\ddot{\boldsymbol{u}} + \boldsymbol{C}\dot{\boldsymbol{u}} + \boldsymbol{K}\boldsymbol{u} = \boldsymbol{f} \ , \tag{4.28}$$

where $\boldsymbol{M}$ is the mass matrix, $\boldsymbol{C}$ the damping matrix, $\boldsymbol{K}$ the stiffness matrix, and $\boldsymbol{u}, \dot{\boldsymbol{u}}, \ddot{\boldsymbol{u}}$ are the displacement, velocity, and acceleration vectors, respectively. There are countless variations of these methods aiming to increase computational performance and improve the stability of the solution for a given time step size. The details and differences of each method are beyond the scope of this work, but the time-stepping method used in this analysis will be discussed in brief.

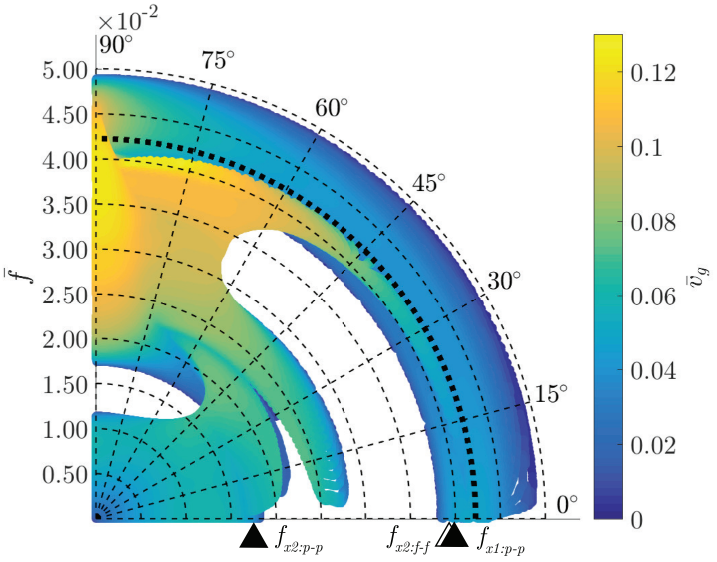

Figure 4.19: First two out-of-plane dispersion surfaces for a rectangular lattice ($\gamma = 1.5$). The dashed black line represents the minimum frequency of the third surface.

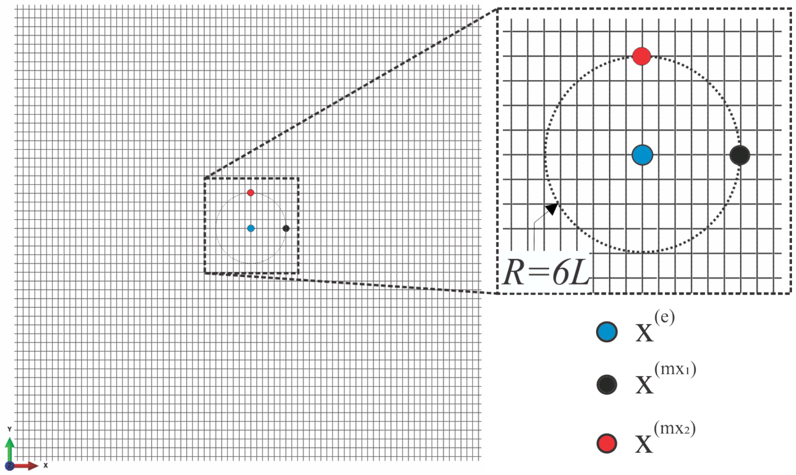

Figure 4.20: Excitation location (*blue*) and measurement locations (*red and black*) in a rectangular lattice ($\gamma = 1.5$) made of 81 × 55 RUCs in the $x_1 \times x_2$-directions.

An explicit update rule is used as it scales well with increasing problem sizes. The explicit updated rule uses the central difference method to approximate the accelerations as

$$\ddot{\boldsymbol{u}} = \frac{1}{\Delta t^2}\left(\boldsymbol{u}^{t-\Delta t} - 2\boldsymbol{u} + \boldsymbol{u}^{t+\Delta}\right) \tag{4.29}$$

and velocity as

$$\dot{\boldsymbol{u}} = \frac{1}{2\Delta t}\left(\boldsymbol{u}^{t+\Delta t} - \boldsymbol{u}^{t-\Delta t}\right) , \tag{4.30}$$

knowing our approximation error scales with $(\Delta t)^2$ and enforcing the need for a relatively small time step for each update. Substituting both of these approximations into Eq. (4.29) and solving for the displacements at $t + \Delta t$, one obtains

$$\left(\frac{1}{\Delta t^2}\boldsymbol{M} + \frac{1}{2\Delta t}\boldsymbol{C}\right)\boldsymbol{u}^{t+\Delta t} = \boldsymbol{f} - \left(\boldsymbol{K} - \frac{2}{\Delta t^2}\boldsymbol{M}\right)\boldsymbol{u}^{t} - \left(\frac{1}{\Delta t^2}\boldsymbol{M} - \frac{1}{2\Delta t}\boldsymbol{C}\right)\boldsymbol{u}^{t-\Delta t} \quad (4.31)$$

This method is used primarily with a lumped mass matrix (diagonal entries only). When neglecting the velocity-dependent damping term, (4.31) no longer requires the solution of a linear system but simply involves division by the diagonal components of $\boldsymbol{M}$ for significantly increased method execution speed.

4.6.5.1 Pass-band at $\bar{f} = 10^{-2}$

For the excitation frequency $\bar{f} = 10^{-2}$ one finds convincing agreement between explicit dynamic simulation results (Fig. 4.21a) and predicted group velocity directions (Fig. 4.21b). The group velocity is nearly uniform in all directions, matching the near-uniform wave front of the dynamic simulation. FFT analysis confirms that the measurement points primarily experience the excitation frequency with slight frequency dispersion.

4.6.5.2 Directional stop-band in the x_2-Direction at $\bar{f} = 1.50 \cdot 10^{-2}$

Exciting the rectangular lattice at $\bar{f} = 1.5 \cdot 10^{-2}$, one again finds convincing agreement between dynamic simulations (Fig. 4.22a) and dispersion relation-generated group velocities (Fig. 4.22b). Waves with higher amplitudes travel primarily in the x_1-direction with the expected angular variance. Two group velocities exist for several directions, where the larger magnitude of either of the two velocities dictates the shape of the wave front seen in transient dynamic simulations. The time history response at $\boldsymbol{x}^{(mx_2)}$ (Fig. 4.22c) reveals an amplitude 1/3rd that at $\boldsymbol{x}^{(mx_1)}$ consistent with the expected wave attenuation. According to the FFT analysis (Fig. 4.22d), this reduction is achieved with minimal frequency dispersion.

4.6.5.3 Directional Stop-Band in x_1-Direction at $\bar{f} = 2.25 \cdot 10^{-2}$

As shown in Fig. 4.23a, and predicted by the dispersion analysis (see Fig. 4.23b), increasing the excitation frequency to $\bar{f} = 2.25 \cdot 10^{-2}$ leads to wave beaming in the x_1-direction. At this frequency two dispersion surfaces exist, making the superposition of out-of-plane modes indistinguishable in Fig. 4.23a. Time history (Fig. 4.23c) and frequency analysis plots (Fig. 4.23d) demonstrate that in both x_1-

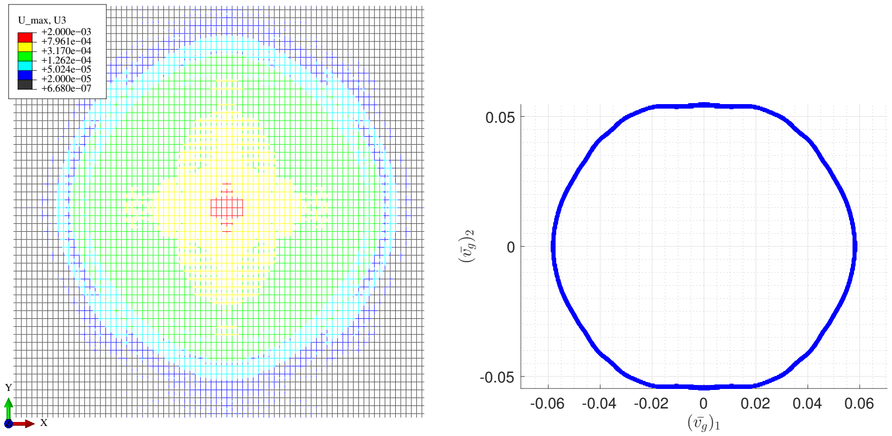

(a) Displacement envelope of explicit dynamic simulation defined as $\max_{t\in(0,t_f)} u_3(\boldsymbol{x},t)$ where $t_f = 1.07\times10^{-1}s$

(b) Group velocity magnitude and direction obtained from dispersion surfaces

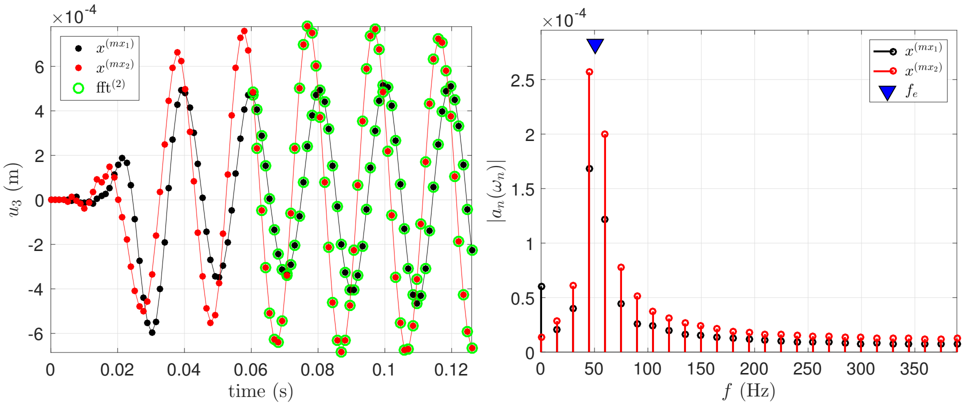

(c) Displacement time history of measurement points $\boldsymbol{x} = \boldsymbol{x}^{(mx_1)}$ and $\boldsymbol{x} = \boldsymbol{x}^{(mx_2)}$

(d) FFT results for $t > 3/f_e$

Figure 4.21: Rectangular lattice response for an excitation frequency $\bar{f} = 10^{-2}$ ($\gamma = 1.5,\ L = 1$).

and x_2-directions there is a relatively long time to reach an effective steady state response as compared to all other tested frequencies. However, one notes that despite the increased frequency dispersion the excitation frequency coefficient in the FFT spectrum is clearly most dominant.

4.6.5.4 Pass-Band at $\bar{f} = 2.75 \cdot 10^{-2}$

At an excitation frequency of $\bar{f} = 2.75 \cdot 10^{-2}$ one finds group velocity in all directions. Our dynamic simulations agree with dispersion surface generated group velocities in terms of directional beaming, but the frequencies within the wave front

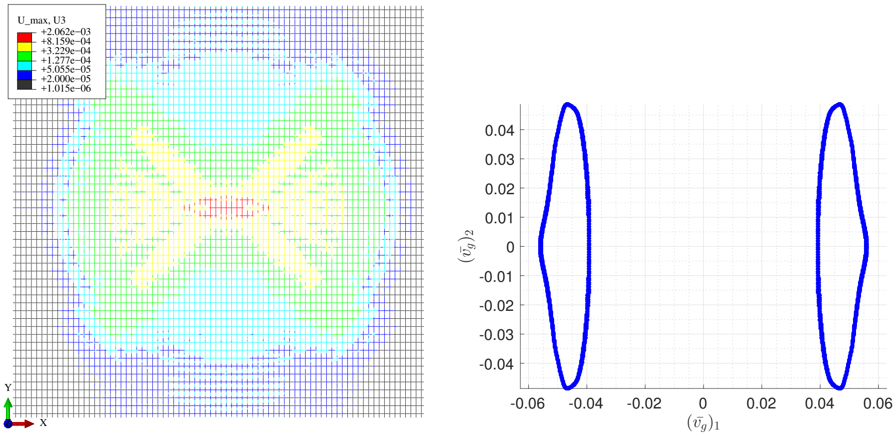

(a) Displacement envelope of explicit dynamic simulation defined as $\max_{t\in(0,t_f)} u_3(\boldsymbol{x},t)$ where $t_f = 1.07\times10^{-1}s$

(b) Group velocity magnitude and direction obtained from dispersion surfaces

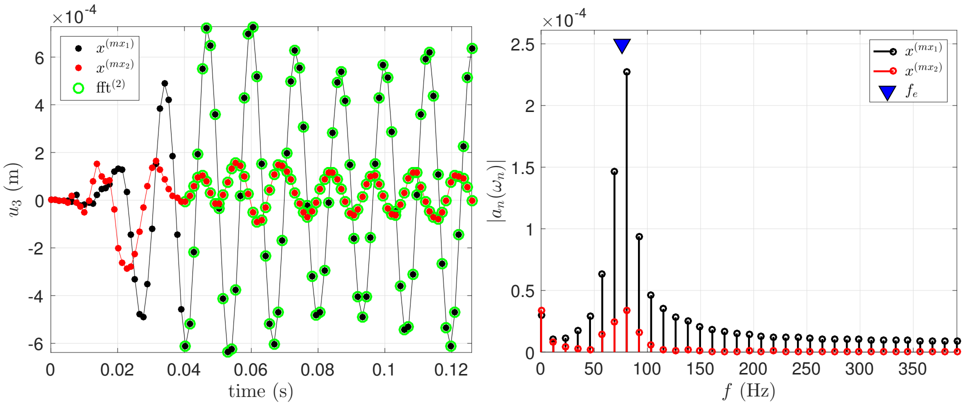

(c) Displacement time history of measurement points $\boldsymbol{x} = \boldsymbol{x}^{(mx_1)}$ and $\boldsymbol{x} = \boldsymbol{x}^{(mx_2)}$

(d) FFT results for $t > 3/f_e$

Figure 4.22: Rectangular lattice response for an excitation frequency $\bar{f} = 1.5\cdot10^{-2}$ $(\gamma = 1.5,\ L = 1)$.

are not predicted in the x_1-direction. Time history and FFT analysis reveal the excitation frequency is highly suppressed with frequency dispersion throughout the neighboring band.

4.6.5.5 Directional stop-band in the x_1-direction at $\bar{f} = 3.46\cdot10^{-2}$

In the excitation frequency of $\bar{f} = 3.46\times10^{-2}$, one finds highly directional beaming with wide stop-bands in the $\pm x_1$-directions confirmed by dynamic simulations. Time history analysis reveals a relatively short transient period; in the x_2-direction FFT analysis shows dominance nearest to the input frequency with broad-band dispersion

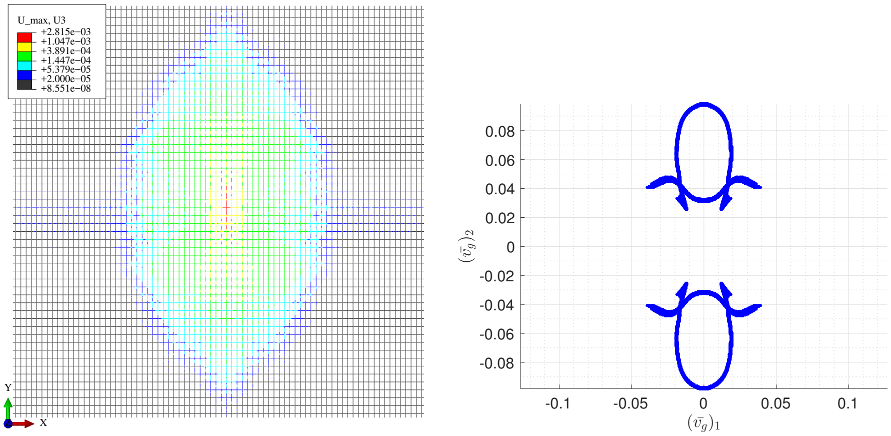

(a) Displacement envelope of explicit dynamic simulation defined as $\max_{t\in(0,t_f)} u_3(\boldsymbol{x},t)$ where $t_f = 5.88\times 10^{-2}s$

(b) Group velocity magnitude and direction obtained from dispersion surfaces

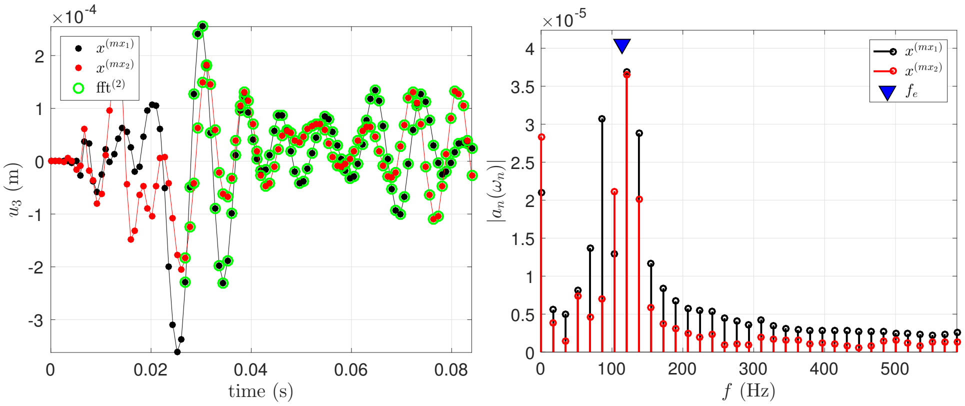

(c) Displacement time history of measurement points $\boldsymbol{x} = \boldsymbol{x}^{(mx_1)}$ and $\boldsymbol{x} = \boldsymbol{x}^{(mx_2)}$

(d) FFT results for $t > 3/f_e$

Figure 4.23: Rectangular lattice response to excitation frequency $\bar{f}_e = 2.26$ ($\gamma = 1.5,\ L = 1$)

in the x_1-direction.

4.6.5.6 Pass-band at $\bar{f} = 3.97\cdot 10^{-2}$

The highest excitation frequency examined, $\bar{f} = 3.97\cdot 10^{-2}$, demonstrates the limitations of predicting the lattice response from dispersion relations. According to the dispersion relation, we expect a full pass-band whereas dynamic simulations show the relative magnitude of out-of-plane displacements having preferential directions. Dispersion relations are not incorrect, but do not reveal how much energy is propagated in each direction and the possible interactions of resonance believed to exist in

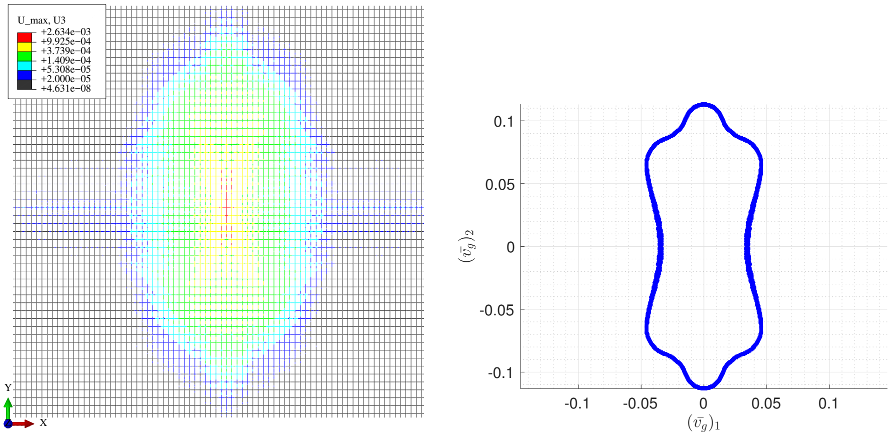

(a) Displacement envelope of explicit dynamic simulation defined as $\max_{t\in(0,t_f)} u_3(\boldsymbol{x},t)$ where $t_f = 5.60 \times 10^{-2} s$

(b) Group velocity magnitude and direction obtained from dispersion surfaces

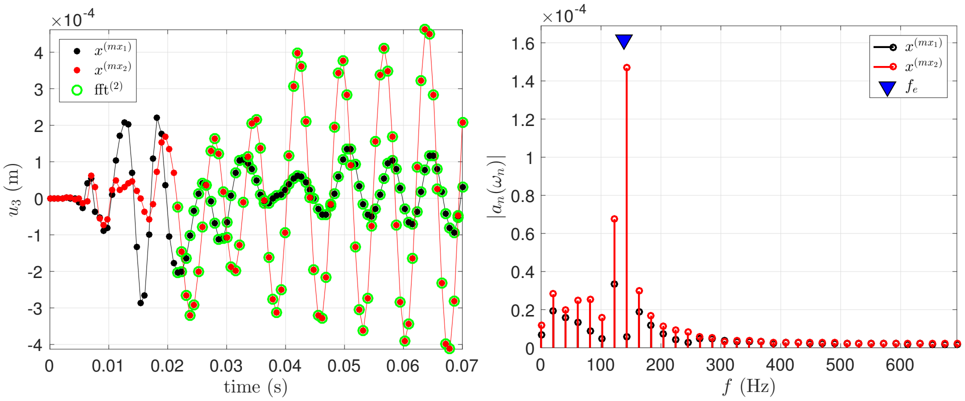

(c) Displacement time history of measurement points $\boldsymbol{x} = \boldsymbol{x}^{(mx_1)}$ and $\boldsymbol{x} = \boldsymbol{x}^{(mx_2)}$

(d) FFT results for $t > 3/f_e$

Figure 4.24: Rectangular lattice response to an excitation frequency $f_e = 2.75 \cdot 10^{-2}$ ($\gamma = 1.5,\ L = 1$).

the dynamic simulation. Time histories show amplitudes in the x_2-direction about 700% higher than in the x_1-direction, for which FFT analysis confirms that those appear at the excitation frequency.

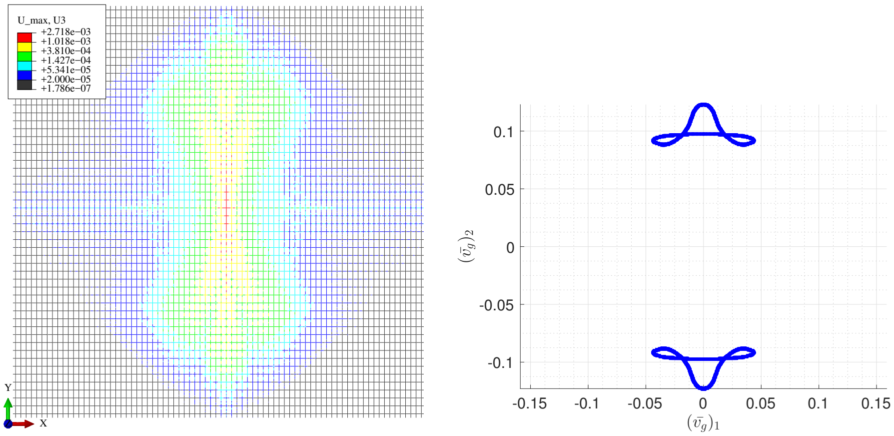

(a) Displacement envelope of explicit dynamic simulation defined as $\max_{t\in(0,t_f)} u_3(\boldsymbol{x},t)$ where $t_f = 5.67\times10^{-2}s$

(b) Group velocity magnitude and direction obtained from dispersion surfaces

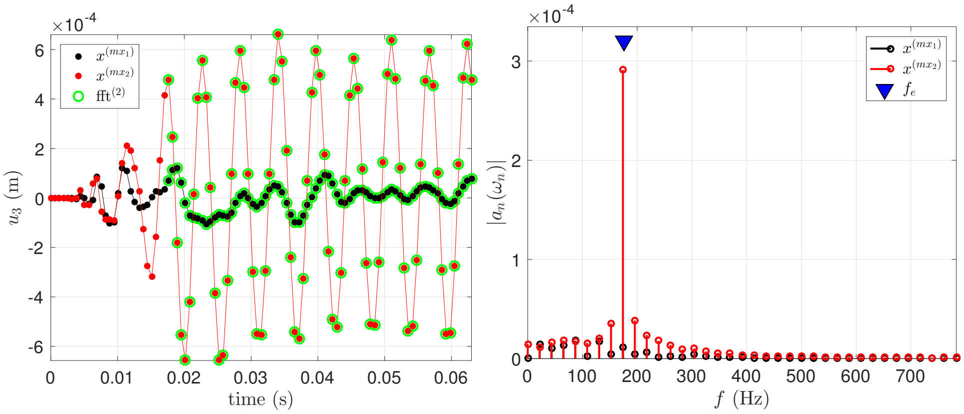

(c) Displacement time history of measurement points $\boldsymbol{x} = \boldsymbol{x}^{(mx_1)}$ and $\boldsymbol{x} = \boldsymbol{x}^{(mx_2)}$

(d) FFT results for $t > 3/f_e$

Figure 4.25: Rectangular lattice response to an excitation frequency $\bar{f} = 3.46\cdot10^{-2}$ ($\gamma = 1.5,\ L = 1$).

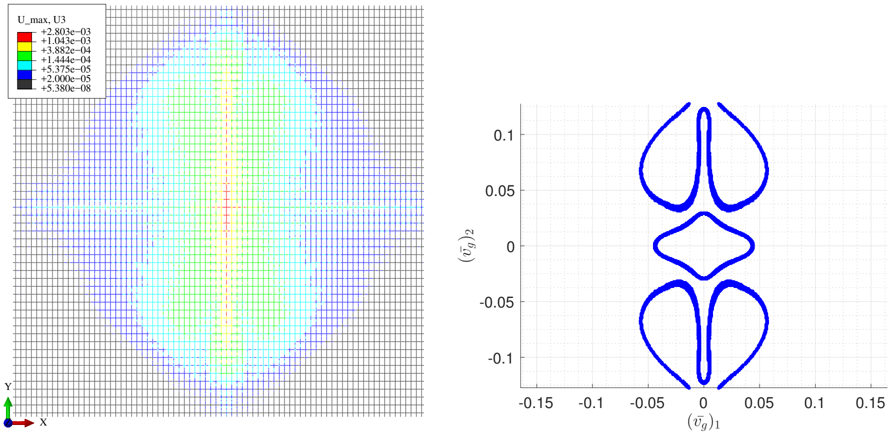

(a) Displacement envelope of explicit dynamic simulation defined as $\max_{t\in(0,t_f)} u_3(\boldsymbol{x},t)$ where $t_f = 5.35\times10^{-2}s$

(b) Group velocity magnitude and direction obtained from dispersion surfaces

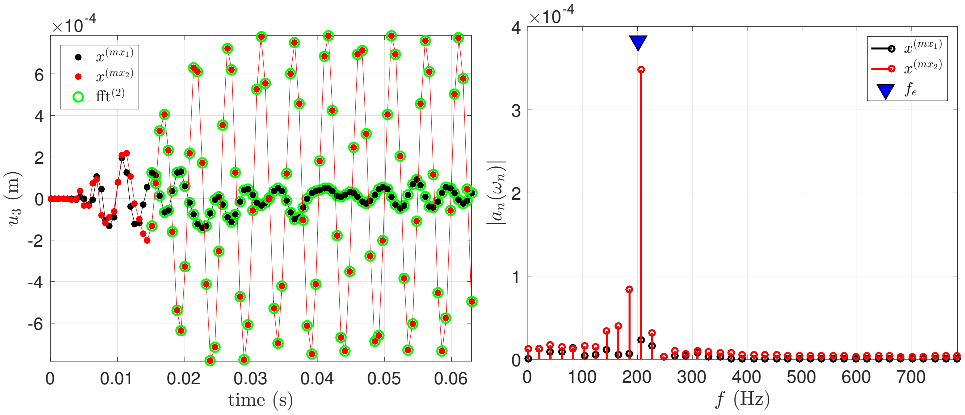

(c) Displacement time history of measurement points $\boldsymbol{x} = \boldsymbol{x}^{(mx_1)}$ and $\boldsymbol{x} = \boldsymbol{x}^{(mx_2)}$

(d) FFT results for $t > 3/f_e$

Figure 4.26: Rectangular lattice response to an excitation frequency $\bar{f} = 3.97\cdot10^{-2}$ ($\gamma = 1.5,\ L = 1$).

4.6.6 Discussion

This work has revealed new opportunities for detecting and optimizing wave beaming through lattice architecture and has shown that:

- Predicting directional wave guiding requires the consideration of more than only the lowest dispersion surface.
- Isolating and interpolating dispersion surfaces corresponding to out-of-plane vibrations yields continuous approximate maps of group velocity magnitude vs. direction and frequency.
- Group velocity analysis is well suited to predict beaming, confirmed by comparison to transient simulations. In addition to (full and partial) stop-bands, the new group velocity maps can also indicate directions of low energy propagation even if no band gaps exist, as discussed below.
- Unlike dispersion relations, the shown group velocity maps show wave characteristics at every point in the IBZ rather than along a characteristic path.
- Variations in simple 2D lattice architectures can be used to control full and partial band gaps.
- In general, partial and full stop-bands are not well predicted by the natural frequencies of individual constituent beams with pinned-pinned or fixed-fixed boundary conditions.

The presented techniques improve upon existing strategies to identify wave beaming in structural lattices. Specifically, the newly-introduced continuous group velocity maps highlight band gaps across wide ranges of frequencies and propagation direction in an illustrative manner. One should note that results depend on the chosen approximation made by interpolating dispersion surfaces so that, e.g. narrow-frequency stop-bands may be missed if spline-interpolated surfaces overlap (while the actual surfaces do not). However, this level of resolution can be controlled exactly through (a) the choice of interpolation and (b) the number of discrete points in $\boldsymbol{k}$-space based on which the dispersion surfaces are calculated. Besides, the same problem arises in a much more pronounced manner in the more traditional group velocity calculations based on iso-frequency contour plots (see, e.g. Ruzzene, Scarpa, and Soranna, 2003). It is important to point out that we evaluate the dispersion relation at (approximately) every point in the IBZ rather than along a characteristic path (e.g. Casadei and Rimoli, 2013), which may miss stop-bands within the IBZ and, especially, cannot make definite statements about beaming within the IBZ. Unlike stop-bands, beaming – as observed in experiments – requires a considerably higher group velocity in specific directions at a given frequency. Therefore, identifying stop-bands only (i.e., regions in which no group velocity exists) may fail to predict beaming accurately.

Consider, e.g. the hexagonal lattice whose group velocity map was shown in Fig. 4.11b and showed strong directionality at $\bar{f} = 1.00 \cdot 10^{-2}$, even though no stop-band appears. Fig. 4.27 shows the corresponding dynamic simulation results and iso-frequency group velocity plot, confirming the predictions of Fig. 4.11b.

In contrast to related prior investigations (Casadei and Rimoli, 2013; Gonella and Ruzzene, 2008a; Gonella and Ruzzene, 2008b), this analysis did not make use of phase velocities in this investigation, among others, because we find that phase velocities are hard to compute unambiguously (they involve division by the complex-valued wave vector components which, for higher-order dispersion surfaces, may become questionable due to periodic translational invariance).

The presented methods can be extended to 3D lattices with increased complexity (and without the separation into in- and out-of-plane modes). Also, the chosen application to beam lattices can be generalized: FE discretizations using plate/shell elements to represent continuous 2D periodic media (such as composites, woven

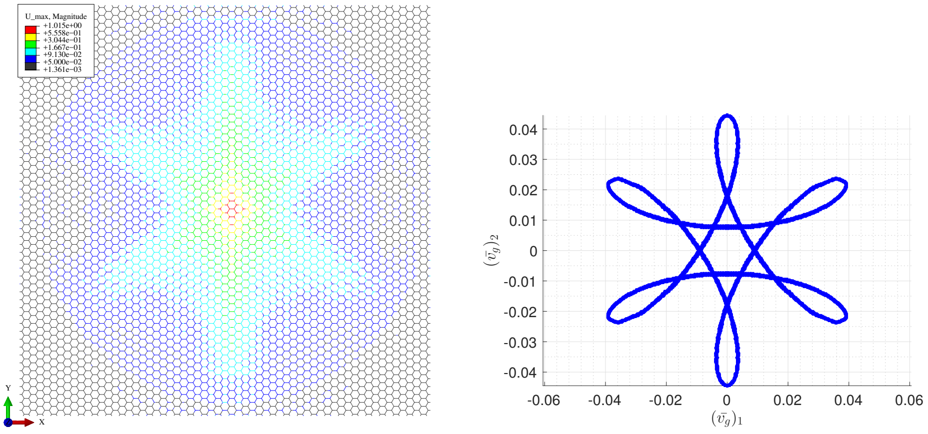

(a) Displacement envelope of explicit dynamic simulation defined as $\max_{t \in (0,t_f)} u_3(\boldsymbol{x}, t)$ where $t_f = 1.95 \times 10^{-1} s$

(b) Group velocity magnitude and direction obtained from dispersion surfaces

Figure 4.27: Hexagonal unit cell ($\theta = 120°$) excited at $\bar{f} = 1.00 \cdot 10^{-2}$ with strong directionality.

networks, or 2D materials) can be used to generate group velocity maps in an analogous fashion.

Ongoing work applies the methods presented here to hollow-tube lattices, which are becoming more prevalent in low-density metamaterials (Meza, Das, et al., 2014; Montemayor et al., 2014; Zheng et al., 2014) but pose new challenges due to the existence of complex torsional and breathing modes affecting the dispersion relations of the now shell-like structures.

4.7 Conclusions

This work presented a method to produce continuous, approximate frequency-dependent group velocity maps for the identification of full and partial stop-bands as well as of wave beaming in periodic 2D structural lattices. By isolating out-of-plane modes, interpolating dispersion surfaces and computing their gradients analytically, the applicability of the proposed group velocity maps for three types of lattices having rectangular, sheared-square, and hexagonal unit cells has been demonstrated. By varying the lattice architecture while preserving their topology (e.g. changing the aspect ratio or shear angle in rectangular and sheared lattices, respectively), the importance of geometry on wave propagation (each lattice type showing different sensitivity to geometric changes) has been highlighted. Predicted directional wave propagation for selected lattices is confirmed by transient dynamic simulation.

Chapter 5

SUMMARY

> *Scientists study the world as it is; engineers create the world that has never been. - Theodore Von Kármán*

5.1 Conclusions

Society is constantly demanding new and improved technology, such as cell phones or transportation, and engineers and scientist have a choice. One can either *design* something better or make it of a better *material*. The latter of two is more impactful as it is not geometrically specific to a single problem. Specifically, density greatly affects performance. Additive manufacturing allows one to explore extremely lightweight materials in the form of cellular materials consisting of a solid phase and fluid phase. Often this fluid is a gas and cellular materials take shape in stochastic micro-geometry as foams or in highly organized ways as lattices. A range of different cellular materials have been developed as engineering materials, but of the set, lattice materials hold promise as being exceptionally efficient as one has direct control over the microstructure. In pursuit of improved materials this thesis has selected low-density, high-stiffness, and high effective-damping as key factors to focus on and has shown how lattice materials can enter into this property space.

Chapter 3 focused on how to use hierarchical structure in lattices to achieve high stiffness for a given relative density. Multiple length scales were introduced creating first-, second-, and third-order hierarchical lattice materials. Finite element simulations predict, and experimental results verify, using structural hierarchy enables lattice materials to reach relative densities as low as 10^{-4} while maintaining near-ideal stretching-dominated stiffness scaling within the geometric parameters tested. A computational methodology based on finite-element substructuring was employed to gain the efficiency required to simulate complex hierarchical lattices containing large numbers of individual truss members (impractical and inefficient using full-resolution finite element methods).

In the pursuit of effective wave attenuation, Chapter 4 examined the unique property of directional damping, or energy beaming, in lattice materials. A new method based on dispersion relations clearly showed that unit cell design highly influences directional stop-band frequency width and directionality. This method is a significant improvement over previous methods by combining frequency, group velocity directionality, and group velocity magnitude into single figure. Explicit dynamic simulations validated this new method accurately predicts group velocity directionality for different frequencies.

5.2 Future directions

As this thesis shows, hierarchical structural lattices can reach very low relative densities while maintaining stretching-dominated behavior for a given geometric parameter set. However, the effect of different unit cell designs at different member slenderness is unclear. Fruitful investigations may come from:

- applying the equilibrium matrix and rank-finding method described in (Pellegrino and Calladine, 1986) to sort a host of slender-member, fundamental unit cell designs into stretching-dominated or bending-dominated
- vary the slenderness of each fundamental unit cell design and find scaling relations for stiffness and strength
- evaluate the stiffness scaling of hierarchical structures across several orders and the determine when and how each level plays a role in the effective properties
- as presented in this thesis, lattice materials can have significantly decreased properties due to geometric imperfections, such as waviness. Is there a fundamental lattice member, i.e. beam, one could design in terms of cross-section and length, such that geometric imperfections have the little affect on stiffness or strength?
- exploring the inelastic deformation of hierarchical lattices. Model-order reduction techniques, similar to the Guyan method present in this thesis, are needed to capture the non-linear deformation to obtain a tractable computational analysis.
- taking advantage of the multiple length scales of hierarchical lattices and instituting size effects, such as those observed for metallic grain size, on the smallest lattice length scale. This could lead to small scale size effects increasing performance on the largest scale.

With regards to dynamic properties there are many unanswered questions about how waves travel through lattices, in particular through hollow lattices such as those fabricated experimentally. In comparison with solid lattices, hollow lattices have low frequency deformation modes including torsion and breathing. These additional modes all combined-mode shapes within the dispersion relation making it difficult to identify a single mode for a given dispersion surface. Future research opportunities could include:

- explore the relations between geometric parameters of length, diameter, and thickness and how a hollow lattice junction transmits waves in a periodic system
- design the hollow lattice to suppress certain deformation modes via stiffening ribs similar to aircraft structures, creating stop bands in the dispersion relation
- make comparisons between finite-element-predicted dispersion responses and experimentally realized micro- or nanoscale samples.

BIBLIOGRAPHY

Abdel-Rahman, A. Y. A. and M. Petyt (1980). “Free and forced wave propagation in two-dimensional periodic systems using matrix techniques”. In: *Recent Advances in Structural Dynamics*. Vol. 1. Institute of Sound and Vibration Research, University of Southampton, pp. 361–373.

Aberg, M. (1997). “The usage of standard finite element codes for computation of dispersion relations in materials with periodic microstructure”. In: *The Journal of the Acoustical Society of America* 102.4, p. 2007. ISSN: 00014966. DOI: `10.1121/1.419652`. URL: `http://scitation.aip.org/content/asa/journal/jasa/102/4/10.1121/1.419652`.

Abrahamson, A. L. (1973). “The response of periodic structures to aero-acoustic pressures, with particular reference to aircraft skin-rib spar structures”. PhD thesis. University of Southampton.

Aizenberg, Joanna et al. (2005). “Skeleton of Euplectella sp.: structural hierarchy from the nanoscale to the macroscale.” In: *Science (New York, N.Y.)* 309.1985, pp. 275–278. ISSN: 0036-8075. DOI: `10.1126/science.1112255`.

Ajdari, Amin et al. (2012). “Hierarchical honeycombs with tailorable properties”. In: *International Journal of Solids and Structures* 49.11-12, pp. 1413–1419. ISSN: 00207683. DOI: `10.1016/j.ijsolstr.2012.02.029`. URL: `http://dx.doi.org/10.1016/j.ijsolstr.2012.02.029`.

Akil Hazizan, Md. and W. J. Cantwell (2002). “The low velocity impact response of foam-based sandwich structures”. In: *Composites Part B: Engineering* 33.3, pp. 193–204. ISSN: 13598368. DOI: `10.1016/S1359-8368(02)00009-4`. URL: `http://www.sciencedirect.com/science/article/pii/S1359836802000094`.

Anderson, E. et al. (1999). *LAPACK Users’ Guide*. Third. Philadelphia, PA: Society for Industrial and Applied Mathematics. ISBN: 0-89871-447-8.

Ashby, Michael F. (2005). *Materials Selection in Mechanical Design*. Vol. 3rd ed. Butterworth-Heinemann. ISBN: 9780750661683. URL: `https://clsproxy.library.caltech.edu/login?url=http://search.ebscohost.com/login.aspx?direct=true&db=e000xna&AN=189594&site=eds-live&scope=site`.

– (2006). “The properties of foams and lattices”. In: *Philosophical transactions. Series A, Mathematical, physical, and engineering sciences* 364.1838, pp. 15–30. ISSN: 1364-503X. DOI: `10.1098/rsta.2005.1678`. URL: `http://rsta.royalsocietypublishing.org/cgi/doi/10.1098/rsta.2005.1678`.

Ashby, Michael F. and Y. J. M. Bréchet (2003). “Designing hybrid materials”. In: *Acta Materialia* 51.19, pp. 5801–5821. ISSN: 13596454. DOI: `10.1016/S1359-6454(03)00441-5`.

Boa, Jing et al. (2012). “Dynamic Responses of a Structure with Periodic Foundation”. In: *Journal of Engineering Mechanics* 138, pp. 761–769. ISSN: 0733-9399. DOI: `10.1061/(ASCE)EM`. URL: `http://ascelibrary.org/doi/pdf/10.1061/(ASCE)EM.1943-7889.0000387`.

Brakus, Josko (1995). “Mechanical properties of natural materials: an overview”. PhD thesis. Massachusetts Institute of Technology.

Brillouin, Leon (1953). *Wave Propagation in Periodic Structures*. 2nd. Dover Publications.

Brun, Michele et al. (2013). “Phononic Band Gap Systems in Structural Mechanics: Finite Slender Elastic Structures and Infinite Periodic Waveguides”. In: *Journal of Vibration and Acoustics* 135.4, p. 041013. ISSN: 0739-3717. DOI: `10.1115/1.4023819`. URL: `http://vibrationacoustics.asmedigitalcollection.asme.org/article.aspx?doi=10.1115/1.4023819`.

Casadei, Filippo and Julian J. Rimoli (2013). “Anisotropy-induced broadband stress wave steering in periodic lattices”. In: *International Journal of Solids and Structures* 50.9, pp. 1402–1414. ISSN: 00207683. DOI: `10.1016/j.ijsolstr.2013.01.015`. URL: `http://dx.doi.org/10.1016/j.ijsolstr.2013.01.015`.

Christensen, R.M. (2000). “Mechanics of cellular and other low-density materials”. In: *International Journal of Solids and Structures* 37.1-2, pp. 93–104. ISSN: 00207683. DOI: `10.1016/S0020-7683(99)00080-3`. URL: `http://www.sciencedirect.com/science/article/pii/S0020768399000803`.

Corning (2016). *Corning Gorilla Glass 5*. URL: `https://www.corning.com/gorillaglass/worldwide/en/glass-types/gorilla-glass-5.html`.

Cremer, L. and H. O. Leilich (1953). “Zur theorie der biegekettenleiter”. In: *On theory of flexural periodic systems), Arch. Elektr. Uebertrag* 7, pp. 261–270.

Currey, John D. (2014). *The mechanical adaptations of bones*. Princeton University Press.

Deshpande, Vikram S., Michael F. Ashby, et al. (2001). “Foam topology: bending versus stretching dominated architectures”. In: *Acta Materialia* 49.6, pp. 1035–1040. ISSN: 13596454. DOI: `10.1016/S1359-6454(00)00379-7`.

Deshpande, Vikram S. and Norman A. Fleck (2000). “High strain rate compressive behaviour of aluminium alloy foams”. In: *International Journal of Impact Engineering* 24.3, pp. 277–298. ISSN: 0734743X. DOI: `http://dx.doi.org/10.1016/S0734-743X(99)00153-0`. URL: `http://www.sciencedirect.com/science/article/B6V3K-3YB4CXR-5/2/1aea9f8bf342602e2cd7533bfa057cc7`.

Deshpande, Vikram S., Norman A. Fleck, and Michael F. Ashby (2001). “Effective properties of the octet-truss lattice material”. In: *Journal of the Mechanics and Physics of Solids* 49.8, pp. 1747–1769. ISSN: 00225096. DOI: `10.1016/S0022-5096(01)00010-2`.

Economou, E. N. and M. M. Sigalas (1992). “Elastic and Acoustic Wave Band Structure”. In: *Journal of Sound and Vibration* 158.2, pp. 377–382.

Eiffel Tower Gallery (2017). URL: `http://www.toureiffel.paris/en/pictures.html?view=galerie&image_id=35`.

Evans, Anthony G. et al. (2001). “The Topological Design of Multifunctional Cellular”. In: *Progress in Materials Science* 46, pp. 309–327.

Ewins, D. J. (1973). “Vibration characteristics of bladed disc assemblies”. In: *Journal of Mechanical Engineering Science* 15.3, pp. 165–186.

Fan, H L et al. (2008). “Mechanical properties of hierarchical cellular materials. Part I: Analysis”. In: *Composites Science and Technology* 68.15, pp. 3380–3387.

Farr, Robert S. (2007a). *Fractal design for an efficient shell strut under gentle compressive loading*. DOI: `10.1103/PhysRevE.76.056608`. URL: `http://arxiv.org/pdf/1001.3532.pdf`.

– (2007b). “Fractal design for efficient brittle plates under gentle pressure loading”. In: *Physical Review E - Statistical, Nonlinear, and Soft Matter Physics* 76, pp. 1–10. ISSN: 15393755. DOI: `10.1103/PhysRevE.76.046601`.

Farr, Robert S. and Yong Mao (2010). “Fractal space frames and metamaterials for high mechanical efficiency”. In: *EPL (Europhysics Letters)* V.1, pp. 1–6. ISSN: 0295-5075. DOI: `10.1209/0295-5075/84/14001`. URL: `http://arxiv.org/abs/1001.3940`.

Faulkner, M. G. and D. P. Hong (1985). “Free vibrations of a mono-coupled periodic system”. In: *Journal of Sound and Vibration* 99.1, pp. 29–42. ISSN: 10958568. DOI: `10.1016/0022-460X(85)90443-2`.

Fleck, Norman A. and Vikram S. Deshpande (2004). “The Resistance of Clamped Sandwich Beams to Shock Loading”. In: *Journal of Applied Mechanics* 71.May, p. 386. ISSN: 00218936. DOI: `10.1115/1.1629109`.

Fleck, Norman A., Vikram S. Deshpande, and Michael F. Ashby (2010). “Micro-architectured materials: past, present and future”. In: *Proceedings of the Royal Society A: Mathematical, Physical and Engineering Sciences* 466.May, pp. 2495–2516. ISSN: 1364-5021. DOI: `10.1098/rspa.2010.0215`.

Fratzl, Peter and Richard Weinkamer (2007). “Nature’s hierarchical materials”. In: *Progress in Materials Science* 52.8, pp. 1263–1334. ISSN: 00796425. DOI: `10.1016/j.pmatsci.2007.06.001`.

Garabit Viaduct (2009). URL: `http://www.highestbridges.com/wiki/images/b/b5/14GarabitGraemeChurchard.jpg`.

Gibson, Lorna J. (2012). “The hierarchical structure and mechanics of plant materials”. In: *Journal of The Royal Society Interface* 9.76, pp. 2749–2766. ISSN: 1742-5689. DOI: `10.1098/rsif.2012.0341`.

Gibson, Lorna J. and Michael F. Ashby (1988). *Cellular solids: structure and properties*. 1st ed. New York: Pergamon Press, Inc.

Gonella, Stefano and Massimo Ruzzene (2008a). “Analysis of in-plane wave propagation in hexagonal and re-entrant lattices”. In: *Journal of Sound and Vibration* 312, pp. 125–139. ISSN: 0022460X. DOI: `10.1016/j.jsv.2007.10.033`.

– (2008b). “Homogenization and equivalent in-plane properties of two-dimensional periodic lattices”. In: *International Journal of Solids and Structures* 45.10, pp. 2897–2915. ISSN: 00207683. DOI: `10.1016/j.ijsolstr.2008.01.002`.

– (2008c). “Homogenization of vibrating periodic lattice structures”. In: *Applied Mathematical Modelling* 32.4, pp. 459–482. ISSN: 0307904X. DOI: `10.1016/j.apm.2006.12.014`.

Griffin, J. H. and T. M. Hoosac (1984). “Model development and statistical investigation of turbine blade mistuning”. In: *Journal of Vibration, Acoustics, Stress, and Reliability in Design* 106.2, pp. 204–210.

Guyan, Robert J. (1965). “Reduction of stiffness and mass matrices”. In: *AIAA journal* 3.2, p. 380.

Heckl, Manfred A. (1964). “Investigations on the Vibrations of Grillages and Other Simple Beam Structures”. In: *The Journal of the Acoustical Society of America* 36.7.

Hussein, Mahmoud I. et al. (2014). “Dynamics of Phononic Materials and Structures: Historical Origins, Recent Progress, and Future Outlook”. In: *Applied Mechanics Reviews* 66.4, p. 040802. ISSN: 0003-6900. DOI: `10.1115/1.4026911`. URL: `http://appliedmechanicsreviews.asmedigitalcollection.asme.org/article.aspx?doi=10.1115/1.4026911`.

Hutchinson, R. G. and Norman A. Fleck (2006). “The structural performance of the periodic truss”. In: *Journal of the Mechanics and Physics of Solids* 54.October 2005, pp. 756–782. ISSN: 00225096. DOI: `10.1016/j.jmps.2005.10.008`.

Jang, Dongchan et al. (2013). “Fabrication and deformation of three-dimensional hollow ceramic nanostructures”. In: *Nature materials* 12.10, pp. 893–8. ISSN: 1476-1122. DOI: `10.1038/nmat3738`. URL: `http://www.ncbi.nlm.nih.gov/pubmed/23995324%5Cnhttp://www.nature.com/nmat/journal/v12/n10/abs/nmat3738.html`.

Jeong, Sang M. and Massimo Ruzzene (2004). “Directional and band-gap behavior of periodic grid-like structures”. In: 5386.404, pp. 101–111. DOI: `10.1117/12.540352`. URL: `http://proceedings.spiedigitallibrary.org/proceeding.aspx?articleid=842554`.

Jeong, Sang M. and Massimo Ruzzene (2005). “Experimental analysis of wave propagation in periodic grid-like structures”. In: *Smart Structures and Materials 2005: Damping and Isolation* 5760.404, pp. 518–525. ISSN: 0277786X. DOI: `10.1117/12.599709`.

Kochmann, Dennis M. (2014). *Ae108 Lectures Notes*.

Kohrs, Torsten and Bjorn A. T. Petersson (2009). “Wave beaming and wave propagation in light weight plates with truss-like cores”. In: *Journal of Sound and Vibration* 321.1-2, pp. 137–165. ISSN: 0022460X. DOI: `10.1016/j.jsv.2008.09.033`.

Kooistra, Gregory W. et al. (2007). “Hierarchical Corrugated Core Sandwich Panel Concepts”. In: *Journal of Applied Mechanics* 74.March 2007, p. 259. ISSN: 00218936. DOI: `10.1115/1.2198243`.

Krödel, Sebastian et al. (2013). “3D Auxetic Microlattices with Independently Controllable Acoustic Band Gaps and Quasi-Static Elastic Moduli”. In: *Advanced . . .* 9999, n/a–n/a. ISSN: 14381656. DOI: `10.1002/adem.201300264`. URL: `http://doi.wiley.com/10.1002/adem.201300264%20http://onlinelibrary.wiley.com/doi/10.1002/adem.201300264/full`.

Kushwaha, Manvir S. (1996). “Classical Band Structure of Periodic Elastic Composites”. In: *International Journal of Modern Physics B* 10.09, pp. 977–1094. ISSN: 0217-9792. DOI: `10.1142/S0217979296000398`.

Kushwaha, Manvir S. and P. Halevi (1994). “Band-gap engineering in periodic elastic composites”. In: *Applied Physics Letters* 64.9, pp. 1085–1087. ISSN: 00036951. DOI: `10.1063/1.110940`.

Lakes, Roderic S. (1993). “Materials with structural hierarchy”. In: ISSN: 0028-0836. DOI: `10.1038/361511a0`.

Langley, R. S. (1994). *On the modal density and energy flow characteristics of periodic structures*. DOI: `10.1006/jsvi.1994.1191`.

– (1996). “the Response of Two-Dimensional Periodic Structures To Point Harmonic Forcing”. In: *Journal of Sound and Vibration* 197.4, pp. 447–469. ISSN: 0022460X. DOI: `10.1006/jsvi.1996.0542`. URL: `http://linkinghub.elsevier.com/retrieve/pii/S0022460X96905428`.

– (1997a). “The Response of Two-dimensional Periodic Structures to Harmonic Point Loading: A Theoretical and Experimental Study of a Beam Grillage”. In: *Journal of Sound and Vibration* 207.4, pp. 521–535. ISSN: 0022460X.

– (1997b). “The Response of Two-dimensional periodic structures to impulsive point loading”. In: *Journal of Sound and Vibration* 201, pp. 235–253.

Li, Gang and Yaochu Fang (2014). “Failure mode analysis and performance optimization of the hierarchical corrugated truss structure”. In: *Advances in Mechanical Engineering* 2014. ISSN: 16878140. DOI: `10.1155/2014/251591`.

Lin, Yu-Kweng and T. J. McDaniel (1969). “Dynamics of beam-type periodic structures”. In: *Journal of Engineering for Industry* 91.4, pp. 1133–1141.

Liu, Liao and Mahmoud I. Hussein (2012). “Wave Motion in Periodic Flexural Beams and Characterization of the Transition Between Bragg Scattering and Local Resonance”. In: *Journal of Applied Mechanics* 79.1, p. 011003. ISSN: 00218936. DOI: `10.1115/1.4004592`.

Liu, Yaozong et al. (2007). “Design guidelines for flexural wave attenuation of slender beams with local resonators”. In: *Physics Letters, Section A: General, Atomic and Solid State Physics* 362.5-6, pp. 344–347. ISSN: 03759601. DOI: `10.1016/j.physleta.2006.10.056`.

Liu, Zhengyou (2000). “Locally Resonant Sonic Materials”. In: *Science* 289.5485, pp. 1734–1736. ISSN: 00368075. DOI: `10.1126/science.289.5485.1734`. URL: `http://www.sciencemag.org/cgi/doi/10.1126/science.289.5485.1734`.

Liu, Zhengyou et al. (2002). “Three-component elastic wave band-gap material”. In: *Physical Review B* 65.16, p. 165116. ISSN: 0163-1829. DOI: `10.1103/PhysRevB.65.165116`. URL: `http://link.aps.org/doi/10.1103/PhysRevB.65.165116`.

Mace, Brian R. and Elisabetta Manconi (2008). “Modelling wave propagation in two-dimensional structures using finite element analysis”. In: *Journal of Sound and Vibration* 318.4-5, pp. 884–902. ISSN: 0022460X. DOI: `10.1016/j.jsv.2008.04.039`.

Manconi, Elisabetta and Brian R. Mace (2009). “Wave characterization of cylindrical and curved panels using a finite element method”. In: *The Journal of the Acoustical Society of America* 125.1, p. 154. ISSN: 00014966. DOI: `10.1121/1.3021418`.

Mandelbrot, Benoit B. (1982). *The fractal geometry of nature*. 1st ed. San Francisco: WH Freeman, p. 471.

Martinsson, P. G. and Alexander B. Movchan (2002). “Vibration of lattice structures and phononic band gaps”. In: *The Quarterly Journal of of Mechanics and Applied Mathematics* 56.8, pp. 45–64. ISSN: 0033-5614. DOI: `10.1093/qjmam/56.1.45`.

Mead, D. J. (1970). “Free wave propagation in periodically supported, infinite beams”. In: *Journal of Sound and Vibration* 11.2, pp. 181–197. ISSN: 10958568. DOI: `10.1016/S0022-460X(70)80062-1`.

– (1971a). “Space-Harmonic Supported Beams : Analysis of Periodically Response To Convected Loading”. In: *Journal of Sound and Vibration* 14.4, pp. 525–541.

– (1971b). “Vibration response and wave propagation in periodic structures”. In: *Journal of Engineering for Industry* 93.3, pp. 783–792.

– (1973). “A General Theory of Harmonic Wave Propagation in Linear Periodic Systems with Multiple Coupling”. In: *Journal of Sound and Vibration* 27.2, pp. 235–260.

Mead, D. J. (1975). “Wave propagation and natural modes in periodic systems. {II}. Multi-coupled sytems, with and without damping”. In: *Journal of Sound and Vibration* 40(1), pp. 19–39.

Mead, D. J. and A. K. Mallik (1976). “An approximate method of predicting the response of periodically supported beams subjected to random convected loading”. In: *Journal of Sound and Vibration* 47.4, pp. 457–471. ISSN: 10958568. DOI: `10.1016/0022-460X(76)90873-7`.

Mead, D. J. and S. Parthan (1979). “Free Wave Propagation in Two-Dimensional Plates”. In: 64, pp. 325–348.

Meza, Lucas R., Satyajit Das, et al. (2014). “Strong , Lightweight and Recoverable Three - Dimensional Ceramic Nanolattices”. In: *Submitted* 1322. DOI: `10.1126/science.1255908`.

Meza, Lucas R. and Julia R. Greer (2014). “Mechanical characterization of hollow ceramic nanolattices”. In: *Journal of Materials Science* 49.6, pp. 2496–2508. ISSN: 00222461. DOI: `10.1007/s10853-013-7945-x`.

Meza, Lucas R., Greg Phlipot, et al. (2016). “Revisiting the Stiffness Scaling of Rigid and Non-rigid Lattice Architectures”. In: *Under Review*.

Meza, Lucas R., Alex J. Zelhofer, et al. (2015). “Resilient 3D hierarchical architected metamaterials.” In: *Proceedings of the National Academy of Sciences of the United States of America* 112.37, pp. 11502–7. ISSN: 1091-6490. DOI: `10.1073/pnas.1509120112`. URL: `http://www.pnas.org/content/112/37/11502.abstract`.

Montemayor, Lauren C. et al. (2014). “Design and fabrication of hollow rigid nanolattices via two-photon lithography”. In: *Advanced Engineering Materials* 16, pp. 184–189. ISSN: 14381656. DOI: `10.1002/adem.201300254`.

Nemat-Nasser, S. (1972). “General Variational Methods for Waves in Elastic Composites”. In: *Journal of Elasticity* 2.2, pp. 73–90.

Niu, Bin and Bo Wang (2016). “Directional mechanical properties and wave propagation directionality of Kagome honeycomb structures”. In: *European Journal of Mechanics-A/Solids* 57, pp. 45–58.

Oftadeh, Ramin et al. (2014). “Optimal Fractal-Like Hierarchical Honeycombs”. In: *Physical Review Letters* 104301.September, pp. 1–5. ISSN: 0031-9007. DOI: `10.1103/PhysRevLett.113.104301`.

Olson, G. B. (1997). “Computational Design of Hierarchically Structured Materials”. In: *Science* 277.1997, pp. 1237–1242. ISSN: 00368075. DOI: `10.1126/science.277.5330.1237`.

Orris, Ruth M. and M. Petyt (1974). “A Finite Element Study of Harmonic Wave Propagation in Periodic Structures”. In: *Journal of Sound and Vibration* 33.2, pp. 223–236. DOI: `10.1016/S0022-460X(74)80108-2`. URL: `http://dx.doi.org/10.1016/S0022-460X(74)80108-2`.

Ortiz, Christine and Mary C. Boyce (2008). “Bioinspired structural materials”. In: *Science* 14.February, pp. 1053–1054. ISSN: 1095-9203. DOI: `10.1126/science.1154295`. URL: `http://www.sciencemag.org/content/319/5866/1053.short`.

Ottarsson, Gisli et al. (1997). “A Reduced-Order Modeling Technique for Mistuned Bladed Disks”. In: *Journal of Vibration and Acoustics* 119, pp. 439–447. ISSN: 02734508.

Pellegrino, S. and C. R. Calladine (1986). “Matrix Analysis of Statically and Kinematically Indeterminate Frameworks”. In: *Int. J. Solids Structures* 22.4, pp. 409–428.

Phani, A. Srikantha et al. (2006). “Wave propagation in two-dimensional periodic lattices.” In: *The Journal of the Acoustical Society of America* 119.December 2005, pp. 1995–2005. ISSN: 00014966. DOI: `10.1121/1.2179748`.

Qiao, Pizhong et al. (2008). “Impact Mechanics and High-Energy Absorbing Materials : Review”. In: *Journal of Aerospace Engineering* 21.October, pp. 235–248. ISSN: 0893-1321. DOI: `10.1061/(ASCE)0893-1321(2008)21`.

Qu, Zu-Qing (2013). *Model order reduction techniques with applications in finite element analysis*. Springer Science & Business Media.

Queheillalt, Douglas T. and Haydn N. G. Wadley (2005). “Cellular metal lattices with hollow trusses”. In: *Acta Materialia* 53.2, pp. 303–313. ISSN: 13596454. DOI: `10.1016/j.actamat.2004.09.024`.

Rayleigh, Lord (1887). “On the maintenance of vibrations by forces of double frequency, and on the propagation of waves through a medium endowed with a periodic structure”. In: *Philosophical Magazine Series 5* 24.147, pp. 145–159. ISSN: 1941-5982. DOI: `10.1080/14786448708628074`. URL: `http://dx.doi.org/10.1080/14786448708628074`.

Rayneau-Kirkhope, Daniel, Yong Mao, and Robert S. Farr (2012). “Ultralight fractal structures from hollow tubes”. In: *Physical Review Letters* 109.November, pp. 2–5. ISSN: 00319007. DOI: `10.1103/PhysRevLett.109.204301`.

– (2013). “Optimization of fractal space frames under gentle compressive load”. In: *Physical Review E - Statistical, Nonlinear, and Soft Matter Physics* 87, pp. 1–7. ISSN: 15393755. DOI: `10.1103/PhysRevE.87.063204`.

Rayneau-Kirkhope, Daniel, Yong Mao, Robert S. Farr, and Joel Segal (2012). “Hierarchical space frames for high mechanical efficiency: Fabrication and mechanical testing”. In: *Mechanics Research Communications* 46, pp. 41–46. ISSN: 00936413. DOI: `10.1016/j.mechrescom.2012.06.011`. URL: `http://dx.doi.org/10.1016/j.mechrescom.2012.06.011`.

Ruzzene, Massimo, L. Mazzarella, et al. (2002). “Wave Propagation in Sandwich Plates with Periodic Auxetic Core”. In: *Journal of Intelligent Material Systems and Structures* 13.9, pp. 587–597. ISSN: 1045-389X. DOI: `10.1106/104538902031865`.

Ruzzene, Massimo and Fabrizio L. Scarpa (2005). “Directional and band-gap behavior of periodic auxetic lattices”. In: *Physica Status Solidi (B) Basic Research* 242.3, pp. 665–680. ISSN: 03701972. DOI: `10.1002/pssb.200460385`.

Ruzzene, Massimo, Fabrizio L. Scarpa, and Francesco Soranna (2003). “Wave beaming effects in two-dimensional cellular structures”. In: *Smart Materials and Structures* 12, pp. 363–372. ISSN: 0964-1726. DOI: `10.1088/0964-1726/12/3/307`.

Rys, Jan et al. (2014). “Fabrication and deformation of metallic glass micro-lattices”. In: *Advanced Engineering Materials* 16, pp. 889–896. ISSN: 15272648. DOI: `10.1002/adem.201300454`.

Schaedler, Tobias A. and William B. Carter (2016). “Architected Cellular Materials”. In: *Annual Review of Materials Research* 46.1, pp. 187–210. ISSN: 1531-7331. DOI: `10.1146/annurev-matsci-070115-031624`. URL: `http://www.annualreviews.org/doi/10.1146/annurev-matsci-070115-031624`.

Schaedler, Tobias A., Alan J. Jacobsen, et al. (2011). “Ultralight Metallic Microlattices”. In: *Science* 334.2011, pp. 962–965. ISSN: 0036-8075. DOI: `10.1126/science.1211649`.

Shan, Sicong et al. (2015). “Multistable Architected Materials for Trapping Elastic Strain Energy”. In: *Advanced Materials* 27.29, pp. 4296–4301. ISSN: 15214095. DOI: `10.1002/adma.201501708`.

Sigalas, M. and E. N. Economou (1993). *Band structure of elastic waves in two dimensional systems*. DOI: `10.1016/0038-1098(93)90888-T`.

Sigmund, Ole and Jakob Søndergaard Jensen (2003). “Systematic design of phononic band-gap materials and structures by topology optimization.” In: *Philosophical transactions. Series A, Mathematical, physical, and engineering sciences* 361.1806, pp. 1001–19. ISSN: 1364-503X. DOI: `10.1098/rsta.2003.1177`. URL: `http://www.ncbi.nlm.nih.gov/pubmed/12804226`.

Spadoni, Alessandro et al. (2009). “Phononic properties of hexagonal chiral lattices”. In: *Wave Motion* 46.7, pp. 435–450. ISSN: 01652125. DOI: `10.1016/j.wavemoti.2009.04.002`.

Sun, C. T. et al. (1968). “Time-harmonic waves in a stratified medium propagating in the direction of the layering”. In: *Journal of Applied Mechanics* 35.2, pp. 408–411.

Sundaram, M. Meenakshi and G. K. Ananthasuresh (2009). “Gustave Eiffel and his optimal structures”. In: *Resonance* 14.9, pp. 849–865. ISSN: 09718044. DOI: `10.1007/s12045-009-0081-x`.

Talbot, J. P. and H. E. M. Hunt (2003). "A computationally efficient piled-foundation model for studying the effects of ground-borne vibration on buildings". In: *Proceedings of the Institution of Mechanical Engineers, Part C: Journal of Mechanical Engineering Science* 217.9, pp. 975–989.

Tee, Kong Fah et al. (2010). "Wave propagation in auxetic tetrachiral honeycombs". In: *Journal of Vibration and Acoustics* 132.3, p. 031007. ISSN: 07393717. DOI: `10.1115/1.4000785`. URL: `http://vibrationacoustics.asmedigitalcollection.asme.org/article.aspx?articleid=1471471`.

Torquato, S. et al. (1998). "Effective Mechanical and Transport Properties of Cellular Solids". In: *International Journal of Mechanical Science* 40, pp. 71–82. ISSN: 1359-0286. DOI: `10.1016/j.cossms.2010.07.001`. URL: `http://dx.doi.org/10.1016/j.cossms.2010.07.001`.

Tripp, Marie K. et al. (2006). "The mechanical properties of atomic layer deposited alumina for use in micro- and nano-electromechanical systems". In: *Sensors and Actuators, A: Physical* 130-131, pp. 419–429. ISSN: 09244247. DOI: `10.1016/j.sna.2006.01.029`.

Valdevit, Lorenzo (2014). "Accurate Stiffness Measurement of Ultralight Hollow Metallic Microlattices by Laser Vibrometry". In: 694, pp. 1491–1495. DOI: `10.1007/s11340-014-9917-8`.

Valdevit, Lorenzo et al. (2011). "Protocols for the optimal design of multi-functional cellular structures: From hypersonics to micro-architected materials". In: *Journal of the American Ceramic Society* 94, pp. 15–34. ISSN: 00027820. DOI: `10.1111/j.1551-2916.2011.04599.x`.

Vasseur, J. O. et al. (1994). "Complete acoustic band gaps in periodic fibre reinforced composite materials: the carbon/epoxy composite and some metallic systems". In: *Journal of Physics: Condensed Matter* 6.42, p. 8759. ISSN: 0953-8984. DOI: `10.1088/0953-8984/6/42/008`.

Wadley, Haydn N. G. (2006). "Multifunctional periodic cellular metals". In: *Philosophical Transactions of the Royal Society A: Mathematical, Physical and Engineering Sciences* 364.1838, pp. 31–68. ISSN: 1364-503X, 1471-2962. DOI: `10.1098/rsta.2005.1697`. URL: `http://rsta.royalsocietypublishing.org/content/364/1838/31`.

Wadley, Haydn N. G. et al. (2003). "Fabrication and structural performance of periodic cellular metal sandwich structures". In: *Composites Science and Technology* 63, pp. 2331–2343. ISSN: 02663538. DOI: `10.1016/S0266-3538(03)00266-5`.

Wang, Pai et al. (2015). "Locally resonant band gaps in periodic beam lattices by tuning connectivity". In: *Physical Review B - Condensed Matter and Materials Physics* 91.2, pp. 2–5. ISSN: 1550235X. DOI: `10.1103/PhysRevB.91.020103`.

Wen, Jihong et al. (2008). “Directional propagation characteristics of flexural wave in two-dimensional periodic grid-like structures”. In: *Journal of Physics D: Applied Physics* 41.13, p. 135505. ISSN: 0022-3727. DOI: `10.1088/0022-3727/41/13/135505`. URL: `http://stacks.iop.org/0022-3727/41/i=13/a=135505`.

Wilson, Edward L. (1974). “The static condensation algorithm”. In: *International Journal for Numerical Methods in Engineering* 8, pp. 198–203.

Yu, Dianlong, Yaozong Liu, Gang Wang, Li Cai, et al. (2006). “Low frequency torsional vibration gaps in the shaft with locally resonant structures”. In: *Physics Letters, Section A: General, Atomic and Solid State Physics* 348.3-6, pp. 410–415. ISSN: 03759601. DOI: `10.1016/j.physleta.2005.08.067`.

Yu, Dianlong, Yaozong Liu, Gang Wang, Honggang Zhao, et al. (2006). “Flexural vibration band gaps in Timoshenko beams with locally resonant structures with two degrees of freedom”. In: *Journal of Applied Physics* 100.12, pp. 1–5. ISSN: 00218979. DOI: `10.1063/1.2400803`.

Zelhofer, Alex J. and Dennis M. Kochmann (2017). “On acoustic wave beaming in two-dimensional structural lattices”. In: *International Journal of Solids and Structures* 115, pp. 248–269.

Zheng, Xiaoyu et al. (2014). “Ultralight, ultrastiff mechanical metamaterials.” In: *Science (New York, N.Y.)* 344.6190, pp. 1373–7. ISSN: 1095-9203. DOI: `10.1126/science.1252291`. URL: `http://www.ncbi.nlm.nih.gov/pubmed/24948733`.

Zimmerman, D. (2003). “Special Issue on Dynamics of Phononic Materials and Structures”. In: *Journal of Vibration and Acoustics* 137.February, p. 29634. DOI: `10.1177/107754603030575`.

Appendix A

HIERARCHICAL LATTICE CONFIGURATIONS

Tbl. A.1 shows all the second-order numerically realized unit cells.

Table A.1: Second-order, half cell unit cells experimentally and computationally realized

Composition	Geometry	1st order unit cell size (μm)	Num. 1st-order unit cells , *N*	Voxel major axis (μm)	Voxel minor axis (μm)	Wall thickness (nm)	Relative density
Solid Polymer	Octahedron-of-Octahedra	8	10	0.7525	0.317	n/a	0.0103113
		8	15	0.7525	0.317	n/a	0.00449315
		8	20	0.7525	0.317	n/a	0.00249912
		12	10	0.7525	0.317	n/a	0.00479697
		12	15	0.7525	0.317	n/a	0.00208892
		12	20	0.7525	0.317	n/a	0.00116154
	Octahedron-of-Octets	8	10	0.7525	0.317	n/a	0.0210253
		8	15	0.7525	0.317	n/a	0.00946245
		8	20	0.7525	0.317	n/a	0.00533641
		12	10	0.7525	0.317	n/a	0.00981578
		12	15	0.7525	0.317	n/a	0.00441424
		12	20	0.7525	0.317	n/a	0.00248865
Composite	Octahedron-of-Octahedra	8	10	0.7725	0.337	20	0.0112059
		8	15	0.7725	0.337	20	0.00488344
		8	20	0.7725	0.337	20	0.00271631
		12	10	0.7725	0.337	20	0.00522722
		12	15	0.7725	0.337	20	0.00227641
		12	20	0.7725	0.337	20	0.00126582
	Octahedron-of-Octets	8	10	0.7725	0.337	20	0.022841
		8	15	0.7725	0.337	20	0.0102987
		8	20	0.7725	0.337	20	0.00582584
		12	10	0.7725	0.337	20	0.0106938
		12	15	0.7725	0.337	20	0.00480942
		12	20	0.7725	0.337	20	0.00272999
Hollow Al2O3	Octahedron-of-Octahedra	8	10	0.7725	0.337	20	0.0008946
		8	15	0.7725	0.337	20	0.00039029
		8	20	0.7725	0.337	20	0.00021719
		12	10	0.7725	0.337	20	0.00043025
		12	15	0.7725	0.337	20	0.00018749
		12	20	0.7725	0.337	20	0.00010428
	Octahedron-of-Octets	8	10	0.7725	0.337	20	0.0018157
		8	15	0.7725	0.337	20	0.00083625
		8	20	0.7725	0.337	20	0.00048943
		12	10	0.7725	0.337	20	0.00087802
		12	15	0.7725	0.337	20	0.00039518
		12	20	0.7725	0.337	20	0.00024134